



Provided by the author(s) and University of Galway in accordance with publisher policies. Please cite the published version when available.

Title	Experimental and computational investigation of atherosclerotic plaque biomechanics
Author(s)	O'Reilly, Brían L.
Publication Date	2019-11-22
Publisher	NUI Galway
Item record	<a href="http://hdl.handle.net/10379/15952">http://hdl.handle.net/10379/15952</a>

Downloaded 2024-05-10T20:23:13Z

Some rights reserved. For more information, please see the item record link above.



# **Experimental and Computational Investigation of Atherosclerotic Plaque Biomechanics**

**Brían L. O'Reilly B.E.**



A thesis submitted to the National University of Ireland as fulfilment of the requirements for the Degree of Doctor of Philosophy

**2019**

Biomedical Engineering  
College of Science and Engineering  
National University of Ireland Galway

Supervisor of Research: Dr. Patrick McGarry

Co-Supervisor: Prof. Peter McHugh

## ABSTRACT

The overall objective of this thesis is to provide new insights into the composition and biomechanical behaviour of atherosclerotic plaque. Experimental and computational analysis techniques are developed to investigate the morphological distributions and mechanical behaviour of calcified particles and fibrous tissue in excised carotid and femoral plaque samples. Finite element simulations are performed to analyse the influence of plaque and calcification morphology and lumen gain following stent deployment. Additionally, cohesive zone models are implemented to predict the modes of plaque rupture during standard balloon angioplasty and cutting balloon angioplasty.

Experimental testing reported in Chapter 4 presents a novel investigation of the morphological and mechanical properties of human iliofemoral and carotid atherosclerotic plaque constituents. Micro-computed tomography analysis is used to characterize the content and morphology of calcifications in excised plaques. The largest calcified particle contributes most of the total calcification in the plaque. Unconfined compression testing of isolated calcifications uncover viscoelastic behaviour and tensile stress relaxation uncovered viscoelastic behaviour in fibrous atherosclerotic samples. Ilio-femoral fibrous samples are found to be significantly stiffer than carotid fibrous samples. Results show isolated calcifications are significantly stiffer than non-calcified fibrous tissue.

Utilising this experimental characterisation data, the effects of calcification volumes on balloon angioplasty and stenting are explored in Chapter 5. The effects of calcification on stenting and balloon angioplasty biomechanics are investigated to potentially assist optimisation of atherosclerosis treatment. Implementing finite element methods, balloon expansion is simulated in stenosed arteries with various calcification content and geometries. It is shown that the balloon pressure to achieve full patency increases with

increasing calcification volume. The presence of circumferentially aligned calcifications results in a higher balloon pressure in comparison to longitudinally aligned calcifications. High strains are calculated in fibrous tissue where it is in series with calcification in the circumferential direction and in the thinnest section of fibrous tissue. Eccentric plaque models with varying calcification content are stented using two stents of different strut thicknesses. The highest maximum principal strains are predicted at the connecting struts at the distal and proximal ends of the stenosis.

Large strains computed during the balloon deployments motivated the investigation of the mechanisms of plaque rupture in Chapter 6. Cohesive zone formulations are used to model fibrous plaque tissue fracture and delamination at the fibrous tissue-calcification interface and at the fibrous plaque tissue-artery interface. Simulations reveal that the mechanism of rupture is intra-fibrous tissue crack propagation in the radial direction through the thinnest section of the plaque. The consequent release of strain energy from the plaque following such rupture eliminates the occurrence of delamination of calcified particles from the fibrous tissue or delamination of the plaque from the artery wall. Simulations also reveal that cutting-balloon angioplasty reduces the pressure required for rupture if one of the blades is positioned at the thinnest section of the plaque. Otherwise, the introduction of cuts into the fibrous tissues is predicted to increase the pressure required to cause rupture.

## ACKNOWLEDGMENTS

Firstly, I would like to thank my supervisors, Dr Patrick McGarry and Prof Peter McHugh for all their guidance and supervision. Their immense assistance, enthusiasm and knowledge helped me to overcome the many challenges faced throughout the PhD.

To the Western Vascular Institute, I am very grateful for all the assistance with the collection of samples and providing clinical perspectives on my work. I would like to thank all the technical staff for all the help with experimental testing, especially David Connolly for the training and innovative ideas for testing and scanning.

I would like to thank my funding sources the College of Engineering and Informatics Scholarship. I would also like to acknowledge the Irish Centre for High-End Computing (ICHEC) for the computational capabilities provided.

To the McGarry (including Ciara) and McHugh research groups past and present, I would first like to apologize for being a constant distraction, secondly, I would like to thank you all for the craic and many chats. To all the postgrads throughout the years (even the 2<sup>nd</sup> floor), you all made the PhD a much better experience through tag rugby, lunch time quizzes, baked goods and Friday night pints.

To my friends from Galway I made through all my years here, you have all ensured that Galway will always be my home away from home. To all my friends from Mullingar, thanks for always being there and making sure I could never have a weekend free. Thank you to all my friends for being the best group of friends I could ever ask for. In particular, I would like to thank Eóin for years of friendship and helping me too many times to count.

To my parents, Hugh and Maura, I thank you for your constant stream of support and encouragement. I could not have done my postgraduate without you. To my brother Ciarán, it's been great to always have someone to chat to even if it was always the same two topics.

To Eimear, you have been a great source of motivation and inspiration all the way through. I cannot thank you enough for your patience in not killing me especially when I was getting close to the end of the PhD.

# TABLE OF CONTENTS

<b>1 INTRODUCTION.....</b>	<b>1</b>
1.1 GENERAL INTRODUCTION .....	1
1.2 AIMS AND OBJECTIVES OF THE THESIS .....	3
1.3 THESIS STRUCTURE .....	4
1.4 REFERENCES.....	6
<b>2 BACKGROUND AND LITERATURE REVIEW.....</b>	<b>8</b>
2.1 INTRODUCTION.....	8
2.2 ATHEROSCLEROTIC PLAQUE.....	9
2.2.1 <i>Structure of Atherosclerotic Plaque</i> .....	9
2.2.2 <i>Mechanical Characterisation and Testing</i> .....	10
2.3 COMPUTATIONAL MODELLING OF ATHEROSCLEROTIC PLAQUE.....	17
2.3.1 <i>Inelasticity and damage modelling approaches</i> .....	22
2.4 PLAQUE RUPTURE STRESS.....	24
2.5 APPLICATIONS IN STENT ANGIOPLASTY .....	26
2.5.1 <i>Stent design assessment</i> .....	27
2.6 DISCUSSION.....	35
2.7 REFERENCES.....	38
<b>3 THEORY .....</b>	<b>46</b>
3.1 INTRODUCTION.....	46
3.1 CONTINUUM MECHANICS.....	46
3.1.1 <i>Deformation and motion</i> .....	47
3.1.2 <i>Strain measures</i> .....	48
3.1.3 <i>Stress measures</i> .....	51
3.2 CONSTITUTIVE LAWS.....	52

3.3 FINITE ELEMENT METHOD.....	57
3.3.1 <i>Implicit finite element method</i> .....	57
3.3.2 <i>Explicit finite element method</i> .....	61
3.4 FRACTURE MODELLING.....	62
3.4.1 <i>Cohesive Zone Modelling (CZM)</i> .....	62
3.5 REFERENCES.....	64
<b>4 MATERIAL CHARACTERISATION AND IMAGING OF DISCRETE ILIOFEMORAL AND CAROTID ATHEROSCLEROTIC PLAQUE CONSTITUENTS .....</b>	<b>65</b>
4.1 INTRODUCTION.....	65
4.2 METHODOLOGY.....	67
4.2.1 <i>Sample acquisition</i> .....	67
4.2.2 <i>Micro computed tomography analysis</i> .....	68
4.2.3 <i>Fibrous tissue uniaxial mechanical testing</i> .....	72
4.2.4 <i>Isolated calcified particle compression testing and inverse finite element analysis</i> .....	75
4.2.5 <i>Scanning electron microscopy</i> .....	76
4.3 RESULTS.....	77
4.3.1 <i>Micro computed tomography analysis</i> .....	77
4.3.2 <i>Fibrous uniaxial testing results</i> .....	79
4.3.3 <i>Calcification compression testing and inverse finite element analysis</i> .....	81
4.3.4 <i>Scanning electron microscopy</i> .....	85
4.4 DISCUSSION.....	86
4.5 REFERENCES.....	91
APPENDIX 4A.....	95
APPENDIX 4B .....	98

<b>5 STENT AND BALLOON ANGIOPLASTY IN CALCIFIED ATHEROSCLEROTIC STENOSES .....</b>	<b>99</b>
5.1 INTRODUCTION.....	99
5.2 METHODOLOGY.....	101
5.2.1 <i>Atherosclerotic plaque geometry construction</i> .....	101
5.2.2 <i>Balloon angioplasty finite element model construction</i> .....	106
5.2.3 <i>Stent angioplasty simulations</i> .....	107
5.3 RESULTS.....	111
5.3.1 <i>Balloon angioplasty simulations</i> .....	111
5.3.2 <i>Stent radial force test</i> .....	115
5.3.3 <i>Stenting simulations</i> .....	117
5.4 DISCUSSION.....	120
5.5 REFERENCES.....	125
APPENDIX 5A.....	129
<b>6 COHESIVE ZONE SIMULATION OF PLAQUE FAILURE DURING BALLOON ANGIOPLASTY .....</b>	<b>135</b>
6.1 INTRODUCTION.....	135
6.2 METHODOLOGY.....	137
6.2.1 <i>Rupture experiment and inverse finite element modelling</i> .....	137
6.2.2 <i>2D angioplasty damage models</i> .....	140
6.2.3 <i>Cutting balloon simulations</i> .....	145
6.3 RESULTS.....	146
6.3.1 <i>Rupture experiments and inverse finite element modelling</i> .....	146
6.3.2 <i>2D angioplasty damage models</i> .....	148
6.3.3 <i>Cutting Balloons</i> .....	152
6.4 DISCUSSION.....	154



6.5 REFERENCES.....	159
<b>7 CONCLUDING REMARKS AND FUTURE RECOMMENDATIONS.....</b>	<b>162</b>
7.1 SUMMARY OF KEY FINDINGS .....	162
7.1.1 Chapter 4.....	162
7.1.2 Chapter 5.....	163
7.1.3 Chapter 6.....	163
7.2 FUTURE RECOMMENDATIONS.....	163
7.3 REFERENCES.....	167

# 1 INTRODUCTION

## 1.1 General introduction

Atherosclerosis is an insidious progressive disease that thickens arterial walls leading to a vascular stenosis, known as atherosclerotic plaque. These plaques are typically complex structures consisting of fibrous matrix, lipids and calcifications. Structural changes occur as the plaque develops and may become unstable over time, leading to rupture. Plaque rupture is a catastrophic clinical event leading to myocardial infarction, stroke or death (Herrington et al., 2016). Atherosclerosis, depending on the affected arteries, can be typically categorized as coronary artery disease (CAD), peripheral artery disease (PAD), carotid artery disease or cerebrovascular disease. CAD is the most common cause of death in the United States, resulting in 8.9 million deaths in 2015 (GBD, 2016). The most common surgical treatments for atherosclerotic arteries are balloon angioplasty, stent angioplasty (balloon angioplasty with stenting), bypass and endarterectomy (Muir, 2009). The effectiveness of vascular device treatment can be enhanced by improving medical device design. Although balloon angioplasty and stenting have relatively low mortality rates (approximately 2 %) (Rastan et al., 2013; Rodriguez et al., 2003), with an aging population, improvements in stent design have the potential to become increasingly important in upcoming decades.

The use of the finite element method is now well established in medical device research and industrial application, for analysis, design and performance assessment. Additionally, it forms part of the medical device regulatory approval process, and, specifically, is currently recommended by the Food and Drug Administration (FDA, 2010) to assess the performance of vascular devices in conjunction with benchtop testing, for regulatory approval. In order to generate accurate finite element models for such purposes (analysis, design and performance assessment), accurate material behaviour and geometrical properties are required. In relation to stent angioplasty in particular, although it is not currently a requirement to use arterial or atherosclerotic models in computational analysis for regulatory approval, Conway et al. (2014) recommended using more representative constitutive laws to describe the mechanical behaviour of plaque constituents and discrete inclusion of plaque constituents in stenting models.

In the current literature, experimental testing of plaque has mostly focussed on heterogeneous plaque samples (Barrett et al., 2017; Cunnane et al., 2015; Loree et al., 1994; Maher et al., 2011; Mulvihill et al., 2013). It has also been shown that small changes in the mechanical behaviour and geometrical properties of the plaque components can result in large changes in the mechanical stresses in the plaque during loading (Buffinton and Ebenstein, 2014; Conway et al., 2014b; Fan et al., 2016; Holzapfel et al., 2005; Wong et al., 2012). In order to accurately simulate localised stresses in plaques during balloon angioplasty and stenting, it is necessary to include realistic geometrical representations of plaque constituents and accurate constitutive laws to describe their respective material behaviours.

In order to address this need, the work of the thesis is focused on experimental testing of homogenous plaque constituents and imaging of plaque morphologies to provide new understanding of the mechanical contribution of the individual constituents. Utilising the new understanding and data on plaque, a range of vascular device treatments is

biomechanically assessed. Novel rupture models are generated to assess the effect of calcification inclusions and the use of cutting balloons during angioplasty. The findings presented in this thesis have important implications for future modelling of atherosclerotic plaque. The novel approaches presented provide new insights into the biomechanics of vascular implant deployment in atherosclerotic arteries.

## 1.2 Aims and objectives of the thesis

The overall objective of this thesis is to provide new insights into the composition and biomechanics of atherosclerotic plaque. Specifically, the work is focused on investigating the mechanics of calcified and fibrous tissue in plaque, and assessing the mechanical contribution of the different tissue types during balloon angioplasty and stenting, thus providing a framework for enhanced vascular device computational models. The findings of this study will inform the design and development of the next generation of endovascular devices. The specific aims of this research are to:

- Establish material behaviour of individual atherosclerotic plaque constituents to enable calibration of accurate constitutive laws for future plaque representations in computational modelling.
- Investigate the composition and geometric structure of atherosclerotic plaques and their constituents to facilitate the creation of more realistic atherosclerotic geometries for finite element implementation.
- Investigate the site specificity of plaque through imaging techniques and the mechanical testing of plaque samples obtained from different arteries of origin (carotid and femoral), exploring the requirement for modelling using location relevant material behaviour.
- Ascertain geometric configurations and compositions that influence the biomechanical stress state during vascular device deployment. This can be

investigated using the finite element motivated by imaging and mechanical testing data.

- Explore rupture during balloon angioplasty and cutting balloon angioplasty in calcified and fibrous plaques, investigating the critical failure paths during rupture.

### 1.3 Thesis structure

The outline of this thesis is as follows:

- Chapter 2 presents the background to the current literature on the topic of atherosclerotic plaque (section 2.2) and stenting (section 2.3) in the field of biomedical engineering. This chapter describes various approaches for experimental testing and computational modelling of atherosclerotic plaques, and the modelling of stenting in stenosed arteries. The specific background of each topic, in relation to this thesis, is also presented in the introduction to each technical chapter (Chapters 4 – 6).
- Chapter 3 discusses the background to the numerical and computational modelling methods utilised in this thesis. Section 3.2 introduces fundamentals of continuum mechanics, section 3.3 defines the constitutive laws used in the technical chapters, section 3.4 describes the finite element method and section 3.5 presents cohesive models for rupture.
- Chapter 4 explores mechanical testing of carotid and iliofemoral atherosclerotic fibrous tissue and calcifications. Micro-computed tomography ( $\mu$ CT) imaging is used to investigate calcification content and morphologies. Inverse finite element methods are used to calibrate material constitutive laws based on experimentally observed mechanical behaviour. The constitutive models calibrated for the constituents are then implemented in Chapters 5 and 6.

- Chapter 5 utilises  $\mu$ CT data to create plaques with realistic calcification geometries. The influence of eccentricity, calcification volume, calcification aspect ratio, and stent radial force in device deployment are explored.
- Chapter 6 describes a finite element investigation of cohesive interfaces to model plaque rupture. Cohesive strength for the calcification-fibrous boundary is calibrated from experimental testing results. Balloon angioplasty and cutting balloon deployment is simulated with cohesive zones in varying interface configurations in both fibrous calcified plaques.
- Chapter 7 summarises the key contributions of this work, followed by and recommendations for future research in terms of atherosclerotic plaque, mechanical testing and medical device development.

## 1.4 References

- Barrett, H.E., Cunnane, E.M., Hidayat, H., O'Brien, J.M., Kavanagh, E.G., Walsh, M.T., 2017. Calcification Volume Reduces Stretch Capability and Predisposes Plaque to Rupture in an in vitro Model of Carotid Artery Stenting. *Eur. J. Vasc. Endovasc. Surg.* 54, 431–438. <https://doi.org/10.1016/j.ejvs.2017.07.022>
- Buffinton, C.M., Ebenstein, D.M., 2014. Effect of Calcification Modulus and Geometry on Stress in Models of Calcified Atherosclerotic Plaque. *Cardiovasc. Eng. Technol.* 5, 244–260. <https://doi.org/10.1007/s13239-014-0186-6>
- Conway, C., McGarry, J.P., McHugh, P.E., 2014a. Modelling of Atherosclerotic Plaque for use in a Computational Test-Bed for Stent Angioplasty. *Ann. Biomed. Eng.* 42, 2425–2439.
- Conway, C., McGarry, J.P., McHugh, P.E., 2014b. Modelling of Atherosclerotic Plaque for Use in a Computational Test-Bed for Stent Angioplasty. *Ann. Biomed. Eng.* 42, 2425–2439. <https://doi.org/10.1007/s10439-014-1107-4>
- Cunnane, E.M., Mulvihill, J.J.E., Barrett, H.E., Healy, D.A., Kavanagh, E.G., Walsh, S.R., Walsh, M.T., 2015. Mechanical, biological and structural characterization of human atherosclerotic femoral plaque tissue. *Acta Biomater.* 11, 295–303. <https://doi.org/10.1016/j.actbio.2014.09.024>
- Fan, Z.M., Liu, X., Du, C.F., Sun, A.Q., Zhang, N., Fan, Z.M., Fan, Y.B., Deng, X.Y., 2016. Plaque components affect wall stress in stented human carotid artery: A numerical study. *Acta Mech. Sin. Xuebao* 32, 1149–1154. <https://doi.org/10.1007/s10409-016-0572-4>
- FDA, 2010. No Title [WWW Document]. Non-Clinical Eng. Tests Recomm. Labeling Intravasc. Stents Assoc. Deliv. Syst. - Guid. Ind. FDA Staff. URL <https://www.fda.gov/regulatory-information/search-fda-guidance-documents/non-clinical-engineering-tests-and-recommended-labeling-intravascular-stents-and-associated-delivery> (accessed 10.15.19).
- GBD, 2016. Global, regional, and national life expectancy, all-cause mortality, and cause-specific mortality for 249 causes of death, 1980–2015: a systematic analysis for the Global Burden of Disease Study 2015. *Lancet* 388, 1459–1544. [https://doi.org/10.1016/S0140-6736\(16\)31012-1](https://doi.org/10.1016/S0140-6736(16)31012-1)
- Herrington, W., Lacey, B., Sherliker, P., Armitage, J., Lewington, S., 2016. Epidemiology of Atherosclerosis and the Potential to Reduce the Global Burden of Atherothrombotic Disease. *Circ. Res.* 118, 535–546. <https://doi.org/10.1161/CIRCRESAHA.115.307611>
- Holzapfel, G.A., Stadler, M., Gasser, T.C., 2005. Changes in the Mechanical Environment of Stenotic Arteries During Interaction With Stents: Computational Assessment of Parametric Stent Designs. *J. Biomech. Eng.* 127, 166–180. <https://doi.org/10.1115/1.1835362>

Loree, H.M., Grodzinsky, A.J., Park, S.Y., Gibson, L.J., Lee, R.T., 1994. Static circumferential tangential modulus of human atherosclerotic tissue. *J. Biomech.* 27, 195–204. [https://doi.org/10.1016/0021-9290\(94\)90209-7](https://doi.org/10.1016/0021-9290(94)90209-7)

Maher, E., Creane, A., Sultan, S., Hynes, N., Lally, C., Kelly, D.J., 2011. Inelasticity of Human Carotid Atherosclerotic Plaque. *Ann. Biomed. Eng.* 39, 2445–2455. <https://doi.org/10.1007/s10439-011-0331-4>

Muir, R.L., 2009. Peripheral arterial disease: Pathophysiology, risk factors, diagnosis, treatment, and prevention. *J. Vasc. Nurs.* 27, 26–30. <https://doi.org/10.1016/j.jvn.2009.03.001>

Mulvihill, J.J., Cunnane, E.M., McHugh, S.M., Kavanagh, E.G., Walsh, S.R., Walsh, M.T., 2013. Mechanical, biological and structural characterization of in vitro ruptured human carotid plaque tissue. *Acta Biomater.* 9, 9027–9035. <https://doi.org/10.1016/j.actbio.2013.07.012>

Rastan, A., Krankenberg, H., Baumgartner, I., Blessing, E., Müller-Hülsbeck, S., Pilger, E., Scheinert, D., Lammer, J., Giler, M., Noory, E., Neumann, F.J., Zeller, T., 2013. Stent placement versus balloon angioplasty for the treatment of obstructive lesions of the popliteal artery: A prospective, multicenter, randomized trial. *Circulation* 127, 2535–2541. <https://doi.org/10.1161/CIRCULATIONAHA.113.001849>

Rodriguez, A., O'Neill, W., Palacios, I.F., Alemparte, M.R., Baldi, J., Navia, J., Delacasa, A., Vogel, D., Oliveri, R., Pereira, C.F., Bernardi, V., 2003. Coronary stenting versus coronary bypass surgery in patients with multiple vessel disease and significant proximal LAD stenosis: Results from the ERACI II study. *Heart* 89, 184–188. <https://doi.org/10.1136/heart.89.2.184>

Wong, K.K.L., Thavornpattanapong, P., Cheung, S.C.P., Sun, Z., Tu, J., 2012. Effect of calcification on the mechanical stability of plaque based on a three-dimensional carotid bifurcation model. *{BMC} Cardiovasc. Disord.* 12. <https://doi.org/10.1186/1471-2261-12-7>



# 2 BACKGROUND AND LITERATURE REVIEW

## 2.1 Introduction

Atherosclerosis is an insidious cardiovascular and peripheral vascular disease that thickens arterial walls leading to a vascular stenosis, known as atherosclerotic plaque. Risk factors that increase the likelihood of atherosclerosis include advanced age, smoking history, diabetes and high blood pressure (Razzouk et al., 2015). Approximately 1.5 million Americans have an acute myocardial infarction annually, with one-third resulting in death (Chhabra et al., 2019). Also each year cardiovascular disease causes 3.9 million deaths in Europe (European Heart Network, 2017) and in 2016, more than 9,000 deaths in Ireland (Irish Heart Foundation, 2018). One of the most common treatments of atherosclerosis is stenting. In the US 1.8 million stents are implanted every year, most of which are coronary stents (iDataResearch, 2018). Peripheral stenting is also a major concern worldwide; it is currently estimated approximately 10% of the world's population have peripheral arterial disease (Peach et al., 2012). With such a large proportion of the world's population at risk of needing vascular intervention, it is of paramount importance the maximisation of treatment effectiveness is achieved.

The experimental characterisation and modelling of atherosclerotic plaque tissue is distinctly lacking and still represents a frontier for vascular mechanics and modelling (Akyildiz et al., 2014). The importance of accuracy in the modelling of atherosclerotic plaque is paramount in the correct prediction of performance of vascular implants, such as stents. Further to this, improvements in modelling capabilities for the prediction of implant performance could be very beneficial in the evolution of regulatory approval processes, for example the requirements for the finite element modelling of stents as part of the medical device regulatory approval process for the Food and Drug Administration (FDA) and CE mark approval. A more accurate insight in the stress-strain analysis of stents and the tissue could better predict the performance of stenting in-vivo, potentially leading to better outcomes.

## 2.2 Atherosclerotic Plaque

### 2.2.1 Structure of Atherosclerotic Plaque

Atherosclerotic plaque is an extremely complex structure with vast variations in both geometry and constituents. Human atherosclerotic plaques contain calcifications, fibrous material, macrophages, and lipid content and the quantities and geometry of which change throughout each individual plaque and vary between whole plaque samples. The pathology of atherosclerosis contains a wide range of configurations and structures that can change over time as soft lesions evolve to become hard calcified lesions. An illustration of a atherosclerotic plaque, HC Stary (1999) is presented in Figure 2.1. In this illustration components such as lipid pools, calcifications and a fibrous cap are shown. During atherogenesis smooth muscle cells migrate from the arterial media into the intima and then proliferate and inducing collagen formation. In more advanced stages stable lesions can continue to grow and can become highly calcified. Alternatively, the fibrous caps can become unstable, leading to rupture and the formation of thrombus material,

which can lead to embolism formation in the blood flow. A particularly dangerous occurrence is the development of a “vulnerable” plaque, where the lesion can become unstable and the fibrous cap ruptures. (Chai et al., 2014b)

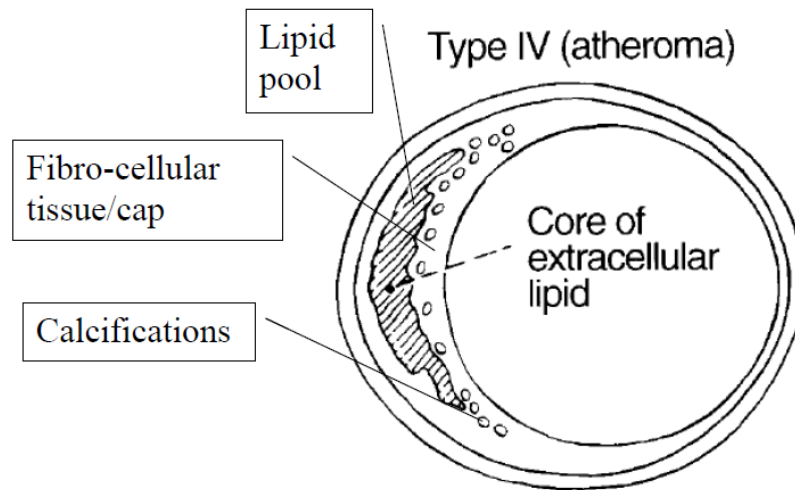


Figure 2.1. Illustration of the cross section of an atherosclerotic plaque. Plaques constituents usually include lipid pools, a fibrous cap and calcifications. Image adapted from Stary (1999).

### 2.2.2 Mechanical Characterisation and Testing

There are many challenges in the mechanical testing of atherosclerotic plaque tissue. There are also issues with obtaining tissue, particularly from humans due to sample availability. The tissue is highly heterogeneous, and a broad range of structural variability exists, leading to a discussion of whether testing entire plaques or cut sections of a plaque is more appropriate (Holzapfel et al., 2004). One major limitation to plaque tissue analysis, characterisation and testing is the lack of a robust animal model of atherosclerotic plaque that is sufficiently representative of the disease in humans (Karimi et al., 2014b). The lack of such a model has significant implications for material availability, consistency and test reproducibility.

In the current literature, the main approach to experimental testing is macroscopic mechanical testing, focusing on compressive and tensile loading to examine the mechanical response (stress-strain curves) and mechanical properties of plaque, including elastic modulus and ultimate tensile strength (UTS). An example of this type of testing is highlighted in

Figure 2.2, which shows an illustration of the mechanical testing and results analysis from Cunnane et al. (2016). Other examples of macroscale testing include: Barrett et al. (2016); Cunnane et al. (2015); Lawlor et al. (2011); Loree et al. (1994); Maher et al. (2009) and Mulvihill et al. (2013). There has been a limited focus on determining local or sub-structure tissue mechanical properties. Examples of studies focusing on macroscopic mechanical characterisation include: Barrett et al. (2016); Cunnane et al. (2015); Lawlor et al. (2011); Loree et al. (1994); Maher et al. (2011, 2009); Mulvihill et al. (2013); Salunke et al. (2001); Teng et al. (2009); Topoleski et al. (1997); and Walraevens et al. (2008). Also reported in a number of these studies are macroscopic constitutive model fits to the experimental stress-strain data, using Neo-Hookean and polynomial hyperelastic models, which are outlined in Chapter 3 of this thesis.

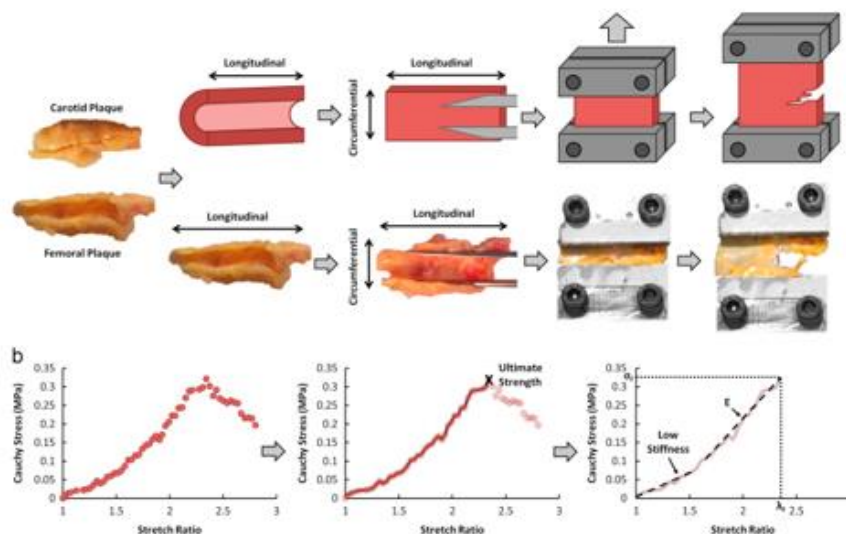


Figure 2.2. (a) Schematic of the mechanical testing protocol of carotid and femoral plaque samples in both the longitudinal and circumferential directions. (b) Analysis of the mechanical testing results (Cunnane et al., 2016).

The study of Loree et al. (1994) is an influential early study where the broad variation in mechanical response is clearly illustrated (see Figure 2.3) as a function of plaque material type. Useful data on basic stress-strain curve shape, and fracture stress and strain ranges, are reported; for example, fracture stresses in the range 149 to 701 kPa, and strains in the range 15 to 60%. This data has been used as the basis for a number of plaque constitutive model calibrations in subsequent studies, including: Conway et al. (2014, 2012); Gastaldi et al. (2010); Morlacchi and Migliavacca (2013). The study of Maher et al. (2009) also illustrates tissue type dependence and large differences between tensile and compressive loading response (see Figure 2.4).

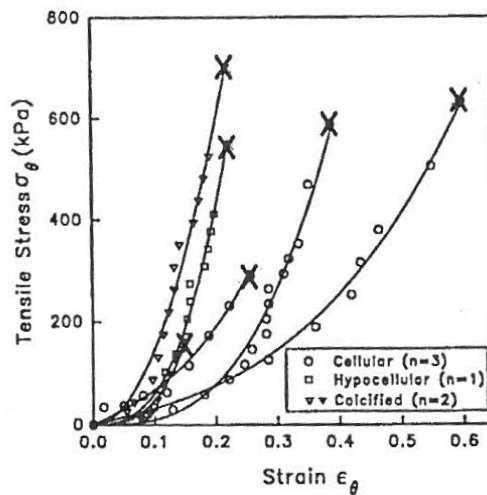


Figure 2.3. Tensile stress-strain curves for 6 fractured plaque specimens, categorised by plaque type, reported by Loree et al. (1994).

Due to the heterogeneity and broad range of structural variability a definitive and standardised tissue type categorisation has not been established. As such the tissue type descriptions reported in different studies are very much study dependent. This adds a layer

of complexity and uncertainty to the interpretation of mechanical data that is not present for traditional materials, where constituents, manufacturing route and mechanical properties generally adhere to well established standards. The Loree et al. (1994) and Maher et al. (2009) studies illustrate this point for plaque (Figure 2.3 and Figure 2.4); “cellular”, “hypocellular” and “echolucent” tissue types are identified, but these are quite subjectively defined as determined the specific microscopy/characterisation method employed. Another study by Barrett et al. (2016) has also proposed a number of calcified plaque sub-classifications.

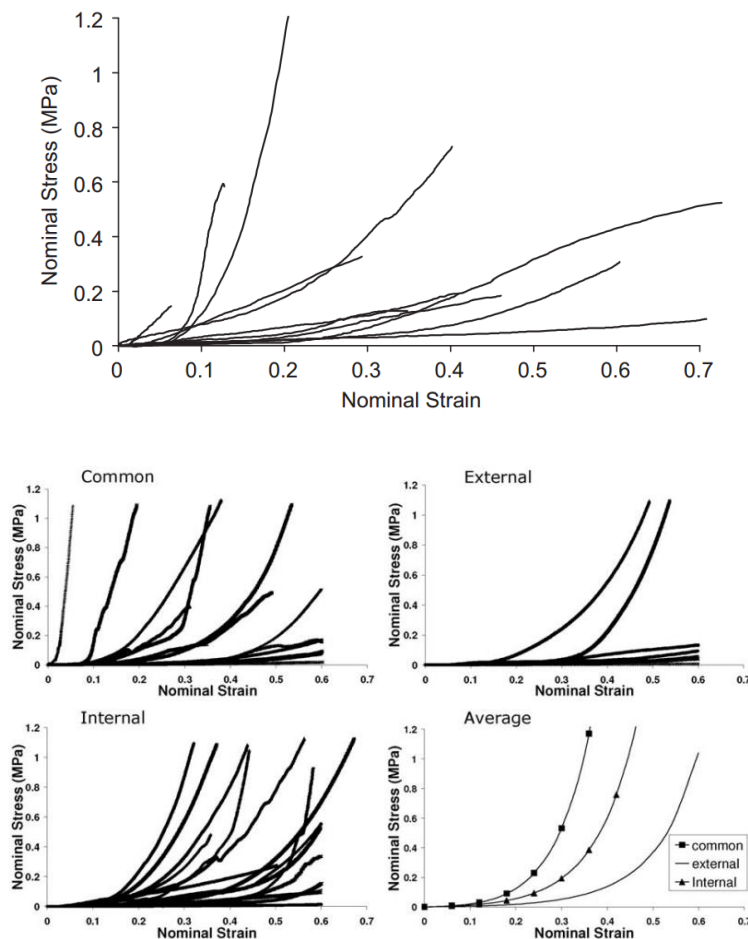


Figure 2.4. Figures from Maher et al. (2009) for mechanical testing of carotid plaque: (left) plot showing tensile stress-strain response, and (right) plot showing compressive stress-strain response (unconfined compression), depending on tissue type. The average

curves were obtained using a mean set of hyperelastic constants using a second order polynomial hyperelastic strain energy function.

Another issue in plaque testing is the site specificity of the samples. Usually plaque mechanical testing is carried out on carotid or peripheral atherosclerotic plaques. This creates issues with sample availability, as these vessels undergo endarterectomy more often when compared to atherosclerotic coronary arteries. Although the majority of stents implanted are coronary stents (iDataResearch, 2018), these blockages, if surgically treated, typically undergo a coronary artery bypass graft (CABG) procedure. Receiving samples from cadavers is often difficult and thus plaque samples from carotid and peripheral arteries are typically used as analogues for coronary plaques when examining mechanical behaviour.

The relatively small number of studies focusing on plaque tissue sub-structure characterisation includes those given in Table 2.1. A range of testing methods, including tensile and compressive mechanical testing, rheometry and nano-indentation, have been used to resolve the mechanical response and behaviour of individual plaque constituents such as the fibrous cap, lipid core, calcifications, etc. Anisotropy of constituent layers in plaque has also been measured through tensile testing in axial and circumferential arterial directions (Holzapfel et al., 2004; Teng et al., 2009).

Table 2.1. Experimental studies reporting on plaque tissue constituent mechanical characterisation.

Author	Location	Method	Data Reported / Model Fit	Constituents
<b>Cahalane et al. (2018)</b>	Carotid Peripheral	Indentation	Elastic Moduli	Calcification (17 - 25 GPa)
<b>Chai et al. (2014)</b>	Carotid	Indentation	Elastic Moduli	Fibrous Cap (9 - 203 kPa) Intima (11 - 475 kPa) Lipid Core (9 - 143 kPa)
<b>Barrett et al. (2009)</b>	Carotid	Indentation	Shear modulus	Fibrous Cap (7 - 100kPa)
<b>Ebenstein et al. (2009)</b>	Carotid	Indentation	Reduced Moduli	Calcification (0.2 - 1630 MPa) Fibrous Tissue (0.05 - 0.98 MPa) Hematoma (0.06 - 1.14 MPa)
<b>Holzapfel et al. (2004)</b>	Iliac	Tensile	Ultimate stress	Fibrous Cap (165.8 - 617.5 kPa) Fibrous Intima (171.8 - 999.2 kPa) Fibrotic Media (181.5 - 1278.1 kPa)
<b>Loree et al. (1994)</b>	Synthetic	Rheometer	Storage Moduli	Lipid Pools (47 - 313 Pa)
<b>Lee et al. (1991)</b>	Aorta	Cyclic Compressive	Elastic Moduli	Fibrous Cap (355 ± 245 kPa)



Nano- and micro-indentation presents very useful possibilities for determining constituents' mechanical behaviour, since the necessity to extract constituents can largely be avoided. Studies utilising nano-indentation (for example, Barrett et al. (2009) and Ebenstein et al. (2009)) have shown large variations in local constituent mechanical properties, similar to those seen at the macroscopic level for the tissue as a whole. While useful for determining material properties in the physiological loading regime, indentation is limited when response to higher (supra-physiological) loads are being explored, including tissue rupture behaviour.

A significant limitation in current atherosclerotic plaque computational modelling is the accurate modelling of plaque inelasticity and damage. Clearly, significant challenges exist in characterising plaque these experimentally, going beyond the difficulties associated with elastic and hyperelastic property identification. The small number of experimental studies that have investigated plaque inelasticity have shown the existence of inelastic/non-recoverable deformation (Ebenstein et al., 2009; Maher et al., 2011; Topoleski et al., 1997; Topoleski and Salunke, 2000) depends strongly on plaque type. Intimately linked with tissue inelasticity is tissue damage, not least because damage can manifest itself as inelastic deformation, with damage leading to material softening and rupture. It is very clear from clinical practice that plaque can experience damage and rupture as part of the angioplasty procedure. Consequently, there is a clear need for the accurate characterisation of these phenomena (inelasticity, damage, softening and rupture) for the development of more accurate atherosclerotic artery computational models, particularly for the simulation of vascular interventions, such as balloon angioplasty, stent implantation and atherectomy.

It should be emphasised that it is necessary to determine plaque tissue mechanical behaviour in both the physiological loading and supra-physiological loading regimes; the

latter is of significant importance due to the high local strains and stresses caused by vascular device deployment and implantation.

Overall, looking to the future, mechanical testing and characterisation of plaque tissue at the sub-structural scale is vitally important, to address the unmet need for more physically representative atherosclerotic plaque constitutive and damage models. Further experimentation is required to more comprehensively characterise non-recoverable/plastic deformation in plaque tissue, building on the limited work to date of Ebenstein et al. (2009), Maher et al. (2011), Topoleski et al. (1997) and Topoleski and Salunke (2000). It is essential that more representative constitutive models be developed for use in future computational investigations of vascular interventions such as stent angioplasty, where tissue load-unload-reload behaviour must be accurately predicted.

There are various comprehensive review articles on plaque testing and mechanical properties, an example of which is Cardoso and Weinbaum (2014) detailing the effects of microcalcifications on rupture, the main discussion points of which will be discussed in section 2.3. Another summary of the literature is in special issue on “Plaque Mechanics” in the Journal of Biomechanics by Gijssen and Migliavacca, (2014), that also makes reference to the work of, Akyildiz et al. (2014), Chai et al. (2014), Holzapfel et al. (2014), Kolandaivelu et al. (2014), and Walsh et al. (2014). This details experimental testing and computational modelling of atherosclerotic plaque and also detailing reviews of the literature in the field of plaque biomechanics.

### 2.3 Computational Modelling of Atherosclerotic Plaque

Based on the experimental mechanical property data that is available, constitutive models for plaque have been developed and implemented in computational models of

atherosclerotic arteries. Linear elastic plaque representations have been developed (typically found in earlier studies) based on measured elastic modulus data (Lee et al. (1992) & Cheng et al. (1993)). As an advancement on this, plaque tissue stress-strain curves have been used to calibrate a range of hyperelastic models in the finite deformation kinematic regime, this is the most common approach reported in the literature to date. The majority of studies have assumed material isotropy for individual plaque constituents or the plaque as a whole where homogeneity and effective properties are implemented (see Table 2.2). Anisotropy in fibrous tissue has also been explored. Table 2.2 gives a summary of reported computational studies involving atherosclerotic artery representations, where the studies have been categorised by spatial dimension (2D-planar or 3D), arterial geometry (idealised or realistic/patient specific, as might be determined from medical imaging), representation of the diseased tissue structure (whether homogenised or multi-component/multi-phase), and material model(s) employed. An illustrative example is that of Cilla et al. (2012) shown in Figure 2.5, where a lipid core is represented using a hyperelastic idealisation.

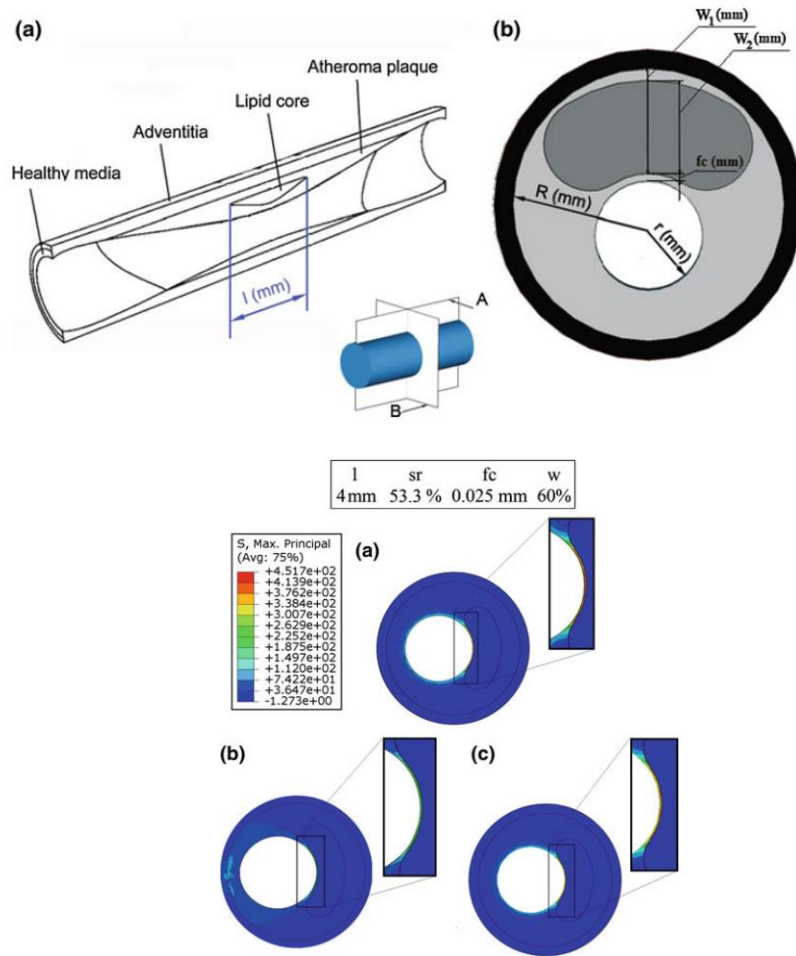


Figure 2.5. Idealised geometry of an atherosclerotic arterial model (transversal section) (top) and contour plots (bottom) of the maximum principal stress with residual stresses included in (a) the longitudinal direction , (b) the longitudinal and circumferential directions and (c) without either (Cilla et al., 2012).

Table 2.2 Computational modelling studies involving representation of atherosclerotic plaque.

Author	Type	Geometry	Constituents	Material Model
Lee et al. (1992)	2D	Idealised	Plaque Lipid Pool	Linear Elastic
Cheng et al. (1993)	2D	Realistic – Digitised tracing	Plaque Lipid Pool Calcification	Linear Elastic
Petrini et al. (2003)	3D	Idealised	Plaque	Hyperelastic 3 <sup>rd</sup> Order Polynomial
Chua et al. (2004)	3D	Idealised	Plaque	Linear Elastic
Migliavacca et al. (2004)	3D	Idealised	Plaque *3 types	Hyperelastic 3 <sup>rd</sup> Order Polynomial
Holzapfel et al. (2005)	3D	Realistic – MRI scan	Diseased Intima Lipid Pool Calcification	Anisotropic Hyperelastic
Li et al. (2006)	2D	Realistic – MRI scan	Fibrous Cap Lipid Pool	Hyperelastic Ogden n=2
Migliavacca et al. (2007)	3D	Idealised	Plaque	Hyperelastic 3 <sup>rd</sup> Order Polynomial
Kiouis et al. (2007)	3D	Realistic – MRI scan	Lipid Pool	Hyperelastic
Timmins et al. (2008)	3D	Idealised	Plaque (stiffness varied)	Hyperelastic 3 <sup>rd</sup> Order Polynomial
Bluestein et al. (2008)	3D	Idealised	Plaque Lipid Pool Calcification	Hyperelastic Mooney-Rivlin
Tang et al. (2009a)	2D	Realistic – MRI scan	Plaque Lipid Pool Calcification	Hyperelastic Modified Mooney-Rivlin
Tang et al. (2009b)	3D	Realistic – MRI scan	Plaque Lipid Pool Calcification	Hyperelastic Modified Mooney-Rivlin
Pericevic et al. (2009)	3D	Idealised	Plaque *3 Types	Hyperelastic Polynomial n=2
Gastaldi et al. (2010)	3D	Idealised	Plaque	Hyperelastic Polynomial n=2
Gu et al. (2010)	3D	Idealised	Plaque	Hyperelastic Polynomial n=2
Sadat et al. (2010)	2D	Realistic – MRI scan	Plaque Lipid Pool Calcification	Hyperelastic Ogden n=2
Zahedmanesh et al. (2010)	3D	Idealised	Plaque	Hyperelastic Ogden n=1

Chapter 2. Background and Literature Review

<b>Wenk et al. (2010)</b>	3D	Idealised	Fibrous Tissue Lipid Pool	Hyperelastic Fung
<b>Pant et al. (2011)</b>	3D	Idealised	Plaque	Hyperelastic Neo-Hookean
<b>Grogan et al. (2011)</b>	3D	Idealised	Plaque	Hyperelastic Polynomial n= 6
<b>Wong et al. (2012)</b>	2D	Realistic – MRI scan	Lipid Pool Fibrous Cap Calcification	Linear Elastic
<b>Cilla et al. (2012)</b>	3D	Idealised	Lipid Pool Plaque	Hyperelastic Neo-Hookean
<b>Garcia et al. (2012)</b>	3D	Idealised	Lipid Pool Plaque Calcification	Hyperelastic Neo-Hookean
<b>Conway et al. (2012)</b>	3D	Idealised/Population Specific	Plaque	Hyperelastic Polynomial n=2 Plastic (range of yield strengths)
<b>Morlacchi et al. (2013)</b>	3D	Realistic –CTA/Patient Specific	Plaque	Hyperelastic Polynomial n=6 Plastic (yield = 400kPa)
<b>Grogan et al. (2013)</b>	3D	Idealised	Plaque	Hyperelastic Polynomial n=2
<b>Morlacchi et al. (2014)</b>	3D	Idealised	Plaque Calcification	Hyperelastic Polynomial n=6
<b>Iannaccone et al. (2014)</b>	3D	Realistic	Fibrotic Media Lipid Pool Fibrous Cap Calcification	Anisotropic Hyperelastic with continuum damage model
<b>Conway et al. (2014)</b>	3D	Idealised/Population Specific	Plaque Lipid Pool Calcification	Hyperelastic Polynomial n=2, Ogden n=1 & n=6 Plasticity & Pseudo-elasticity
<b>Karimi et al. (2014)</b>	3D	Idealised	Plaque Calcified Cellular Hypocellular	Hyperelastic Mooney-Rivlin
<b>Karimi et al. (2014a)</b>	3D	Idealised	Plaque Calcified Cellular Hypocellular	Hyperelastic Ogden n=3
<b>Schiavone and Zhao (2015)</b>	3D	Idealised	Plaque Hypocellular Calcification	Hyperelastic Polynomial n=6, Ogden n=1
<b>Fan et al. (2016)</b>	3D	Realistic – MRI scan	Lipid Pool Fibrous Cap Calcification	Hyperelastic Mooney-Rivlin
<b>Conway et al. (2017)</b>	3D	Idealised	Plaque Calcification	Hyperelastic Polynomial n=2, Ogden n=1 & n=6 Plasticity & Pseudo-elasticity
<b>Gökgöl et al. (2017)</b>	3D	Idealised	Plaque Calcification	Hyperelastic Yeoh Plasticity

### 2.3.1 Inelasticity and damage modelling approaches

In a fracture mechanics approach, plaque damage and rupture are addressed as a crack initiation and growth problem, other studies use cohesive zone/interface debonding models to simulate material failure. In the work of Gasser and Holzapfel (2007), delamination between material boundaries are modelled using the interface element method (IEM) and the partition of unity finite element method (PUFEM) is implemented to simulate the fracturing of layers. The fractured model is shown in Figure 2.6 whereby the model failed at the shoulders of the plaque. Other examples of studies using fracture mechanics include: Versluis et al. (2006); Ferrara and Pandolfi (2008); Nguyen and Levy (2010); Pei et al. (2013); Leng et al. (2015a, 2015b) and Merei et al. (2017) investigated the use of cohesive zone modelling to model the delamination of the plaque from the arterial wall in mouse models.

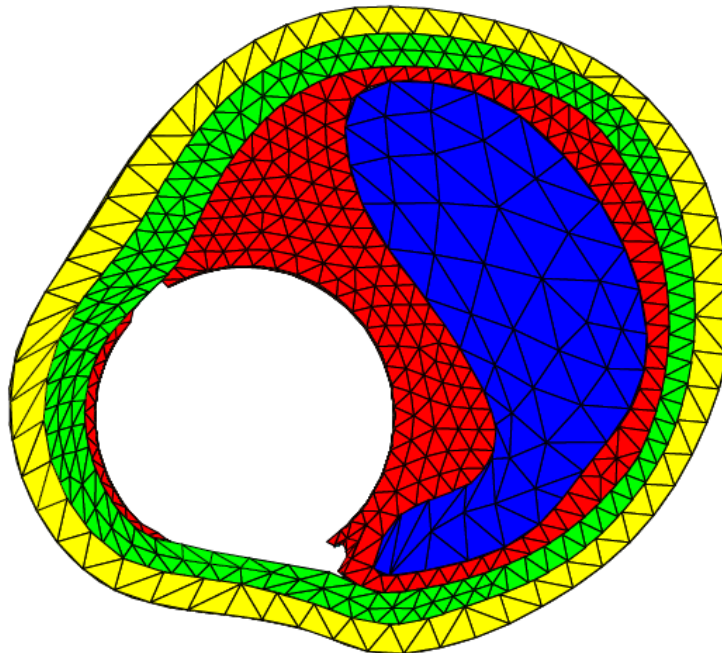


Figure 2.6. Deformed plaque lesion undergoing balloon expansion in the lumen. Partition of unity finite element method (PUFEM) and interface element method (IEM) modelling approach is used to capture the damage in the model. Partitioned elements have been

removed for clarity and each colour represents a different material type (red = intima, blue = lipid pool, green=media and yellow=adventitia) (Gasser and Holzapfel, 2007).

The continuum damage mechanics approach, as described above in section 2.3.1., where the plaque is modelled as a homogeneous continuum and with parameters introduced to represent permanent deformation (inelastic strain) and damage (damage parameter). Examples of studies in this category include: Maher et al. (2011); Balzani et al. (2012) and Iannaccone et al. (2014).

Pseudo-elasticity and elasto-plasticity damage approaches have also been used in atherosclerotic plaque modelling. Pseudo-elastic modelling has been implemented by Conway et al. (2014) to account for plaque damage in a computational model of stent angioplasty motivated by the presence of the Mullins effect in experimental cyclic stress-strain data for plaque tissue (see Figure 2.7). In the elasto-plastic approach, the tissue is idealised as an isotropic elastic-perfectly plastic material, where the plasticity is characterised by von-Mises plasticity, with a yield stress determined from reported plaque stress-strain data. Examples of studies that utilise elasto-plasticity are: Gökgöl et al. (2017); Gastaldi et al. (2010); Conway et al. (2012) and Conway et al. (2014), where the Loree et al. (1994) data was used to identify a plaque yield stress of 400 kPa.

In continuum damage mechanics, pseudo-elasticity and elasto-plasticity are very useful phenomenological modelling approaches to incorporate plaque tissue damage into computational models. While attractive in terms of ease of implementation, they are highly idealised and not physically based as they do not account directly for the microstructural deformation and failure mechanisms that are at play in the material, in particular given the structural heterogeneity of the material.



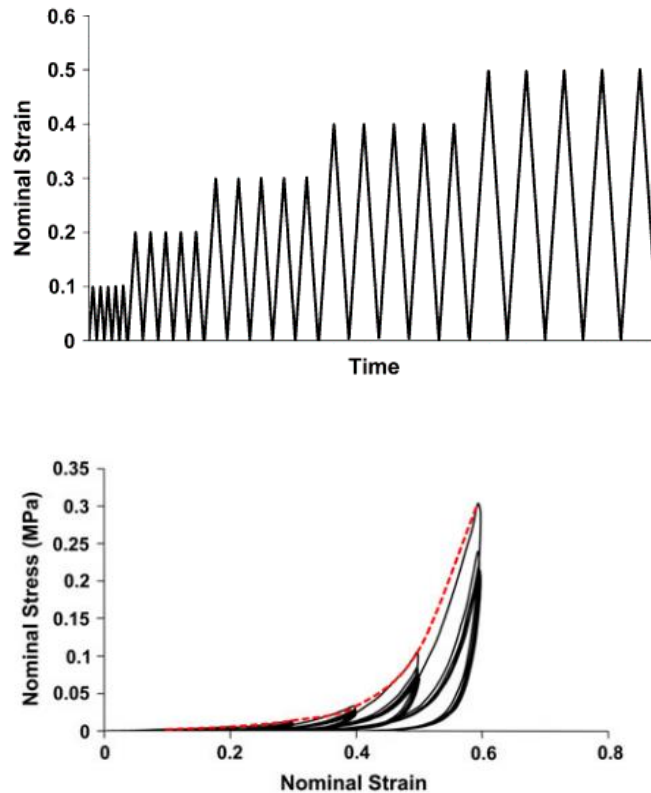


Figure 2.7. Data on cyclic compression testing of atherosclerotic plaque samples (human carotid plaque) from Maher et al. (2011): (top) incremental cyclic loading history, and (bottom) a typical stress-strain response (the dotted line represents the load envelope of the tissue).

## 2.4 Plaque Rupture Stress

In an attempt to characterise the mechanical strength of atherosclerotic plaque tissue, and to aid in assessing tissue rupture risk, significant attention has been paid in the literature to the identification of a “plaque rupture stress”. These efforts have typically involved mechanical testing of diseased arterial tissue, backed up by computational modelling. Modelling is used to calculate the local peak tissue stress at the point of macroscopic tissue rupture, thereby identifying the rupture stress value (see Cardoso and Weinbaum (2014), and Gijssen and Migliavacca (2014)). Using such an approach, a very widely cited plaque rupture stress threshold of 300 kPa was established by Cheng et al. (1993). Cheng

et al. (1993) also reported an average rupture stress of  $545 \pm 160$  kPa. The measure of stress used here was the peak circumferential stress (PCS), the local stress component in the arterial circumferential direction.

In terms of using such data in computational models to assess tissue rupture risk, arguably the best stress component to compare with these rupture values is the maximum principal stress, since it can be argued that it is more representative of a critically loaded condition in a soft predominantly elastic fibrous material. In contrast to von-Mises stress, which is more representative of a critically loaded condition in predominantly plastically deforming materials that fail through shape distortion deformation modes (such as ductile metals). Nonetheless, useful critical von-Mises stress data has also been reported for vulnerable plaque as material lying between 227 and 683 kPa. (Li et al., 2006)

Not surprisingly, rupture stresses has been found to be highly variable, depending on the plaque type examined; for example 342 kPa for lipid dominant plaque and 618 kPa for calcified plaque (Mulvihill et al., 2013). Weinbaum and co-workers (Cardoso and Weinbaum, 2014; Kelly-Arnold et al., 2013; Maldonado et al., 2012) have focussed on vulnerable cap rupture stress, finding that the high stress concentrations around micro-calcifications (increasing stresses up to x15) could significantly lower effective rupture stresses for such tissue. In Figure 2.8 below the nominal value of 300 kPa, with a value of 107 kPa reported by Maldonado et al. (2012).

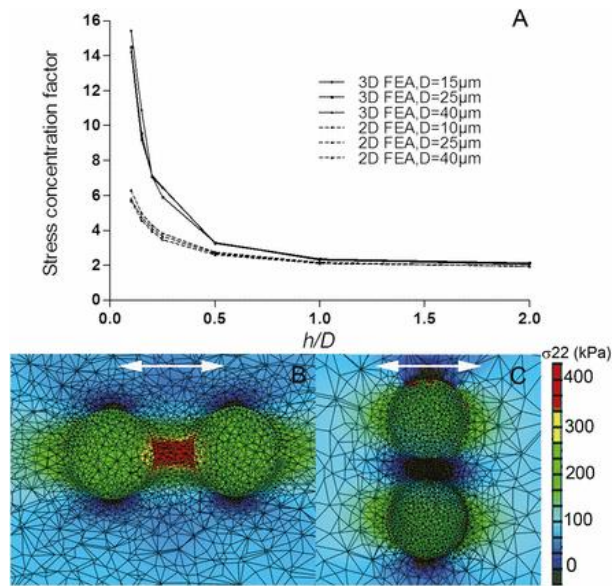


Figure 2.8. (A) illustrates the computational results for the analysis of stress concentrations caused by calcifications in a soft tissue matrix, and the relationship between the separation distance and the diameter, given by  $h$  and  $D$  respectively. The finite element results for particles of  $h/D$  of 0.4 oriented along the (B) tensile and (C) transverse loading axis (Kelly-Arnold et al., 2013).

## 2.5 Applications in Stent Angioplasty

As is clear from the above sections, the development of tissue constitutive and damage models to enable the physically representative computational modelling of vascular interventions, such as stent angioplasty, is of significant interest to the computational biomechanics community. This has, in part, been fuelled by the industrial need for numerical simulations of medical device performance as part of medical device regulatory approval process, for example the US Food and Drug Administration (FDA) requirements for the computational modelling of stent performance in angioplasty as part of their regulatory approval process.

While the literature on the computational modelling of stenting is vast, studies (see Table 2.2) that have included explicit representations of plaque tissue sub-structure and constituents are quite rare. This is surprising, given what is now known on the importance

of having an accurate plaque tissue representation in computational models of this type, as reviewed in detail above. Examples of such studies include: Holzapfel et al. (2005); García et al. (2012); Iannaccone et al. (2014); Morlacchi et al. (2014) and Conway et al. (2014).

### 2.5.1 Stent design assessment

As a practical application of the considerations discussed above, Conway et al. (2014, 2012) reported on the development of a computational test-bed for coronary angioplasty (using the commercially available finite element software Abaqus (Dassault Systems Simulia, RI, USA)) to facilitate stent mechanical performance assessment as part of the stent design process. In terms of overall arterial model geometry, the work proposed to bridge the gap between the use of highly idealised (straight or moderately curved cylindrical geometries), that have been extensively studied in the literature, and patient specific arterial geometries (generated from medical imaging) that have the limitation that they are by definition relevant for a particular individual, making generalisations difficult. Instead a population specific approach was taken where models for a range of geometrical population categories were created (covering variations in arterial curvature and stenosis level); this has the advantage of being more general than patient specific, yet more representative than a single idealised atherosclerotic arterial model. The population specific arterial geometries are shown in Figure 2.9, with the steps in the stent deployment simulation illustrated in Figure 2.10.

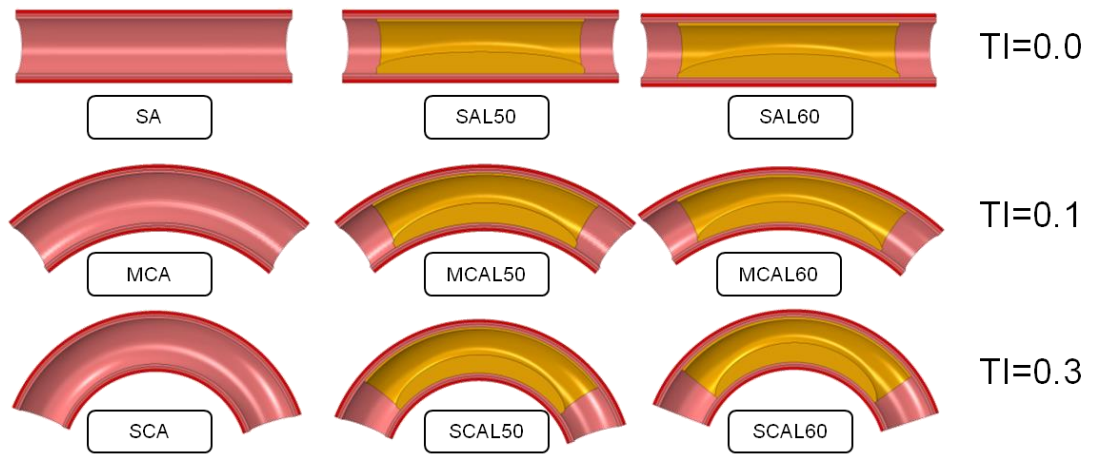


Figure 2.9. The population specific arterial geometries of Conway et al. (2012) covering three levels of curvature: straight artery (SA), moderately curved artery (MA) and severely curved artery (SCA) and three stenosis levels: no stenosis, 50% lesion (L50) and 60% lesion (L60).

A second motivation of this work was to attempt to better inform regulatory body guidelines for medical device approval, in particular the FDA guidelines on computational modelling of stent performance in angioplasty (U.S. Food and Drug Administration, (U.S. Department of Health and Human Services)). It is interesting to note that these guidelines are relatively imprecise in terms of prescribing details on the diseased artery model structure and the range of arterial geometries that should be considered in these analyses, to generate a realistic depiction of device performance in-vivo.

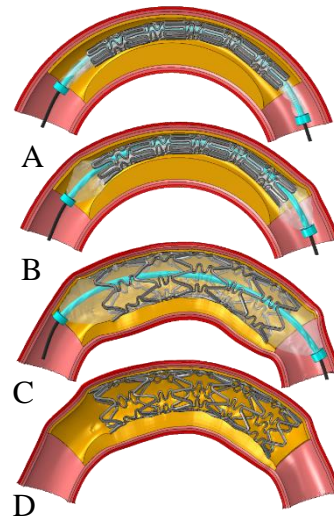


Figure 2.10. Simulation of steps in stent deployment simulation from Conway et al. (2012). A: Pre-deployment; B: Mid-deployment; C: Maximum balloon inflation; D. Post balloon deflation and removal. Case considered is a severely curved artery with 60% lesion (SCAL60), and the Cypher-like stent.

Within the geometrical framework shown in Figure 2.9 a three-layer arterial model (intima, media, adventitia) was implemented using the HGO model described above, with material constants as established in Holzapfel et al. (2005). A wide range of stenotic (plaque) tissue representations were considered. Conway et al. (2012) modelled the tissue as a homogeneous non-linear elastic-plastic material with the non-linear elasticity characterised by a Mooney-Rivlin polynomial hyperelastic model calibrated by Pericevic et al. (2009) to the Loree et al. (1994) experimental data. A range of plaque tissue types (cellular, hypocellular, calcified) with a range of plastic yield stresses (to represent plaque tissue damage) derived from the Loree et al. (1994) data were used. As test cases, the computational test-bed was applied to two stent geometries, based on the closed-cell Cypher stent and the open-cell Multi-Link stent. In Conway et al. (2014) particular focus was applied to the plaque representation to include multiple constituents and constituent

combinations, including matrix tissue, lipid pool (Figure 2.11) and calcified particles (Figure 2.12). In addition, a range of matrix tissue representations was considered, ranging from very soft tissue (using a first-order Ogden hyperelastic model, calibrated from Maher et al. (2011) compressive stress-strain data) to stiffer tissue (using the Mooney-Rivlin polynomial model calibration from Conway et al. (2012)) Finally, two plaque (matrix) tissue damage representations were considered: elasto-plasticity and pseudo-elasticity (using the Ogden and Roxburghy (1999) model, calibrated to the Maher et al. (2011) data (see Figure 2.7)). This computational test-bed formulation allowed for the effects of each of the modelling features and variations to be considered, and insight gained into their relative importance for the practical purpose of stent mechanical performance assessment. Which in turn was assessed through the following measures: stented vessel recoil, stent scaffolding capability (related to radial strength) and tissue damage risk (related to peak tissue stress levels generated).

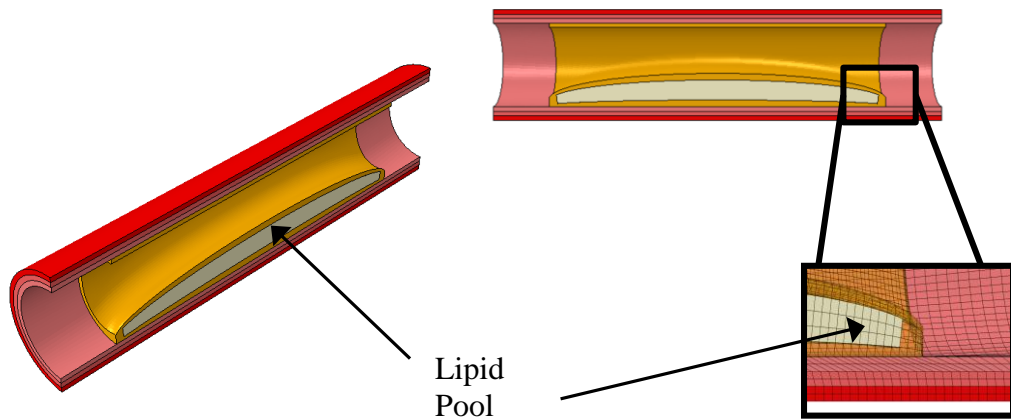


Figure 2.11. Schematic diagram of SAL50 artery model (Figure 2.9) with lipid pool, constituting 9.3% of total atherosclerotic tissue volume. (Conway et al., 2014)

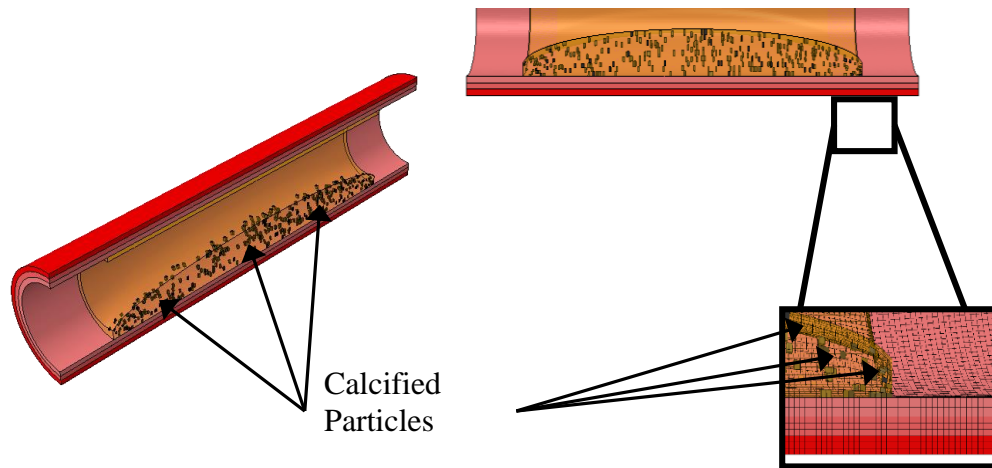


Figure 2.12. Schematic diagram of SAL50 artery model (Figure 2.9) with calcified particles, constituting 0.5% of total atherosclerotic tissue volume. (Conway et al., 2014)

As detailed in Conway et al. (2014, 2012), the results and insights generated are very relevant. In relation to overall arterial geometry (Figure 2.10), one surprising result was that arterial curvature had only a minor influence on the stent performance measures. Relatively speaking, the stenosis level dominated the model predictions, controlling the differentiation between the performance of the two stents (with the open-cell design performing better for larger stenosis levels, and also for greater arterial tortuosity). Leading to the suggestion that stenosis level could be a critically important parameter in stent selection for the clinician.

The constitutive description of the plaque tissue, and its sub-structure details, are seen to be influential in determining stent performance, and it is possible to infer relative importance across the range of plaque tissue modelling features considered. In this context, the choice of plaque tissue matrix properties is seen to dominate the results, indicating the importance of establishing clearly defined plaque tissue types, and achieving representative experimental mechanical characterisation that is tissue type-dependent. It has been observed in other computational stenting studies that calcification present reduces the lumen gain achieved during stenting (García et al., 2012; Pericevic et



al., 2009). Other studies have investigated at the effect of calcification volume, lipid pool geometries, stent oversizing and eccentricity (Buffinton and Ebenstein, 2014; Iannaccone et al., 2014; Pei et al., 2013; Jonathan F Wenk et al., 2010). All of which found effects on the stress states in the plaque demonstrating the importance of considering all geometrical variations and all constituents behaviours when modelling stenting or other medical device deployments.

In relation to damage modelling, the elasto-plasticity approach is significantly more influential on the stress-state than the pseudo-elasticity approach, and this could be related to the significant peak stress limiting effect of the plasticity model on the loading and reloading path, relative to the pseudo-elastic model, as shown in Conway et al. (2014). In relation to plaque tissue sub-structure representation, the presence of calcifications dominated over the presence of the lipid pool in determining stent performance, through increasing vessel recoil (reducing lumen gain) and increasing local tissue stresses Figure 2.13, and in particular Figure 2.13(F)), with the lipid pool only being influential in very soft matrix tissue cases. This emphasises the importance of having more geometrically representative calcified particles in the plaque tissue model, which is consistent with the recent enhanced focus on characterising the mechanical effects of plaque tissue calcification, as noted above in Section 3.4. (Barrett et al., 2016; Cahalane et al., 2018; Cardoso and Weinbaum, 2014; Kelly-Arnold et al., 2013; Maldonado et al., 2012).

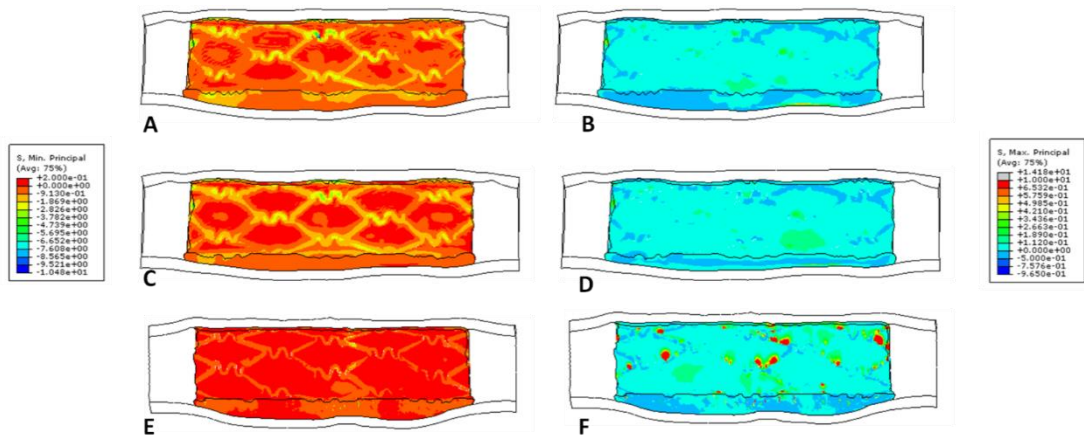


Figure 2.13. Principal stress contour plots (MPa) in the plaque tissue at maximum balloon inflation, for the soft Ogden matrix tissue model and the Cypher-like stent (Conway et al. 2014). Minimum principal stresses (A, C, E); maximum principal stresses (B, D, F); lipid pool (C, D); calcifications (E, F).

A study by García et al. (2012) uses an innovative stent design (Figure 2.14) to help minimise the damage on the endothelium during stenting. It is identified that the location for the maximum radial force should be in the middle of the stent to open the stenosis, but unnecessary damage may be imparted in the non-stenosed area by over expansion. It is found that by reducing the strut thickness at the ends they can reduce the stress in the healthy arterial sections, thus potentially reducing the risk of restenosis. Other studies that have investigated the effects of stent design and sizing on efficacy of stenting include: Gökgöl et al. (2017); He et al. (2019); Gerhard A Holzapfel et al. (2005) and Timmins et al. (2008)

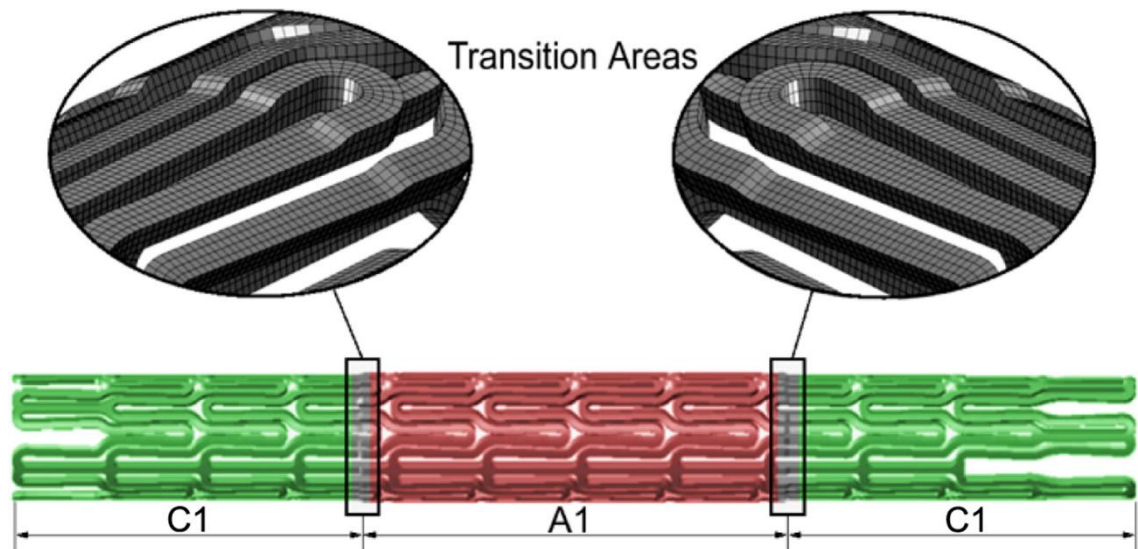


Figure 2.14. A variable stent design that reduces the radial force in each of the sections highlighted C1 as opposed to A1 (García et al., 2012).

Patient specific modelling is of great importance for evaluating the most realistic predictions in stent evaluation. Holzapfel et al. (2005) used a patient specific model (Figure 2.15) generated from an external iliac extracted post-mortem. This was used as an attesting case to evaluate different stent geometries and determine differences in their performances. For examples of additional studies that have explored patient specific plaque geometries see Table 2.2.

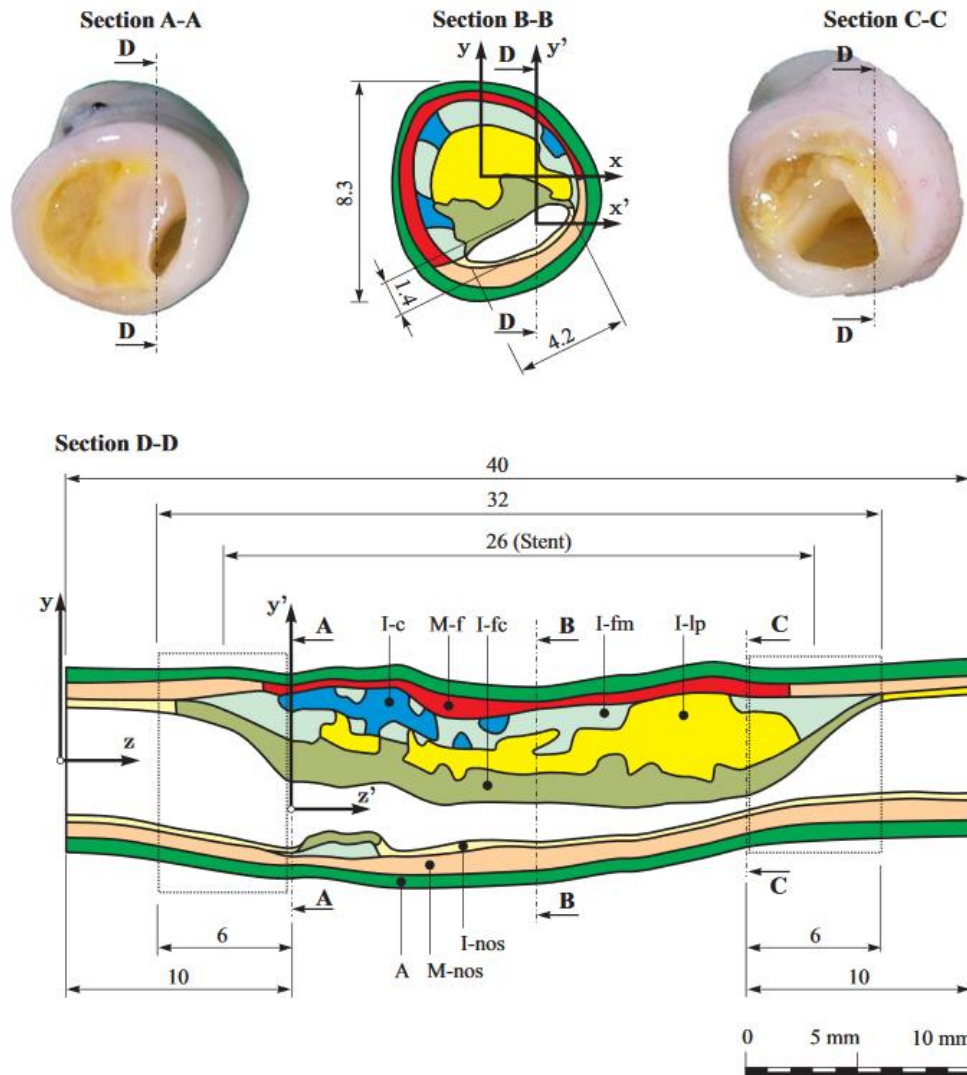


Figure 2.15. Sections of a patient specific atherosclerotic external iliac artery. Section B-B is the region with the smallest lumen diameter of 1.4 mm. The tissue components are: adventitia (A), non-diseased media (M-nos), non-diseased intima (I-nos), fibrous cap (I-fc), lipid pool (I-lp), calcification (I-c), fibrotic intima at the medial border (I-fm) and diseased media (M-f) (Holzapfel et al., 2005).

## 2.6 Discussion

Undoubtedly, despite the practical difficulties in relation to tissue sourcing and testing, significant and important experimental and modelling work has been performed to characterise and represent the mechanical behaviour of atherosclerotic plaque. Significant insights into the mechanical performance of the tissue have been established, and models

have been developed that have proven practically useful in computational modelling investigations of vascular interventions such as stent angioplasty.

However, substantial work remains to be done on a number of aspects of plaque characterisation and modelling. Although difficult, it would be very beneficial if a universal modelling strategy for plaque constituent materials could be established for more straight-forward comparability between stenting studies. It is clear however that this will only be possible when greater experimental characterisation has been performed. Such a standard would be hugely beneficial for the comparison of test data across different studies, and also for the development of future constitutive models.

As indicated above, the modelling of plaque inelasticity and damage to date has primarily been phenomenological in nature. While this is very useful for practical implementation in computational analysis and design studies, it is quite idealised and limited in its ability to accurately capture the details of material deformation and failure. Overall, improved and more physically based constitutive and damage model formulations are required (Holzapfel et al., 2014), that will be more physically accurate and representative in their mechanical performance predictions.

Additionally, one area that has received little attention in the literature is the rate dependence and viscoelasticity of plaque tissue, although the existence of soft tissue viscoelasticity is well accepted. Indeed, the tissue preconditioning cyclic loading that is widely utilised in mechanical testing programmes for soft tissue is largely intended to overcome tissue rate effects and viscoelasticity, and to produce stabilised stress-strain response curves for the testing programme proper. In relation to plaque tissue, Topoleski and Salunke (2000) and Heiland et al. (2013) report a significant time-dependent (stress-relaxation) response for atherosclerotic plaque. On this basis, further experimental work to obtain an accurate characterisation of the rate dependence and viscoelasticity of

homogeneous fibrous plaque tissue would be extremely beneficial, with a view to accounting for such effects in constitutive models. This would significantly enhance the capabilities of computational models, for example in relation to assessing the effects of balloon/stent deployment rate, and tissue strain recovery and stress relaxation over time.

As discussed in Holzapfel et al. (2014), stresses in diseased tissue models are very sensitive to small changes in the mechanical environment. Furthermore, the mechanical properties can vary significantly from patient to patient therefore an in-vivo method should be used for evaluating the mechanical properties of all the tissue components. Unfortunately, the technology, infrastructure, and computational power to carry out these kinds of balloon or stenting simulations pre-operation are not feasible for implementation. It is the author's opinion that the investigation of trends in plaque configurations with regard to risk assessment is essential in evaluating the safety of balloon angioplasty and stenting.

## 2.7 References

- Akyildiz, A.C., Gijssen, F.J.H., Mulvihill, J.J., Walsh, M.T., Holzapfel, G.A., Cunnane, E.M., 2014. Uniaxial tensile testing approaches for characterisation of atherosclerotic plaques. *J. Biomech.* 47, 793–804. <https://doi.org/10.1016/j.jbiomech.2014.01.017>
- Akyildiz, A.C., Speelman, L., Gijssen, F.J.H., 2014. Mechanical properties of human atherosclerotic intima tissue. *J. Biomech.* 47, 773–783. <https://doi.org/10.1016/j.jbiomech.2014.01.019>
- Balzani, D., Brinkhues, S., Holzapfel, G.A., 2012. Constitutive framework for the modeling of damage in collagenous soft tissues with application to arterial walls. *Comput. Methods Appl. Mech. Eng.* 213–216, 139–151. <https://doi.org/10.1016/j.cma.2011.11.015>
- Barrett, H.E., Cunnane, E.M., Kavanagh, E.G., Walsh, M.T., 2016. On the effect of calcification volume and configuration on the mechanical behaviour of carotid plaque tissue. *J. Mech. Behav. Biomed. Mater.* 56, 45–56. <https://doi.org/10.1016/j.jmbbm.2015.11.001>
- Barrett, S.R.H., Sutcliffe, M.P.F., Howarth, S., Li, Z.Y., Gillard, J.H., 2009. Experimental measurement of the mechanical properties of carotid atherothrombotic plaque fibrous cap. *J. Biomech.* 42, 1650–1655. <https://doi.org/10.1016/j.jbiomech.2009.04.025>
- Bluestein, D., Alemu, Y., Avrahami, I., Gharib, M., Dumont, K., Ricotta, J.J., Einav, S., 2008. Influence of microcalcifications on vulnerable plaque mechanics using FSI modeling. *J. Biomech.* 41, 1111–1118. <https://doi.org/10.1016/j.jbiomech.2007.11.029>
- Buffinton, C.M., Ebenstein, D.M., 2014. Effect of Calcification Modulus and Geometry on Stress in Models of Calcified Atherosclerotic Plaque. *Cardiovasc. Eng. Technol.* 5, 244–260. <https://doi.org/10.1007/s13239-014-0186-6>
- Cahalane, R.M., Barrett, H.E., O’Brien, J.M., Kavanagh, E.G., Moloney, M.A., Walsh, M.T., 2018. Relating the mechanical properties of atherosclerotic calcification to radiographic density: A nanoindentation approach. *Acta Biomater.* 80, 228–236. <https://doi.org/10.1016/j.actbio.2018.09.010>
- Cardoso, L., Weinbaum, S., 2014. Changing views of the biomechanics of vulnerable plaque rupture: A review. *Ann. Biomed. Eng.* 42, 415–431. <https://doi.org/10.1007/s10439-013-0855-x>
- Chai, C.K., Akyildiz, A.C., Speelman, L., Gijssen, F.J.H., Oomens, C.W.J., van Sambeek, M.R.H.M., van der Lugt, A., Baaijens, F.P.T., 2014a. Local anisotropic mechanical properties of human carotid atherosclerotic plaques - Characterisation by micro-indentation and inverse finite element analysis. *J. Mech. Behav. Biomed. Mater.* 43, 59–68. <https://doi.org/10.1016/j.jmbbm.2014.12.004>
- Chai, C.K., Speelman, L., Oomens, C.W.J., Baaijens, F.P.T., 2014b. Compressive mechanical properties of atherosclerotic plaques - Indentation test to characterise the local anisotropic behaviour. *J. Biomech.* 47, 784–792. <https://doi.org/10.1016/j.jbiomech.2014.01.018>

- Cheng, G.G., Loree, H.M., Kamm, R.D., Fishbein, M.C., Lee, R.T., 1993. Distribution of Circumferential Stress in Ruptured and Stable Atherosclerotic Lesions. *Circulation* 87, 1179–1187.
- Chhabra, L., Zain, M.A., Siddiqui, W.J., 2019. *Coronary Stents*. StatPearls Publishing.
- Chua, S.N.D., MacDonald, B.J., Hashmi, M.S.J., 2004. Finite element simulation of slotted tube (stent) with the presence of plaque and artery by balloon expansion. *J. Mater. Process. Technol.* 155–156, 1772–1779. <https://doi.org/10.1016/j.jmatprotec.2004.04.396>
- Cilla, M., Peña, E., Martínez, M.A., 2012. 3D computational parametric analysis of eccentric atheroma plaque: Influence of axial and circumferential residual stresses. *Biomech. Model. Mechanobiol.* 11, 1001–1013. <https://doi.org/10.1007/s10237-011-0369-0>
- Conway, C., McGarry, J.P., Edelman, E.R., McHugh, P.E., 2017. Numerical Simulation of Stent Angioplasty with Predilatation: An Investigation into Lesion Constitutive Representation and Calcification Influence. *Ann. Biomed. Eng.* 45, 2244–2252. <https://doi.org/10.1007/s10439-017-1851-3>
- Conway, C., McGarry, J.P., McHugh, P.E., 2014. Modelling of Atherosclerotic Plaque for Use in a Computational Test-Bed for Stent Angioplasty. *Ann. Biomed. Eng.* 42, 2425–2439. <https://doi.org/10.1007/s10439-014-1107-4>
- Conway, C., Sharif, F., McGarry, J.P., McHugh, P.E., 2012. A Computational Test-Bed to Assess Coronary Stent Implantation Mechanics Using a Population-Specific Approach. *Cardiovasc. Eng. Technol.* 3, 374–387. <https://doi.org/10.1007/s13239-012-0104-8>
- Cunnane, E.M., Mulvihill, J.J.E., Barrett, H.E., Healy, D.A., Kavanagh, E.G., Walsh, S.R., Walsh, M.T., 2015. Mechanical, biological and structural characterization of human atherosclerotic femoral plaque tissue. *Acta Biomater.* 11, 295–303. <https://doi.org/10.1016/j.actbio.2014.09.024>
- Cunnane, E.M., Mulvihill, J.J.E., Barrett, H.E., Hennessy, M.M., Kavanagh, E.G., Walsh, M.T., 2016. Mechanical properties and composition of carotid and femoral atherosclerotic plaques: A comparative study. *J. Biomech.* 49, 3697–3704. <https://doi.org/10.1016/j.jbiomech.2016.09.036>
- Ebenstein, D.M., Coughlin, D., Chapman, J., Li, C., Pruitt, L.A., 2009. Nanomechanical properties of calcification, fibrous tissue, and hematoma from atherosclerotic plaques. *J. Biomed. Mater. Res. - Part A* 91, 1028–1037. <https://doi.org/10.1002/jbm.a.32321>
- European Heart Network, 2017. *European Cardiovascular Disease Statistics 2017 – European Heart Network* [WWW Document]. URL <http://www.ehnheart.org/cvd-statistics.html/> (accessed 26/04/2019)
- Fan, Z.M., Liu, X., Du, C.F., Sun, A.Q., Zhang, N., Fan, Z.M., Fan, Y.B., Deng, X.Y., 2016. Plaque components affect wall stress in stented human carotid artery: A numerical study. *Acta Mech. Sin. Xuebao* 32, 1149–1154. <https://doi.org/10.1007/s10409-016-0572-4>



- Ferrara, A., Pandolfi, A., 2008. Numerical modelling of fracture in human arteries. *Comput. Methods Biomech. Biomed. Engin.* 11, 553–567. <https://doi.org/10.1080/10255840701771743>
- García, A., Peña, E., Martínez, M.A., 2012. Influence of geometrical parameters on radial force during self-expanding stent deployment. Application for a variable radial stiffness stent. *J. Mech. Behav. Biomed. Mater.* 10, 166–175. <https://doi.org/10.1016/j.jmbbm.2012.02.006>
- Gasser, T.C., Holzapfel, G.A., 2007. Modeling plaque fissuring and dissection during balloon angioplasty intervention. *Ann. Biomed. Eng.* 35, 711–23. <https://doi.org/10.1007/s10439-007-9258-1>
- Gastaldi, D., Morlacchi, S., Nichetti, R., Capelli, C., Dubini, G., Petrini, L., Migliavacca, F., 2010. Modelling of the provisional side-branch stenting approach for the treatment of atherosclerotic coronary bifurcations: Effects of stent positioning. *Biomech. Model. Mechanobiol.* 9, 551–561. <https://doi.org/10.1007/s10237-010-0196-8>
- Gijssen, F.J.H., Migliavacca, F., 2014. Plaque mechanics. *J. Biomech.* 47, 763–764. <https://doi.org/10.1016/j.jbiomech.2014.01.031>
- Gökgöl, C., Diehm, N., Büchler, P., 2017. Numerical Modeling of Nitinol Stent Oversizing in Arteries with Clinically Relevant Levels of Peripheral Arterial Disease: The Influence of Plaque Type on the Outcomes of Endovascular Therapy. *Ann. Biomed. Eng.* 45, 1420–1433. <https://doi.org/10.1007/s10439-017-1803-y>
- Grogan, J.A., Leen, S.B., McHugh, P.E., 2013. Optimizing the design of a bioabsorbable metal stent using computer simulation methods. *Biomaterials* 34, 8049–8060. <https://doi.org/10.1016/j.biomaterials.2013.07.010>
- Grogan, J.A., O'Brien, B.J., Leen, S.B., McHugh, P.E., 2011. A corrosion model for bioabsorbable metallic stents. *Acta Biomater.* 7, 3523–3533. <https://doi.org/10.1016/j.actbio.2011.05.032>
- Gu, L., Zhao, S., Muttyam, A.K., Hammel, J.M., 2010. The Relation Between the Arterial Stress and Restenosis Rate After Coronary Stenting. *J. Med. Device.* 4, 031005. <https://doi.org/10.1115/1.4002238>
- He, H. peng, Weng, J. cheng, Zhao, Y., Cai, S. hong, Zhang, X. ling, Yin, H. hui, 2019. Impact of Plaque Calcification and Stent Oversizing on Clinical Outcomes of Atherosclerotic Femoropopliteal Arterial Occlusive Disease Following Stent Angioplasty. *Eur. J. Vasc. Endovasc. Surg.* 58, 215–222. <https://doi.org/10.1016/j.ejvs.2019.01.025>
- Heiland, V.M., Forsell, C., Roy, J., Hedin, U., Gasser, T.C., 2013. Identification of carotid plaque tissue properties using an experimental-numerical approach. *J. Mech. Behav. Biomed. Mater.* 27, 226–238. <https://doi.org/10.1016/j.jmbbm.2013.05.001>
- Holzapfel, G.A., Mulvihill, J.J., Cunnane, E.M., Walsh, M.T., 2014. Computational approaches for analyzing the mechanics of atherosclerotic plaques: A review. *J. Biomech.* 47, 859–869. <https://doi.org/10.1016/j.jbiomech.2014.01.011>

- Holzapfel, G.A., Sommer, G., Gasser, C.T., Regitnig, P., 2005. Determination of layer-specific mechanical properties of human coronary arteries with nonatherosclerotic intimal thickening and related constitutive modeling. *Am. J. Physiol. Circ. Physiol.* 289, H2048–H2058. <https://doi.org/10.1152/ajpheart.00934.2004>
- Holzapfel, G.A., Sommer, G., Regitnig, P., 2004. Anisotropic Mechanical Properties of Tissue Components in Human Atherosclerotic Plaques. *J. Biomech. Eng.* 126, 657. <https://doi.org/10.1115/1.1800557>
- Holzapfel, G.A., Stadler, M., Gasser, T.C., 2005. Changes in the Mechanical Environment of Stenotic Arteries During Interaction With Stents: Computational Assessment of Parametric Stent Designs. *J. Biomech. Eng.* 127, 166–180. <https://doi.org/10.1115/1.1835362>
- Iannaccone, F., Debusschere, N., De Bock, S., De Beule, M., Van Loo, D., Vermassen, F., Segers, P., Verheghe, B., 2014. The influence of vascular anatomy on carotid artery stenting: A parametric study for damage assessment. *J. Biomech.* 47, 890–898. <https://doi.org/10.1016/j.jbiomech.2014.01.008>
- iDataResearch, 2018. Over 1.8 Million Stents Implanted per Year in the U.S. - iData Research [WWW Document]. URL <https://idataresearch.com/over-1-8-million-stents-implanted-per-year-in-the-u-s/> (accessed 10.20.19)
- Irish Heart foundation, 2018. More than 9,000 lives lost to cardiovascular disease in 2016. – Irish Heart Foundation [WWW Document]. URL <https://irishheart.ie/news/more-than-9000-lives-lost-to-cardiovascular-disease-in-2016/> (accessed 26/04/2019)
- Karimi, A., Navidbakhsh, M., Razaghi, R., 2014a. A finite element study of balloon expandable stent for plaque and arterial wall vulnerability assessment. *J. Appl. Phys.* 116. <https://doi.org/10.1063/1.4891019>
- Karimi, A., Navidbakhsh, M., Shojaei, A., Hassani, K., Faghihi, S., 2014b. Study of plaque vulnerability in coronary artery using mooney-rivlin model: A combination of finite element and experimental method. *Biomed. Eng. - Appl. Basis Commun.* 26, 1–7. <https://doi.org/10.4015/S1016237214500136>
- Karimi, A., Navidbakhsh, M., Yamada, H., Razaghi, R., 2014c. A nonlinear finite element simulation of balloon expandable stent for assessment of plaque vulnerability inside a stenotic artery. *Med. Biol. Eng. Comput.* 52, 589–599. <https://doi.org/10.1007/s11517-014-1163-9>
- Kelly-Arnold, A., Maldonado, N., Laudier, D., Aikawa, E., Cardoso, L., Weinbaum, S., 2013. Revised microcalcification hypothesis for fibrous cap rupture in human coronary arteries. *Proc. Natl. Acad. Sci.* 110, 10741–10746. <https://doi.org/10.1073/pnas.1308814110>
- Kiouis, D.E., Gasser, T.C., Holzapfel, G.A., 2007. A numerical model to study the interaction of vascular stents with human atherosclerotic lesions. *Ann. Biomed. Eng.* 35, 1857–1869. <https://doi.org/10.1007/s10439-007-9357-z>
- Kolandaivelu, K., Leiden, B.B., Edelman, E.R., 2014. Predicting response to endovascular therapies: Dissecting the roles of local lesion complexity, systemic

- comorbidity, and clinical uncertainty. *J. Biomech.* 47, 908–921. <https://doi.org/10.1016/j.jbiomech.2014.01.006>
- Lawlor, M.G., O'Donnell, M.R., O'Connell, B.M., Walsh, M.T., 2011. Experimental determination of circumferential properties of fresh carotid artery plaques. *J. Biomech.* 44, 1709–1715. <https://doi.org/10.1016/j.jbiomech.2011.03.033>
- Lee, R.T., Grodzinsky, A.J., Frank, E.H., Kamm, R.D., Schoen, F.J., 1991. Structure-dependent dynamic mechanical behavior of fibrous caps from human atherosclerotic plaques. *Circulation* 83, 1764–1770. <https://doi.org/10.1161/01.CIR.83.5.1764>
- Lee, R.T., Richardson, S.G., Grodzinsky, A.J., Loree, H.M., Gharib, S.A., Tong, L., Pandian, N., 1992. Prediction of mechanical properties of human atherosclerotic tissue by high-frequency intravascular ultrasound imaging. *Arterioscler. Thromb. Vasc. Biol.* 23, 1–5. [https://doi.org/10.1016/0735-1097\(91\)91342-c](https://doi.org/10.1016/0735-1097(91)91342-c)
- Leng, X., Chen, X., Deng, X., Sutton, M.A., Lessner, S.M., 2015a. Modeling of Experimental Atherosclerotic Plaque Delamination. *Ann. Biomed. Eng.* 43, 2838–2851. <https://doi.org/10.1007/s10439-015-1357-9>
- Leng, X., Chen, X., Deng, X., Sutton, M.A., Lessner, S.M., 2015b. Simulation of Atherosclerotic Plaque Delamination Using the Cohesive Zone Model. *Conf. Proc. Soc. Exp. Mech. Ser.* 63, 81–88. [https://doi.org/10.1007/978-3-319-06974-6\\_12](https://doi.org/10.1007/978-3-319-06974-6_12)
- Li, Z.Y., Howarth, S., Trivedi, R.A., U-King-Im, J.M., Graves, M.J., Brown, A., Wang, L., Gillard, J.H., 2006. Stress analysis of carotid plaque rupture based on in vivo high resolution MRI. *J. Biomech.* 39, 2611–2622. <https://doi.org/10.1016/j.jbiomech.2005.08.022>
- Loree, H.M., Grodzinsky, A.J., Park, S.Y., Gibson, L.J., Lee, R.T., 1994. Static circumferential tangential modulus of human atherosclerotic tissue. *J. Biomech.* 27, 195–204. [https://doi.org/10.1016/0021-9290\(94\)90209-7](https://doi.org/10.1016/0021-9290(94)90209-7)
- Maher, E., Creane, A., Sultan, S., Hynes, N., Lally, C., Kelly, D.J., 2011. Inelasticity of Human Carotid Atherosclerotic Plaque. *Ann. Biomed. Eng.* 39, 2445–2455. <https://doi.org/10.1007/s10439-011-0331-4>
- Maher, E., Creane, A., Sultan, S., Hynes, N., Lally, C., Kelly, D.J., 2009. Tensile and compressive properties of fresh human carotid atherosclerotic plaques. *J. Biomech.* 42, 2760–2767. <https://doi.org/10.1016/j.jbiomech.2009.07.032>
- Maldonado, N., Kelly-Arnold, A., Vengrenyuk, Y., Laudier, D., Fallon, J.T., Virmani, R., Cardoso, L., Weinbaum, S., 2012. A mechanistic analysis of the role of microcalcifications in atherosclerotic plaque stability: potential implications for plaque rupture. *Am. J. Physiol. Circ. Physiol.* 303, H619–H628. <https://doi.org/10.1152/ajpheart.00036.2012>
- Merei, B., Badel, P., Davis, L., Sutton, M.A., Avril, S., Lessner, S.M., 2017. Atherosclerotic plaque delamination: Experiments and 2D finite element model to simulate plaque peeling in two strains of transgenic mice. *J. Mech. Behav. Biomed. Mater.* 67, 19–30. <https://doi.org/10.1016/j.jmbbm.2016.12.001>

- Migliavacca, F., Gervaso, F., Prosi, M., Zunino, P., Minisini, S., Formaggia, L., Migliavacca, F., Gervaso, F., Prosi, M., Zunino, P., Minisini, S., Formaggia, L., Dubini, G., 2007. Expansion and drug elution model of a coronary stent. *Comput. Methods Biomech. Biomed. Engin.* 10, 63–73. <https://doi.org/http://dx.doi.org/10.1080/10255840601071087>
- Migliavacca, F., Petrini, L., Massarotti, P., Schievano, S., Auricchio, F., Dubini, G., 2004. Stainless and shape memory alloy coronary stents: A computational study on the interaction with the vascular wall. *Biomech. Model. Mechanobiol.* 2, 205–217. <https://doi.org/10.1007/S10237-004-0039-6>
- Morlacchi, S., Colleoni, S.G., Cárdenes, R., Chiastra, C., Diez, J.L., Larrabide, I., Migliavacca, F., 2013. Patient-specific simulations of stenting procedures in coronary bifurcations: Two clinical cases. *Med. Eng. Phys.* 35, 1272–1281. <https://doi.org/10.1016/j.medengphy.2013.01.007>
- Morlacchi, S., Migliavacca, F., 2013. Modeling stented coronary arteries: Where we are, where to go. *Ann. Biomed. Eng.* 41, 1428–1444. <https://doi.org/10.1007/s10439-012-0681-6>
- Morlacchi, S., Pennati, G., Petrini, L., Dubini, G., Migliavacca, F., 2014. Influence of plaque calcifications on coronary stent fracture: A numerical fatigue life analysis including cardiac wall movement. *J. Biomech.* 47, 899–907. <https://doi.org/10.1016/j.jbiomech.2014.01.007>
- Mulvihill, J.J., Cunnane, E.M., McHugh, S.M., Kavanagh, E.G., Walsh, S.R., Walsh, M.T., 2013. Mechanical, biological and structural characterization of in vitro ruptured human carotid plaque tissue. *Acta Biomater.* 9, 9027–9035. <https://doi.org/10.1016/j.actbio.2013.07.012>
- Nguyen, C.M., Levy, A.J., 2010. The mechanics of atherosclerotic plaque rupture by inclusion/matrix interfacial decohesion. *J. Biomech.* 43, 2702–2708. <https://doi.org/10.1016/j.jbiomech.2010.06.012>
- Ogden, R.W., Roxburghy, D.G., 1999. A pseudo-elastic model for the Mullins effect in filled rubber. *Proc. R. Soc. Lond. A Math. Phys. Sci.* 455, 2861–2877.
- Pant, S., Limbert, G., Curzen, N.P., Bressloff, N.W., 2011. Multiobjective design optimisation of coronary stents. *Biomaterials* 32, 7755–7773. <https://doi.org/10.1016/j.biomaterials.2011.07.059>
- Peach, G., Griffin, M., Jones, K.G., Thompson, M.M., Hinchliffe, R.J., 2012. Diagnosis and management of peripheral arterial disease. *BMJ* 345. <https://doi.org/10.1136/bmj.e5208>
- Pei, X., Wu, B., Li, Z.-Y., 2013. Fatigue Crack Propagation Analysis of Plaque Rupture. *J. Biomech. Eng.* 135, 101003. <https://doi.org/10.1115/1.4025106>
- Pericevic, I., Lally, C., Toner, D., Kelly, D.J., 2009. The influence of plaque composition on underlying arterial wall stress during stent expansion: The case for lesion-specific stents. *Med. Eng. Phys.* 31, 428–433. <https://doi.org/10.1016/j.medengphy.2008.11.005>

- Petrini, L., Migliavacca, F., Dubini, G., F. Auricchio, 2003. Numerical analysis of vascular stents exploiting shape-memory-alloy behavior. 16th {AIMETA} {C}ongress {T}heoretical {A}ppplied {M}echanics 1–10.
- Razzouk, L., Rockman, C.B., Patel, M.R., Guo, Y., Adeiman, M.A., Riles, T.S., Berger, J.S., 2015. Co-existence of vascular disease in differential arterial beds: Peripheral artery disease and carotid artery stenosis. *Atherosclerosis* 241, 687–691. <https://doi.org/10.1016/j.atherosclerosis.2015.06.029>.Co-existence
- Sadat, U., Li, Z.Y., Young, V.E., Graves, M.J., Boyle, J.R., Warburton, E.A., Varty, K., O'Brien, E., Gillard, J.H., 2010. Finite element analysis of vulnerable atherosclerotic plaques: A comparison of mechanical stresses within carotid plaques of acute and recently symptomatic patients with carotid artery disease. *J. Neurol. Neurosurg. Psychiatry* 81, 286–289. <https://doi.org/10.1136/jnnp.2009.190363>
- Salunke, N.V., Topoleski, L.D.T., Humphrey, J.D., Mergner, W.J., 2001. Compressive stress-relaxation of human atherosclerotic plaque. *J. Biomed. Mater. Res.* 55, 236–241. [https://doi.org/10.1002/1097-4636\(200105\)55:2<236::AID-JBM1010>3.0.CO;2-F](https://doi.org/10.1002/1097-4636(200105)55:2<236::AID-JBM1010>3.0.CO;2-F)
- Schiavone, A., Zhao, L.G., 2015. A study of balloon type, system constraint and artery constitutive model used in finite element simulation of stent deployment. *Mech. Adv. Mater. Mod. Process.* 1, 1–15. <https://doi.org/10.1186/s40759-014-0002-x>
- Stary, H.C., 1999. *An atlas of atherosclerosis : progression and regression*. Parthenon Pub. Group.
- Tang, D., Teng, Z., Canton, G., Hatsukami, T.S., Dong, L., Huang, X., Yuan, C., 2009a. Local critical stress correlates better than global maximum stress with plaque morphological features linked to atherosclerotic plaque vulnerability: An in vivo multi-patient study. *Biomed. Eng. Online* 8, 1–9. <https://doi.org/10.1186/1475-925X-8-15>
- Tang, D., Yang, C., Kobayashi, S., 2009b. 3D MRI-Based Anisotropic FSI Models with Cyclic Bending for Human Coronary Atherosclerotic Plaque Mechanical Analysis. *J Biomech Eng.* 131. <https://doi.org/10.1115/1.3127253>.3D
- Teng, Z., Tang, D., Zheng, J., Woodard, P.K., Hoffman, A.H., 2009. An experimental study on the ultimate strength of the adventitia and media of human atherosclerotic carotid arteries in circumferential and axial directions. *J. Biomech.* 42, 2535–2539. <https://doi.org/10.1016/j.jbiomech.2009.07.009>
- Timmins, L.H., Meyer, C.A., Moreno, M.R., Moore, J.E., 2008. Effects of Stent Design and Atherosclerotic Plaque Composition on Arterial Wall Biomechanics. *J. Endovasc. Ther.* 15, 643–654. <https://doi.org/10.1583/08-2443.1>
- Topoleski, L.D.T., Salunke, N.V., 2000. Mechanical behavior of calcified plaques: a summary of compression and stress-relaxation experiments. *Z. Kardiol.* 89, S085–S091. <https://doi.org/10.1007/s003920070105>
- Topoleski, L.D.T., Salunke, N. V., Humphrey, J.D., Mergner, W.J., 1997. Composition- and history-dependent radial compressive behavior of human atherosclerotic plaque. *J. Biomed. Mater. Res.* 35, 117–127. [https://doi.org/10.1002/\(SICI\)1097-4636\(199704\)35:1<117::AID-JBM12>3.0.CO;2-G](https://doi.org/10.1002/(SICI)1097-4636(199704)35:1<117::AID-JBM12>3.0.CO;2-G)

U.S. Department of Health and Human Services, F. and D.A., n.d. Non-Clinical Engineering Tests and Recommended Labeling for Intravascular Stents and Associated Delivery Systems - Guidance for Industry and FDA Staff [WWW Document]. URL <https://www.fda.gov/medicaldevices/deviceregulationandguidance/guidancedocuments/ucm071863.htm> (accessed 4.9.19).

Versluis, A., Bank, A.J., Douglas, W.H., 2006. Fatigue and plaque rupture in myocardial infarction. *J. Biomech.* 39, 339–347. <https://doi.org/10.1016/j.jbiomech.2004.10.041>

Walraevens, J., Willaert, B., De Win, G., Ranftl, A., De Schutter, J., Sloten, J. Vander, 2008. Correlation between compression, tensile and tearing tests on healthy and calcified aortic tissues. *Med. Eng. Phys.* 30, 1098–1104. <https://doi.org/10.1016/j.medengphy.2008.01.006>

Walsh, M.T., Cunnane, E.M., Mulvihill, J.J., Akyildiz, A.C., Gijssen, F.J.H., Holzapfel, G.A., 2014. Uniaxial tensile testing approaches for characterisation of atherosclerotic plaques. *J. Biomech.* 47, 793–804. <https://doi.org/10.1016/j.jbiomech.2014.01.017>

Wenk, J.F., Papadopoulos, P., Zohdi, T.I., 2010. Numerical Modeling of Stress in Stenotic Arteries With Microcalcifications: A Micromechanical Approximation. *J. Biomech. Eng.* 132, 091011. <https://doi.org/10.1115/1.4001351>

Wenk, J.F., Papadopoulos, P., Zohdi, T.I., 2010. Numerical Modeling of Stress in Stenotic Arteries With Microcalcifications: A Micromechanical Approximation. *J. Biomech. Eng.* 132. <https://doi.org/10.1115/1.4001351>

Wong, K.K.L., Thavornpattanapong, P., Cheung, S.C.P., Sun, Z., Tu, J., 2012. Effect of calcification on the mechanical stability of plaque based on a three-dimensional carotid bifurcation model. *BMC Cardiovasc. Disord.* 12. <https://doi.org/10.1186/1471-2261-12-7>

Zahedmanesh, H., John Kelly, D., Lally, C., 2010. Simulation of a balloon expandable stent in a realistic coronary artery-Determination of the optimum modelling strategy. *J. Biomech.* 43, 2126–2132. <https://doi.org/10.1016/j.jbiomech.2010.03.050>

# 3 THEORY

## 3.1 Introduction

The purpose of this chapter is to introduce the fundamental continuum mechanics theoretical background that underlies the computational simulations performed in the later chapters of this thesis. The chapter is structured as follows: Section 3.2 presents key continuum mechanics concepts; Section 3.3 presents the constitutive laws used in this thesis; Section 3.4 presents key concepts and numerical techniques underlying the finite element technique; Section 3.5 presents an overview of cohesive zone modelling of material and interface fracture.

## 3.1 Continuum mechanics

Continuum mechanics entails the study of motion and deformation, the study of stress in the continuum, and the mathematical description of the fundamental laws of physics governing the motion of a continuum (Reddy, 2013). A continuum refers to the assumption that the material being analysed/computed is continuous homogenous matter without gaps or empty spaces. Standard tensor and indicial notation are used throughout this chapter. Tensor/vector components are denoted in **bold** with respect to the standard orthonormal base vectors  $\mathbf{e}_1$ ,  $\mathbf{e}_2$ , and  $\mathbf{e}_3$ . Sample vectors  $\mathbf{u}$  and  $\mathbf{v}$  are used to demonstrate

that the following; the transpose of a vector/tensor is given by the superscript of capital T (example  $\mathbf{u}^T$ ); and the inner product of two vectors is denoted by the following equation:

$$\mathbf{u}\mathbf{v} = \mathbf{u}_1\mathbf{v}_1 + \mathbf{u}_2\mathbf{v}_2 + \mathbf{u}_3\mathbf{v}_3 = \sum_{i=1}^3 \mathbf{u}_i\mathbf{v}_i \quad (3-1)$$

Each component of tensors is defined by the subscripts  $i$  and  $j$ . These indicate the location of the components by defining the  $i^{\text{th}}$  row and the  $j^{\text{th}}$  column in the tensor. In the case of mechanics,  $i_{\text{max}}$  and  $j_{\text{max}}$  are typically 3 as 3x3 tensors.

### 3.1.1 Deformation and motion

A schematic of the deformation and motion of a body is demonstrated in Figure 3.1. A body in the reference configuration  $\Omega_0$  undergoes a motion denoted by  $\chi$  to the current configuration  $\Omega$ . The original position in space of a point P is described by  $\mathbf{X}$  at time 0 and the deformed position is described by  $\mathbf{x}$  at time t.

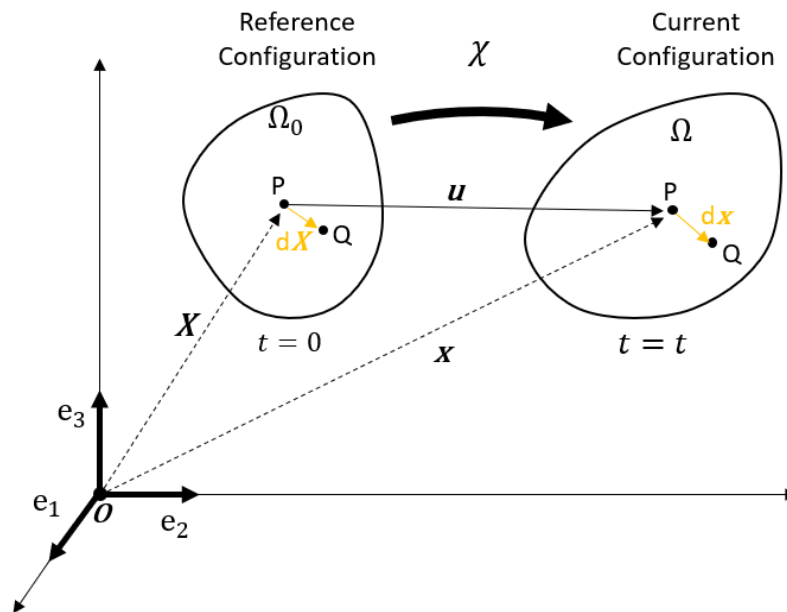




Figure 3.1. Illustration of the deformation and motion of a continuum body in space.

The deformed position for a point  $P$  on a body in space from a reference position over a time  $t$  is described by the following:

$$\mathbf{x} = \chi(\mathbf{X}, t) \quad (3-2)$$

where  $\mathbf{X}$  and  $\mathbf{x}$  define the spatial coordinates of the two positions in relation to the origin  $O$ . The displacement of point  $P$  between the reference and current configuration is described by the vector  $\mathbf{u}$  such that:

$$\mathbf{u} = \mathbf{x} - \mathbf{X} \quad (3-3)$$

Consider the distance between two points  $P$  and  $Q$  on the reference configuration. They are separated by the by the infinitesimal line element  $d\mathbf{X}$  and then in the current configuration they are separated by  $d\mathbf{x}$ . This change in the material points in reference to each other is called the deformation gradient tensor  $\mathbf{F}$  where it is expressed as:

$$\mathbf{F} = \frac{\partial \chi(\mathbf{X}, t)}{\partial \mathbf{X}} = \frac{\partial \mathbf{x}}{\partial \mathbf{X}} \quad (3-4)$$

### 3.1.2 Strain measures

The deformation gradient can be used to define the stretch in a body using the left and right Cauchy-Green tensors  $\mathbf{B}$  and  $\mathbf{C}$  which are described as:

$$\begin{aligned} \mathbf{C} &= \mathbf{F}^T \mathbf{F} \\ \mathbf{B} &= \mathbf{F} \mathbf{F}^T \end{aligned} \quad (3-5)$$

A common strain measure used in continuum mechanics is the Green-Lagrange strain  $\mathbf{E}$  given by:

$$\mathbf{E} = \frac{1}{2} (\mathbf{F}^T \mathbf{F} - \mathbf{I}) \quad (3-6)$$

where the  $\mathbf{I}$  is the identity tensor, whereby  $\mathbf{FI} = \mathbf{F}$ . Another form is index notation which provides:

$$E_{ij} = \frac{1}{2} \left( \frac{\partial u_i}{\partial X_j} + \frac{\partial u_j}{\partial X_i} + \frac{\partial u_k}{\partial X_i} \frac{\partial u_k}{\partial X_j} \right) \quad (3-7)$$

With the assumption that the product of infinitesimal strains is approximately zero the infinitesimal strain  $\varepsilon_{ij}$  is given by:

$$\varepsilon_{ij} = \frac{1}{2} \left( \frac{\partial u_i}{\partial X_j} + \frac{\partial u_j}{\partial X_i} \right) \quad (3-8)$$

The volume ratio  $J$  sometimes known as the Jacobian determinate, calculates the ratio of volume change between the reference and current configurations. This is calculated by the determinate of the deformation gradient:

$$J = \det(\mathbf{F}) \quad (3-9)$$

The deformation gradient can undergo polar decomposition into a unique orthogonal rotation tensor  $\mathbf{R}$ , the right (or material) stretch and left (or spatial) stretch tensors  $\mathbf{U}$  and  $\mathbf{V}$  respectively. This splits the deformation into a rotation and a stretch.

$$\mathbf{F} = \mathbf{RU} = \mathbf{VR} \quad (3-10)$$

These stretch tensors are related to the right and left Cauchy-Green tensors through the following relationships:

$$\begin{aligned} \mathbf{U}^2 &= \mathbf{C} \\ \mathbf{V}^2 &= \mathbf{B} \end{aligned} \quad (3-11)$$

The principal scalar invariants of the right Cauchy-Green tensor are useful in defining strain-energy density functions. Where  $\lambda_i$  is the stretch, and the three principal invariants are given by:

$$I_1 = \text{tr}(\mathbf{C}) = \lambda_1^2 + \lambda_2^2 + \lambda_3^2$$

$$I_2 = \frac{1}{2} [I_1^2 - \text{tr}(\mathbf{C}^2)] = \lambda_1^2 \lambda_2^2 + \lambda_1^2 \lambda_3^2 + \lambda_2^2 \lambda_3^2$$

$$I_3 = \det(\mathbf{C}) = J^2 = \lambda_1^2 \lambda_2^2 \lambda_3^2 \quad (3-12)$$

The velocity of a material point, P, on a body is:

$$\mathbf{v} = \frac{\partial \mathbf{x}}{\partial t} \quad (3-13)$$

The velocity between two points in the body is given as:

$$d\mathbf{v} = \frac{\partial \mathbf{v}}{\partial \mathbf{x}} d\mathbf{x} = \mathbf{L} d\mathbf{x} \quad (3-14)$$

and the spatial velocity gradient  $\mathbf{L}$  is:

$$\mathbf{L} = \frac{\partial \mathbf{v}}{\partial \mathbf{x}} = \frac{\partial \mathbf{v}}{\partial \mathbf{X}} \frac{\partial \mathbf{X}}{\partial \mathbf{x}} = \frac{\partial \mathbf{F}}{\partial t} \mathbf{F}^{-1} = \dot{\mathbf{F}} \mathbf{F}^{-1} \quad (3-15)$$

where  $\dot{\mathbf{F}}$  is the time derivative of the deformation gradient and  $\mathbf{F}^{-1}$  is the inverse of the deformation gradient. The spatial velocity gradient is decomposed into the symmetric part (sometimes known as the rate of deformation tensor) and the antisymmetric part (sometimes known as the spin tensor),  $\mathbf{D}$  and  $\mathbf{W}$  respectively.

$$\mathbf{D} = \frac{1}{2} (\mathbf{L} + \mathbf{L}^T)$$

$$\mathbf{W} = \frac{1}{2} (\mathbf{L} - \mathbf{L}^T) \quad (3-16)$$

Since the definition of  $\mathbf{D}$  is the rate of true strain ( $\mathbf{D} = \dot{\boldsymbol{\varepsilon}}$ ) this then implies you can derive the logarithmic strain  $\boldsymbol{\varepsilon}$  by the following expression (Abaqus Theory Manual, DS SIMULIA, USA).

$$\boldsymbol{\varepsilon}(t) = \int_0^t \mathbf{D} dt \quad (3-17)$$

### 3.1.3 Stress measures

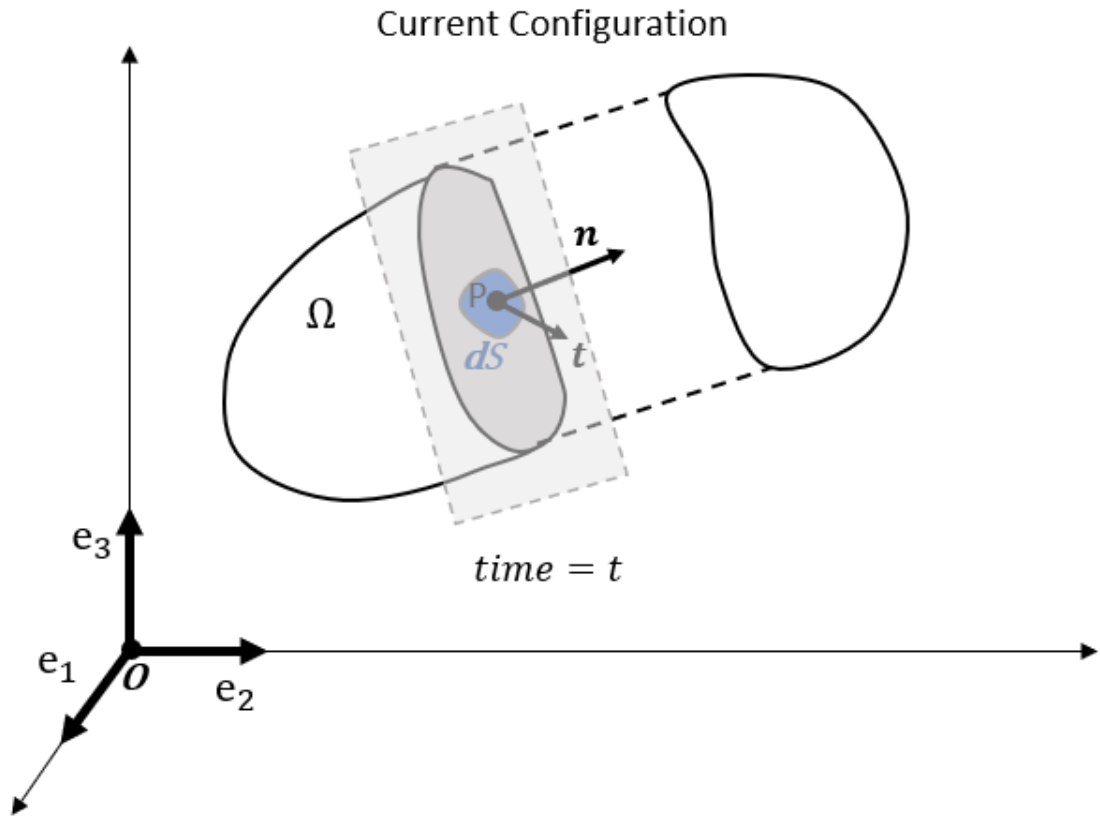


Figure 3.2. Traction vector acting on an infinitesimal surface  $dS$  and the traction vector,  $\mathbf{t}$ , acting on the surface with vector  $\mathbf{n}$ .

A representative schematic of a body with traction forces on a surface of a section cut is illustrated in Figure 3.2. The traction vector,  $\mathbf{t}$  is the force per unit that acts on the infinitesimal surface  $dS$  around the point,  $P$ . The vector  $\mathbf{n}$  acting normal to the surface.

The Cauchy (true) stress relates to the traction and normal vector by:

$$\mathbf{t} = \boldsymbol{\sigma} \mathbf{n} \quad (3-18)$$

The hydrostatic pressure stress component  $p$  of the stress of the Cauchy stress is described as:

$$p = -\frac{\text{tr}(\boldsymbol{\sigma})}{3} \quad (3-19)$$

The deviatoric stress  $\mathbf{s}$  can be expressed as:

$$\mathbf{s} = \boldsymbol{\sigma} - p\mathbf{I} \quad (3-20)$$

The Kirchoff stress tensor is defined as:

$$\boldsymbol{\tau} = J\boldsymbol{\sigma} \quad (3-21)$$

The first Piola-Kirchoff stress  $\mathbf{P}$  is given as:

$$\mathbf{P} = J\boldsymbol{\sigma}\mathbf{F}^{-T} \quad (3-22)$$

also giving the following expression for the Cauchy stress tensor:

$$\boldsymbol{\sigma} = J^{-1}\mathbf{P}\mathbf{F}^T \quad (3-23)$$

This then implies that:

$$\mathbf{P}\mathbf{F}^T = \mathbf{F}\mathbf{P}^T \quad (3-24)$$

The first Piola-Kirchoff stress  $\mathbf{P}$  is a non-symmetric tensor and is closely linked to the nominal stress by the relationship  $\mathbf{N} = \mathbf{P}^T$ . The second Piola-Kirchoff stress  $\mathbf{S}$  is a stress measure that is also related to  $\mathbf{P}$  but is symmetric and is used commonly in the formulation of constitutive equations of solids. It can be expressed in terms of the Cauchy stress and also the first Piola-Kirchoff stress by:

$$\mathbf{S} = J\mathbf{F}^{-1}\boldsymbol{\sigma}\mathbf{F}^{-T} = \mathbf{P}\mathbf{F}^T = \mathbf{F}\mathbf{P}^T \quad (3-25)$$

## 3.2 Constitutive laws

This section describes the constitutive laws implemented in computational models developed in future chapters in this thesis. The two constitutive law types used are hyperelasticity and viscoelasticity.

This section describes the hyperelastic and viscoelastic constitutive laws implemented in computational models developed in Chapters 4, 5 and 6. Many biological tissues are modelled using hyperelastic constitutive formulations. Hyperelastic materials are generally described in terms of the strain energy density functions denoted by  $\Psi$ . This the strain energy stored in the material per unit volume as a function of the stretch. The first Piola-Kirchoff stress can be described as:

$$\mathbf{P} = \frac{\partial \Psi(\mathbf{F})}{\partial \mathbf{F}} \quad (3-26)$$

The Cauchy stress is then described in terms of the deformation gradient and the right Cauchy-Green tensor by the following:

$$\boldsymbol{\sigma} = J^{-1} \mathbf{F} \left( \frac{\partial \Psi(\mathbf{F})}{\partial \mathbf{F}} \right)^T = 2J^{-1} \mathbf{F} \frac{\partial \Psi(\mathbf{C})}{\partial \mathbf{C}} \mathbf{F}^T \quad (3-27)$$

The second Piola-Kirchoff stress phrased in terms of the right Cauchy-Green tensor and the Lagrangian strain is:

$$\mathbf{S} = 2 \frac{\partial \Psi(\mathbf{C})}{\partial \mathbf{C}} = \frac{\partial \Psi(\mathbf{E})}{\partial \mathbf{E}} \quad (3-28)$$

Typically strain energy density functions are described using the strain invariants that were described in the equations from 3-11:

$$\Psi = \Psi[I_1, I_2, I_3] \quad (3-29)$$

Using the chain rule to differentiate the strain energy density function with respect to  $\mathbf{C}$  gives:

$$\frac{\partial \Psi(\mathbf{C})}{\partial \mathbf{C}} = \frac{\partial \Psi}{\partial I_1} \frac{\partial I_1}{\partial \mathbf{C}} + \frac{\partial \Psi}{\partial I_2} \frac{\partial I_2}{\partial \mathbf{C}} + \frac{\partial \Psi}{\partial I_3} \frac{\partial I_3}{\partial \mathbf{C}} \quad (3-30)$$

Then the derivatives of each of the invariants with respect to  $\mathbf{C}$  are:

$$\frac{\partial I_1}{\partial \mathbf{C}} = \mathbf{I}; \quad \frac{\partial I_2}{\partial \mathbf{C}} = I_1 \mathbf{I} - \mathbf{C}; \quad \frac{\partial I_3}{\partial \mathbf{C}} = I_3 \mathbf{C}^{-1} \quad (3-31)$$

Then this can be substituted back into 3-28 where the formulation of the second Piola-Kirchoff stress is established:

$$\mathbf{S} = 2 \left[ \left( \frac{\partial \Psi}{\partial I_1} + \frac{\partial \Psi}{\partial I_2} I_1 \right) \mathbf{I} - \frac{\partial \Psi}{\partial I_2} \mathbf{C} + I_3 \frac{\partial \Psi}{\partial I_3} \mathbf{C}^{-1} \right] \quad (3-32)$$

It can be deduced from the previous equation (3-27) that the Cauchy stress can be expressed in terms of the left Cauchy-Green tensor as follows:

$$\boldsymbol{\sigma} = 2J^{-1} \mathbf{B} \frac{\partial \Psi(\mathbf{B})}{\partial \mathbf{B}} \quad (3-33)$$

Using the same method to calculate the invariant derivatives in terms of  $\mathbf{C}$  but for now instead in terms of  $\mathbf{B}$ , and then substituting back into equation (3-33), a useful expression for the Cauchy stress in terms of the (symmetric) left Cauchy-Green tensor is obtained:

$$\boldsymbol{\sigma} = 2J^{-1} \left[ \left( \frac{\partial \Psi}{\partial I_2} I_2 + \frac{\partial \Psi}{\partial I_3} I_3 \right) \mathbf{I} + \frac{\partial \Psi}{\partial I_1} \mathbf{B} - I_3 \frac{\partial \Psi}{\partial I_2} \mathbf{B}^{-1} \right] \quad (3-34)$$

Compressibility in hyperelasticity can be solved numerically by the decomposition of the strain energy density function into a volumetric and an isochoric part:

$$\Psi = \Psi_{vol}(J) + \Psi_{iso}(\bar{\mathbf{B}}) \quad (3-35)$$

The volumetric part of the decomposed strain energy density function is dependent on the determinant of the deformation gradient (volume ratio)  $J$ . The isochoric strain energy part is a function of the distortional form of the left Cauchy-Green tensor which is expressed as:

$$\bar{\mathbf{B}} = J^{-\frac{2}{3}} \mathbf{B} \quad (3-36)$$

The Cauchy stress can be similarly be additively decomposed into volumetric and isochoric parts:

$$\boldsymbol{\sigma} = \boldsymbol{\sigma}_{vol} + \boldsymbol{\sigma}_{iso} \quad (3-37)$$

The volumetric and isochoric contribution expressions are determined as follows:

$$\begin{aligned} \boldsymbol{\sigma}_{vol} &= 2J^{-1} \mathbf{B} \frac{\partial \Psi_{vol}(J)}{\partial \mathbf{B}} = \frac{\partial \Psi_{vol}(J)}{\partial J} \mathbf{I} = p \mathbf{I} \\ \boldsymbol{\sigma}_{iso} &= 2J^{-1} \mathbf{B} \frac{\partial \Psi_{iso}(\bar{\mathbf{B}})}{\partial \mathbf{B}} = \bar{\boldsymbol{\sigma}} - \frac{tr(\bar{\boldsymbol{\sigma}})}{3} \mathbf{I} \end{aligned} \quad (3-38)$$

Where  $\bar{\boldsymbol{\sigma}}$  is defined by:

$$\bar{\boldsymbol{\sigma}} = 2J^{-1} \bar{\mathbf{B}} \frac{\partial \Psi_{iso}(\bar{\mathbf{B}})}{\partial \bar{\mathbf{B}}} \quad (3-39)$$

A wide range of hyperelastic formulations have been proposed for the modelling of large strain deformation of biological soft tissues, rubbers and polymers. The simplest formulation is referred to as the neo-Hookean hyperelastic constitutive law, with the strain energy density given as:

$$\Psi = C_{10}(\bar{I}_1 - 3) + \frac{1}{D_1}(J - 1)^2 \quad (3-40)$$

The two inputted parameters used to fit experimental data are  $C_{10}$  and  $D_1$ . This formulation uses modified invariants that are calculated using the deviatoric stretch defined as:

$$\bar{\lambda}_i = J^{-\frac{1}{3}} \lambda_i \quad (3-41)$$

for each of the three directions of stretch. In the neo-Hookean formulation only the first deviatoric strain tensor is required, which is expressed as:

$$\bar{I}_1 = \bar{\lambda}_1^2 + \bar{\lambda}_2^2 + \bar{\lambda}_3^2 \quad (3-42)$$

The initial shear modulus  $\mu_0$  and the initial bulk modulus are described by a relationship to the inputted parameters  $C_{10}$  and  $D_1$  respectively:



$$\mu_0 = 2C_{10}; \quad K_0 = \frac{2}{D_1} \quad (3-43)$$

The Yeoh hyperelastic model is the reduced polynomial with 3 independent terms and three corresponding pairs of parameters  $D_i$  and  $C_{i0}$  terms. The strain energy density function is given as:

$$\Psi = \sum_{i=1}^3 C_{i0} (\bar{I}_1 - 3)^i + \sum_{i=1}^3 \frac{1}{D_i} (J - 1)^{2i} \quad (3-44)$$

The Ogden strain energy density function is given as:

$$\Psi = \sum_{i=1}^N \frac{2\mu_i}{\alpha_i^2} (\bar{\lambda}_1^{\alpha_i} + \bar{\lambda}_2^{\alpha_i} + \bar{\lambda}_3^{\alpha_i} - 3) + \sum_{i=1}^N \frac{1}{D_i} (J - 1)^{2i} \quad (3-45)$$

where the material parameters are  $\alpha_i$ ,  $\mu_i$  and  $D_i$  are specified for each of the  $N$  terms.

Viscoelasticity describes a class of materials that exhibit both viscous and elastic characteristics when subjected to stress or strain. Such materials exhibit strain-rate dependence and hysteresis in loading curves during mechanical testing. Viscoelastic relaxation moduli are typically characterised using a Prony series. The shear relaxation modulus  $G_R(t)$  is given as:

$$\frac{G_R(t)}{G_0} = 1 - \sum_{i=1}^n g_i (1 - e^{-\frac{t}{\tau_i}}) \quad (3-46)$$

where  $G_0$  is the instantaneous shear modulus,  $g_i$  is the ratio of the long-term shear modulus  $G_R(\infty)$  to  $G_0$  for the  $i^{th}$  component in the Prony series and  $\tau_i$  is the relaxation time. A similar expression is used to describe the bulk relaxation modulus  $K_R(t)$ :

$$\frac{K_R(t)}{K_0} = 1 - \sum_{i=1}^n k_i (1 - e^{-\frac{t}{\tau_i}}) \quad (3-47)$$

where  $K_0$  is the instantaneous bulk modulus and  $k_i$  is the ratio of the long-term bulk modulus  $K_R(\infty)$  to  $K_0$  for the  $i^{th}$  component in the Prony series.

### 3.3 Finite element method

The computational analyses presented in this thesis is achieved using the finite element method (FE). All original FE analysis in upcoming chapters is carried out in the commercially available software package Abaqus (DS SIMULIA, RI, USA). The two numerical methods used to solve boundary value problems are an implicit integration scheme using Abaqus/Standard and an explicit integration scheme in Abaqus/Explicit. The fundamentals for FE and the two integration schemes will be outlined here and a more comprehensive discussion of these topics is available in the Abaqus User Documentation (DS SIMULIA, USA).

The FE method involves the discretisation of a volume into discrete volumes known as elements that are interconnected at points known as nodes. An iterative scheme is implemented over the entire domain and is solved in each of the smaller subdomains, i.e. at an element level. This facilitates an approximate solution to complex boundary problems as it easier to solve a series of simple polynomials than it is to solve one complex polynomial (Reddy.,2004).

#### 3.3.1 Implicit finite element method

The Abaqus/Standard implicit solver uses an iterative scheme to update stress and displacement in the elements of a body. The time increments in the models at time  $t$  are of a time step of  $\Delta t$  and so the time step that is being solved is  $t + \Delta t$ . Abaqus/Standard implements the Newton-Raphson method for the convergence of increments. This involves attempting to reduce the residual force vector reduce to within a specified tolerance. The principle of virtual work states that total work done by the internal and

external forces is zero for small strains. This is represented by the equation, in the FE method given in matrix/vector, or Voigt notation, as:

$$\int_V \delta \boldsymbol{\varepsilon}^T \boldsymbol{\sigma} dV = \int_S \delta \mathbf{u}^T \mathbf{t} dS \quad (3-48)$$

where  $V$  is the reference volume where equilibrium is forced,  $\boldsymbol{\varepsilon}$  is the strain,  $\boldsymbol{\sigma}$  is the stress vector  $S$  is the surface of the reference volume,  $\mathbf{u}$  is the displacement vector and  $\mathbf{t}$  is the traction vector. This relationship is active over every element (reference volume) in a numerical analysis. The change of displacement  $\delta \mathbf{u}$  and strain  $\delta \boldsymbol{\varepsilon}$  are calculated as:

$$\begin{aligned} \delta \mathbf{u} &= \widehat{\mathbf{N}}_e \delta \mathbf{u}_e \\ \delta \boldsymbol{\varepsilon} &= \widehat{\mathbf{B}}_e \delta \mathbf{u}_e \end{aligned} \quad (3-49)$$

where  $\widehat{\mathbf{N}}_e$  is the element shape function matrix and  $\widehat{\mathbf{B}}_e$  element shape function gradient matrix and  $\delta \mathbf{u}_e$  is the nodal displacement vector. Substituting these equations back into the principal of virtual work provides:

$$\sum_e \int_V \delta \mathbf{u}_e^T \widehat{\mathbf{B}}_e^T \boldsymbol{\sigma}(\mathbf{u}_e) dV = \sum_e \int_{S_e} \delta \mathbf{u}_e^T \widehat{\mathbf{N}}_e^T \mathbf{t} dS \quad (3-50)$$

Rearranging this expression:

$$\delta \mathbf{u}^T \left( \int_V \widehat{\mathbf{B}}^T \boldsymbol{\sigma}(\mathbf{u}) dV - \int_S \widehat{\mathbf{N}}^T \mathbf{t} dS \right) = 0 \quad (3-51)$$

Since  $\delta \mathbf{u}^T$  is arbitrary it may be eliminated from the expression:

$$\int_V \widehat{\mathbf{B}}^T \boldsymbol{\sigma}(\mathbf{u}) dV - \int_S \widehat{\mathbf{N}}^T \mathbf{t} dS = 0 \quad (3-52)$$

This expression can be viewed as the balance of forces in the simulation, so letting the difference of these equal a global residual force  $\mathbf{G}(\mathbf{u})$ .

$$\mathbf{G}(\mathbf{u}) = \int_V \hat{\mathbf{B}}^T \boldsymbol{\sigma}(\mathbf{u}) dV - \int_S \hat{\mathbf{N}}^T \mathbf{t} dS = \int_V \hat{\mathbf{B}}^T \boldsymbol{\sigma}(\mathbf{u}) dV - \mathbf{F}_{ext} \quad (3-53)$$

where  $\mathbf{F}_{ext}$  is the external force. The objective of the finite element method is to determine equilibrium whereby, an iterative scheme is implemented to vary  $\mathbf{u}$  to achieve:

$$\mathbf{G}(\mathbf{u}) = 0 \quad (3-54)$$

The iterative solving scheme implemented in Abaqus/Standard is the Newton-Raphson method. This method has the generic formulation of:

$$x_{n+1} = x_n - \frac{f(x_n)}{f'(x_n)} \quad (3-55)$$

This allows for an approximate solution from an initial guess to be subsequently iterated until convergence is reached. This is reached when the following expression is satisfied:

$$|x_{n+1} - x_n| < \text{tolerance} \quad (3-56)$$

In the case of finite element, the Newton-Raphson is applied for a step between times  $t$  and  $t + \Delta t$ . This method is particularly useful with non-linear constitutive laws and non-linear boundary condition analyses as it can achieve an accurate solution. An initial guess for the nodal displacements  $\mathbf{u}_n^{t+\Delta t}$  is made and convergence is then reached for the internal forces and externally applied loads/displacements using the Newton-Raphson method. This solving method for the displacement has the expression:

$$\mathbf{u}_{n+1}^{t+\Delta t} = \mathbf{u}_n^{t+\Delta t} - \left[ \frac{\partial \mathbf{G}(\mathbf{u}_n^{t+\Delta t})}{\partial \mathbf{u}} \right]^{-1} \mathbf{G}(\mathbf{u}_n^{t+\Delta t}) \quad (3-57)$$

This is the solution for the  $n^{th} + 1$  increment for the time  $t + \Delta t$ . This expression in terms of the change in the nodal displacement per increment takes the form of:

$$\delta \mathbf{u}_{n+1} = \mathbf{u}_{n+1}^{t+\Delta t} - \mathbf{u}_n^{t+\Delta t} = - \left[ \frac{\partial \mathbf{G}(\mathbf{u}_n^{t+\Delta t})}{\partial \mathbf{u}} \right]^{-1} \mathbf{G}(\mathbf{u}_n^{t+\Delta t}) \quad (3-58)$$

Considering that the element tangent stiffness matrix is  $\mathbf{K} = \frac{\partial \mathbf{G}(\mathbf{u})}{\partial \mathbf{u}}$ , the following relationship is used to iterate and solve for the time  $t + \Delta t$ :

$$\mathbf{K}(\mathbf{u}_n^{t+\Delta t}) \delta \mathbf{u}_{n+1} = - \mathbf{G}(\mathbf{u}_n^{t+\Delta t}) \quad (3-59)$$

The magnitude of  $\mathbf{G}(\mathbf{u}_n^{t+\Delta t})$  is checked against a tolerance to establish convergence. The element tangent stiffness matrix needs to be solved for in terms of displacement as non-linear solutions will require an incremental approach to solve for the change in stiffness with a change in displacement. The element tangent stiffness matrix is given as:

$$\mathbf{K}(\mathbf{u}) = \frac{\partial \mathbf{G}(\mathbf{u})}{\partial \mathbf{u}} = \frac{\partial}{\partial \mathbf{u}} \left( \int_V \mathbf{B}^T \boldsymbol{\sigma}(\mathbf{u}) dV - \mathbf{F}_{ext} \right) \quad (3-60)$$

which solves to:

$$\begin{aligned} &= \frac{\partial}{\partial \mathbf{u}} \left( \int_V \mathbf{B}^T \boldsymbol{\sigma}(\mathbf{u}) dV \right) \\ &\int_V \mathbf{B}^T \frac{\partial \boldsymbol{\sigma}(\mathbf{u})}{\partial \mathbf{u}} dV = \int_V \mathbf{B}^T \frac{\partial \boldsymbol{\sigma}(\mathbf{u})}{\partial \boldsymbol{\varepsilon}} \frac{\partial \boldsymbol{\varepsilon}}{\partial \mathbf{u}} dV \\ &\int_V \mathbf{B}^T \frac{\partial \boldsymbol{\sigma}(\mathbf{u})}{\partial \boldsymbol{\varepsilon}} \mathbf{B} dV = \int_V \mathbf{B}^T \mathbf{D}^{tan} \mathbf{B} dV \end{aligned} \quad (3-61)$$

$\mathbf{D}^{tan}$  is the consistent tangent matrix of the Jacobian constitutive law described by  $\frac{\partial \boldsymbol{\sigma}}{\partial \boldsymbol{\varepsilon}}$ .

The implicit solver requires to invert the stiffness matrix which is very computationally expensive. The advantage to this method is that large deformation is able to be taken in one step while retaining sufficient accuracy. This is dissimilar to the explicit finite element method solving in Abaqus/Explicit.

### 3.3.2 Explicit finite element method

The Abaqus/Explicit solver determines the solution without iterating by explicitly advancing the kinematic state from the previous increment. At the end of each time step the update of the system matrices is executed and the new system of equations is solved without iteration. If the increments are small enough accurate results will be computed, otherwise the solution will diverge. This is because equilibrium is not strictly enforced.

$$\mathbf{u}_{n+1} = \mathbf{u}_n + \Delta t^{n+1} \dot{\mathbf{u}}^{n+0.5}$$

$$\dot{\mathbf{u}}^{n+0.5} = \dot{\mathbf{u}}^{n-0.5} + \frac{\Delta t^{n+1} + \Delta t^n}{2} \ddot{\mathbf{u}}^n \quad (3-62)$$

where  $\dot{\mathbf{u}}$  and  $\ddot{\mathbf{u}}$  represent velocity and acceleration, and  $n$  is the time increment. Abaqus/Explicit inverts the mass matrix to reduce computational cost.

$$\ddot{\mathbf{u}}^n = \mathbf{M}^{-1} \cdot \left( \int_S \mathbf{N}^T \mathbf{t} dS + \int_V \mathbf{N}^T \mathbf{P}^n dV - \int_V \mathbf{B}^T \boldsymbol{\sigma}(\mathbf{u}) dV \right)$$

$$\ddot{\mathbf{u}}^n = \mathbf{M}^{-1} \cdot (\mathbf{F}^n - \mathbf{I}^n)$$

$$\mathbf{M} = \int_V \rho \mathbf{N} dV \quad (3-63)$$

where  $\mathbf{F}^n$  is the vector of applied external forces,  $\mathbf{M}$  is the diagonal mass matrix and  $\mathbf{I}^n$  is the vector of internal element forces.  $\mathbf{P}^n$  is the vector of nodal forces and  $\rho$  is the current density of the material. As the solution becomes unstable and divergent with a large time increment, it is important to ensure the  $\Delta t$  is small in the implicit scheme as there is no iterative process to impose equilibrium. The estimated stable time increment is given by:

$$\Delta t = \min \left( \frac{L_e}{c_d} \right) \quad (3-64)$$

Where  $L_e$  is the characteristic element length and  $c_d$  is the dilatational wave speed of the material. When performing a quasi-static analysis using the explicit integration scheme, it is important to ensure that the kinetic energy is less than 5% of the total strain energy

such that dynamic effects are negligible in the model. For further detail on the principles of the finite element method the reader is referred to Fagan (1992) and Bathe (2006).

### 3.4 Fracture Modelling

FE allows for numerical predictions of crack propagation and material damage. Fracture modelling entails the simulation of delamination or cracking in mechanical continuum simulations and is commonly used to predict the failure of materials under various loading conditions. In the study presented in Chapter 6 fracture modelling in atherosclerotic plaques is implemented using the cohesive zone modelling approach.

#### 3.4.1 Cohesive Zone Modelling (CZM)

The concept of the cohesive zone model (CZM) originated from Barenblatt (1959 & 1962) and Dugdale (1960). It allows for the approximation of non-linear fracture behaviour between two surfaces. A traction-separation law is applied at the interface that provides a representation of a cohesive zone in Figure 3.3.

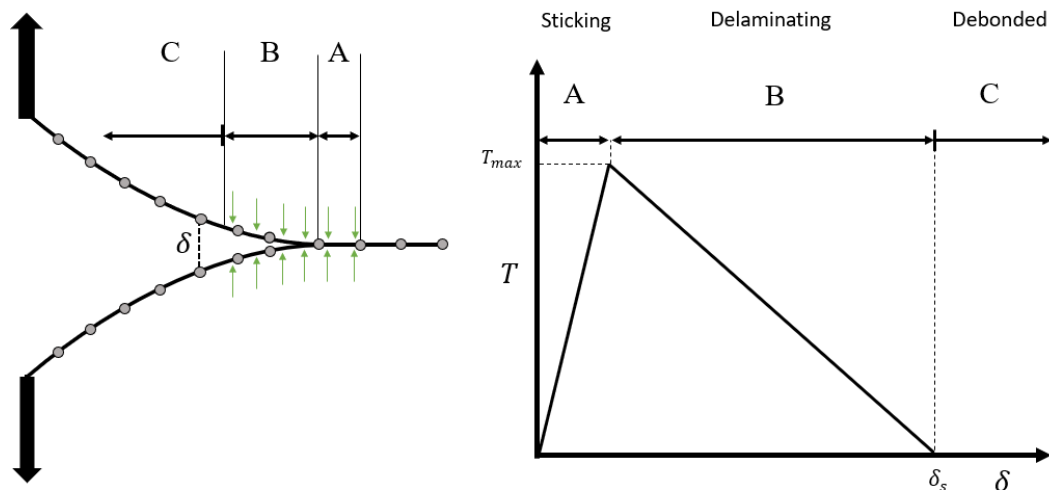


Figure 3.3. A representation of a bilinear cohesive model simulating the delamination of two surfaces. The cohesive forces are represented by the green arrows.

Every cohesive zone has a traction-separation law that defines the separation of surfaces and traction between the cohesive surfaces. The traction is a function of the separation of

the two surfaces. Figure 3.3 is an example of a bilinear traction-separation law in pure mode I (normal) separation or pure mode II (shear) separation. In the case of bilinear traction-separation, the traction can be split into three phases; A) elastic region with no softening and the stiffness, this region of the interface has typically a much greater stiffness than the material stiffness of the two materials at the interface, such that the effect on the macroscale behaviour is similar to a tied interface before damage is induced; B) after  $T_{max}$  has been reached, as the separation progresses the traction softens; C) after the maximum separation  $\delta_s$  the  $T = 0$  and the material has fully debonded. Cohesive laws may contain mode mixity to describe varying ratios of tangential and normal separation. The generic expression for the energy release rate  $G$  is:

$$G = \int_0^{\delta_s} T(\delta)d\delta \quad (3-65)$$

where  $T$  is the traction,  $\delta$  is the displacement and  $\delta_s$  is the maximum separation. A more comprehensive description of cohesive zones can be found in the Abaqus User Documentation (DS SIMULIA, USA), additionally a specific cohesive initiation and evolution is described in Chapter 6.



### 3.5 References

Barenblatt, G.I., 1962. The mathematical theory of equilibrium cracks in brittle fracture, in: *Advances in Applied Mechanics*. Elsevier, pp. 55–129.

Barenblatt, G.I., 1959. The formation of equilibrium cracks during brittle fracture. General ideas and hypotheses. Axially-symmetric cracks. *J. Appl. Math. Mech.* 23, 622–636.

Bathe, K.-J., 2006. *Finite element procedures*. Klaus-Jurgen Bathe.

Dugdale, D.S., 1960. Yielding of steel sheets containing slits. *J. Mech. Phys. Solids* 8, 100–104.

Fagan, M.J., 1992. *Finite Element Analysis: Theory and Practice*, Longman Scientific and Technical. Longman Scientific & Technical.

Reddy, J.N., 2013. *An introduction to continuum mechanics*. Cambridge university press.

Reddy, J.N., 2004. *An introduction to the finite element method*. McGraw-Hill New York, USA.

# 4 MATERIAL CHARACTERISATION AND IMAGING OF DISCRETE ILIOFEMORAL AND CAROTID ATHEROSCLEROTIC PLAQUE CONSTITUENTS

## 4.1 Introduction

Atherosclerosis is an insidious disease that progressively changes the mechanical properties and composition of the native arterial tissue and reduces the lumen area causing stenosis (Taniwaki et al., 2002). Major complications include claudication, ulceration and embolization (Shaikh et al., 2012). An improved understanding of the structure and mechanical behaviour of atherosclerotic plaque can potentially lead to improved vascular devices and minimization of adverse clinical events (Conway et al., 2017, 2014, 2012). Previous plaque studies observed that the length-scale of atherosclerotic calcified particles are comparable to those of the plaques themselves (Barrett et al., 2016; Cahalane et al., 2018). However, the majority of studies on the mechanical behaviour of

atherosclerotic plaques to date have focused on uniaxial testing of whole plaques (e.g. Salunke *et al.*,2001; Maher *et al.*,2009,2011; Lawlor *et al.*,2011; Mulvihill *et al.*,2013; Cunnane *et al.*,2015), rather than separate testing of the constituent components. The isolation and separate mechanical testing of calcified particles and fibrous tissue represents an advance on previous studies of plaque in which whole composite specimens were tested (e.g. Salunke *et al.*,2001; Maher *et al.*,2009,2011; Lawlor *et al.*,2011; Mulvihill *et al.*,2013; Barrett *et al.*,2015; Cunnane *et al.*,2015,2016). The studies of Maher *et al.* (2011), Teng *et al.* (2009) and Holzapfel *et al.* (2004) separated plaques, but neither calcified particles nor homogeneous fibrous tissue were isolated. Discrete computational models evaluating rupture risk of plaque constituents require, as input data for finite element modelling, separate mechanical properties for calcified particles and for the surrounding fibrous matrix material as suggested in Walsh *et al.* (2014). To the authors' knowledge, only two studies to date have investigated the mechanical properties of calcified particles using nano-indentation techniques (Cahalane *et al.*,2018; Ebenstein *et al.*,2009). Previous studies have used  $\mu$ CT analysis to quantify calcification content in atherosclerotic plaques (Barrett *et al.*,2016; Kelly-Arnold *et al.*,2013; Maldonado *et al.*,2015,2012). However, a characterization of the distribution of calcification morphologies within plaque samples has not been previously reported.

In the current study, a detailed characterisation of the morphology of calcified particles in atherosclerotic plaques is provided. While a wide distribution of particle size is observed, the largest particles in each plaque sample are found to be of a comparable length-scale to that of the plaque sample itself. Again, this suggests that mechanical analysis of plaque behaviour during angioplasty should explicitly represent calcified particles in addition to the surrounding fibrous matrix, requiring separate input of mechanical properties for both phases. The current study is structured as follows: Section

4.2.2 presents  $\mu$ CT analysis of plaque and calcified particle morphologies; Section 4.2.3 presents mechanical testing of isolated non-calcified fibrous tissue; Section 4.2.4 presents mechanical testing of isolated calcified particles

## 4.2 Methodology

### 4.2.1 Sample acquisition

Excised human atherosclerotic plaque samples are acquired from University College Hospital Galway and the Galway Clinic as approved by the respective hospital's ethical research committees; consent is acquired from patients scheduled for carotid or iliofemoral endarterectomies pre-operation and recorded anonymously in accordance to the Declaration of Helsinki. Samples are stored in vials of 0.1 M phosphate buffer solution (PBS) post-excision. Iliofemoral (n=8) and carotid (n=22) atherosclerotic plaques are collected throughout the study.

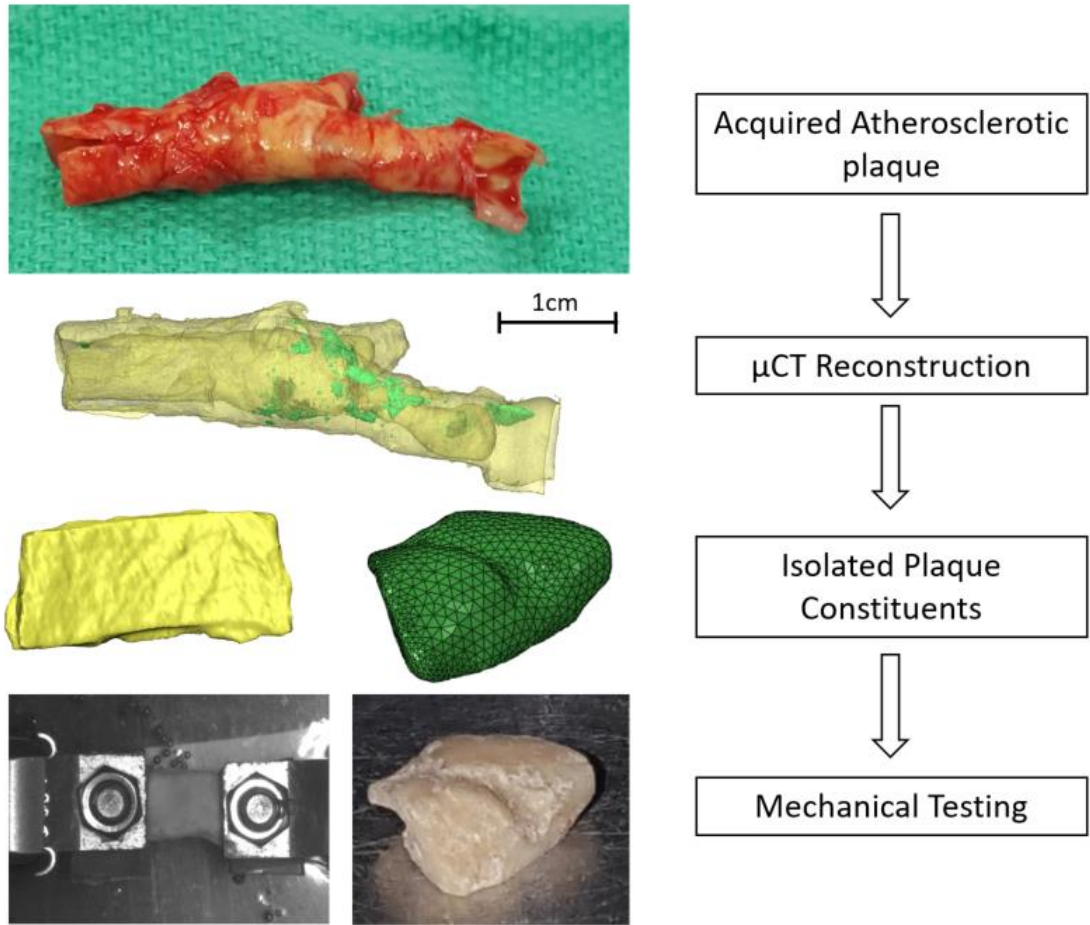


Figure 4.1. Schematic of the utilised testing pathway: Atherosclerotic plaque samples are acquired from endarterectomies, Imaging is used to ensure the homogeneity of isolated atherosclerotic plaque samples and isolated non-calcified fibrous samples are uniaxially tested in a water bath and isolated calcified particles undergo unconfined compression.

#### 4.2.2 Micro computed tomography analysis

As illustrated in Figure 4.1, samples are  $\mu$ CT scanned using intensity settings of 45 kV, 200  $\mu$ A and 9 W. An air filter is used with an integration time of 55 ms. A voxel size of 20  $\mu$ m is achieved allowing for sufficient resolution of the plaque constituents. Samples are submerged in mineral oil during scanning to create a sufficiently large density differential between the medium and the fibrous material. This allows for identification

of the outer boundary of the plaque. Scans are processed into 2D DICOM files for image analysis.

Image processing software (Mimics) is used to process the DICOM images and the constituents of the atherosclerotic samples are discretised using a greyscale value range of 4500-12000 for non-calcified fibrous tissue with grayscale values of 12000+ used for calcifications. The 3D files created using Mimics are further processed through 3-Matic 3D modelling software. STL models of composite plaques, consisting of fibrous tissue and embedded calcifications are then generated. A selection of 3D reconstructed composite plaque geometries are shown in Figure 4.2.

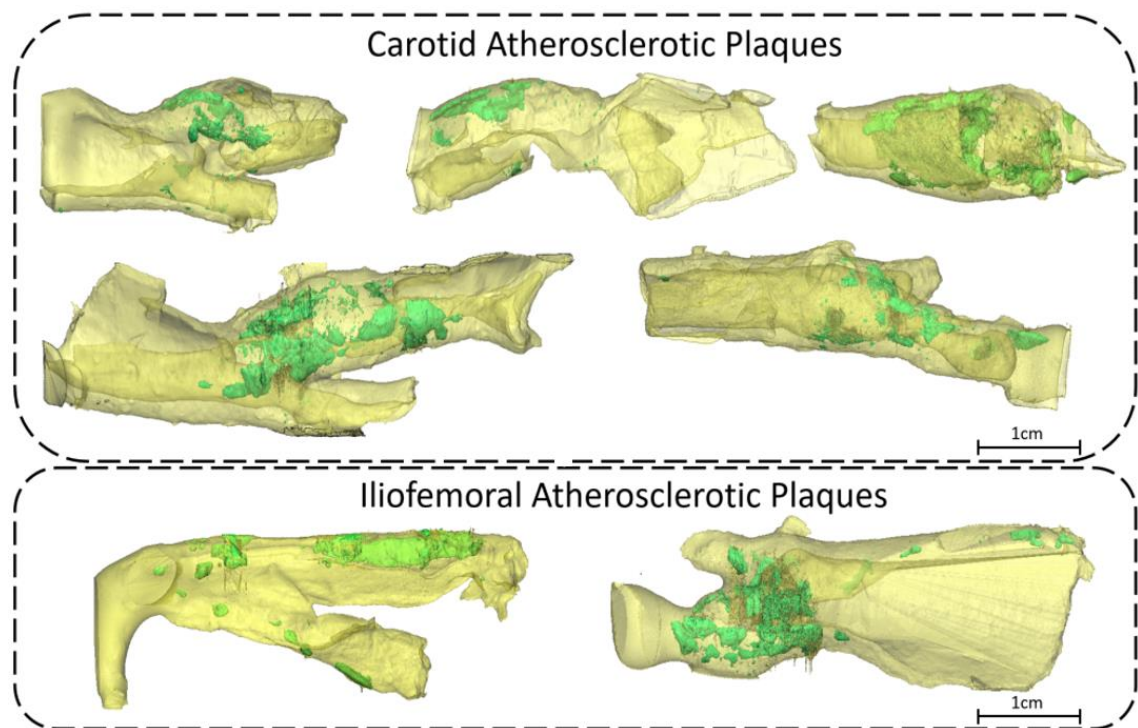


Figure 4.2. Reconstructed CT scans of whole atherosclerotic plaques showing both fibrous (yellow) and calcified constituents (green).

A MATLAB program was developed to analyse STL files so that the volume, surface area and sphericity can be quantified for each individual calcified particle within each

plaque. Additionally, the total volume of each plaque is quantified. The volume of each entity is calculated using the Gauss divergence theorem. The surface area is calculated by summing the areas of the individual faces of the triangles that bound each discretised volume.

For each calcified plaque the following quantitative metrics are determined:

*Total Calcification Volume Fraction*

$$= \frac{\text{Total volume of calcified particles in plaque}}{\text{Total volume of plaque}} \quad (4-1)$$

*Particle Volume Fraction*

$$= \frac{\text{Volume of the individual calcified particles}}{\text{Total volume of calcified particles in plaque}} \quad (4-2)$$

*Sphericity*

$$= \frac{\text{Surface area of equivalent volume sphere}}{\text{Surface area of calcified particle}} \quad (4-3)$$

Sphericity provides an approximate measure of how similar the shape of the individual calcified particle is to a sphere, with a max value of 1 being a perfect sphere (Liu et al., 2008). This is a useful measure to assess the geometric variation between calcified particles.

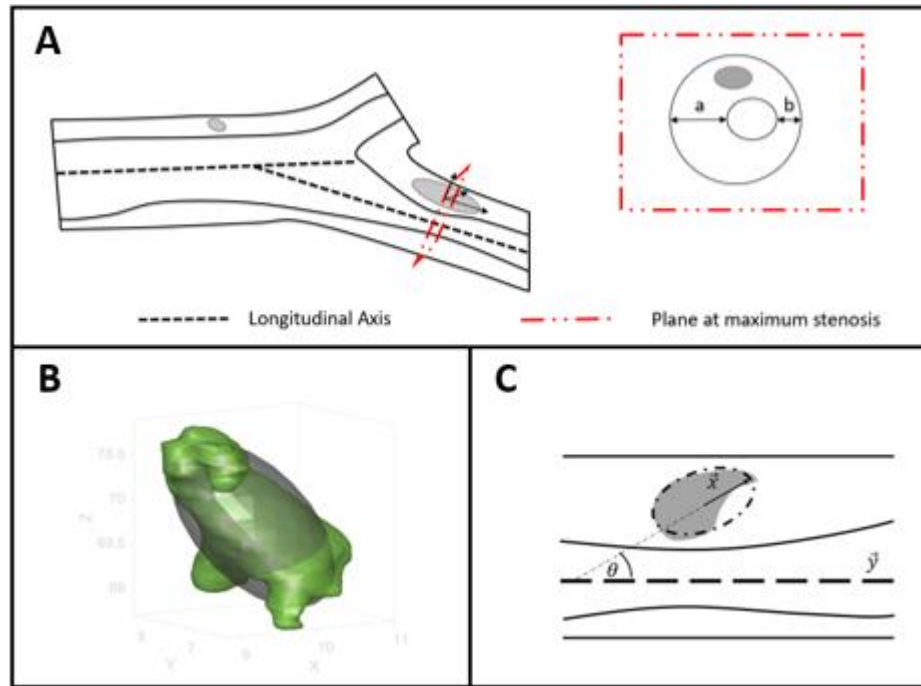


Figure 4.3. (A) Schematic of the methodology used to characterise the maximum eccentricity  $\left(\frac{a}{b}\right)$  of a plaque and the orientation of the major axis of embedded calcifications in relation to the centreline of the plaque. (B) Best-fit ellipsoid for a  $\mu$ CT reconstruction of a calcification. (C) Illustration of the angle  $\theta$  between the major axis of the best fit ellipsoid and the longitudinal axis of the vessel.

As shown in Figure 4.3(A) eccentricity of the plaque is characterised for the atherosclerotic plaques scanned. A plane at the maximum stenosis along the plaque sample is isolated. Then the largest ( $a$ ) and smallest ( $b$ ) thickness of the plaque are measured. The eccentricity is then calculated as  $\left(\frac{a}{b}\right)$ . This measure of eccentricity was previously used in Li et al. (2010).

Ellipsoids are fitted to the calcifications using a MATLAB toolbox from M Moerman (2018), as shown in Figure 4.3(B) and a vector describing the orientation of the major axis is computed. Figure 4.3(C) shows the directionality of the centreline of each of the plaques being approximated by identifying a series of centre points along the vessel



lumen. The angle  $\theta$  between the major axis of the best-fit ellipsoid for a calcified particle ( $\vec{x}$ ) and the corresponding vessel longitudinal axis ( $\vec{y}$ ) is computed as;

$$\theta = \cos^{-1} \left[ \frac{\vec{x} \cdot \vec{y}}{|\vec{x}| |\vec{y}|} \right] \quad (4-4)$$

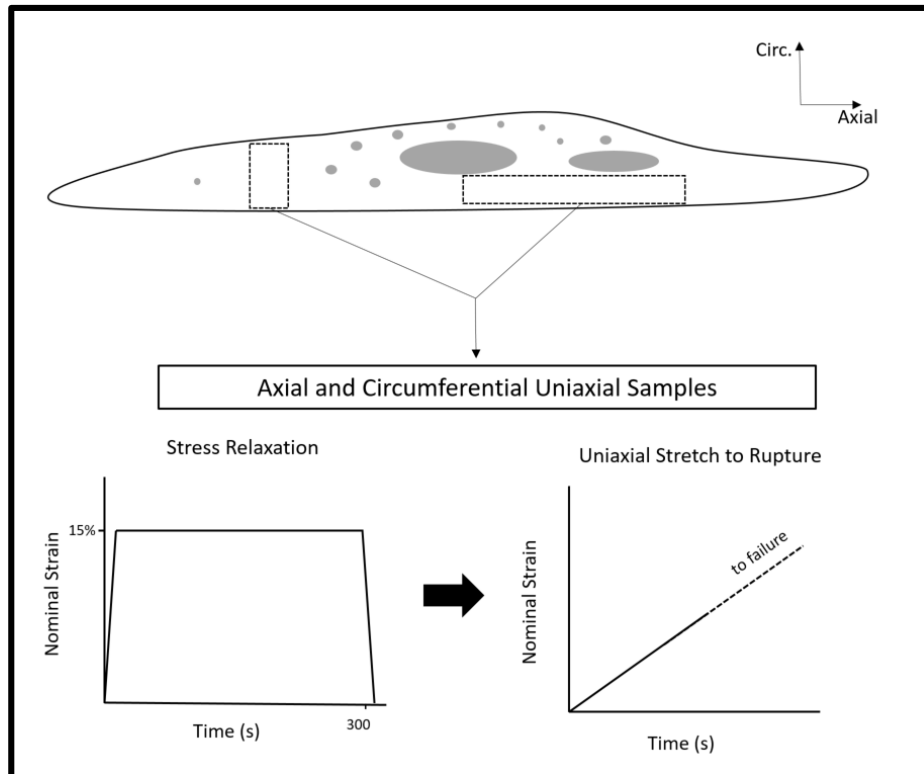


Figure 4.4. Schematic of the extraction and testing of isolated non-calcified fibrous samples that do not contain any detectable (by  $\mu$ CT analysis) calcified particles. Strips of fibrous tissue are cut from atherosclerotic tissue oriented either axially or circumferentially. These strips are stretched to 15% strain and held for 300 seconds and uniaxially tested to failure.

#### 4.2.3 Fibrous tissue uniaxial mechanical testing

Non-calcified fibrous samples are isolated from the acquired atherosclerotic plaques, as shown in Figure 4.4, focusing on sites that exhibit no identifiable (through  $\mu$ CT scanning)

calcified particles. Samples are extracted so that the long axis is aligned (approximately 15 mm x 5 mm) in either the circumferential or axial direction. These samples are subject to stress relaxation testing and constant strain-rate uniaxial tension testing. Excised fibrous tissue strips are then re-scanned to confirm that no calcifications are present. Samples are tested in a water bath at room temperature. Samples are glued to sandpaper in the clamped region, and are then rigidly clamped using hand-tightened knurled metal clamps.

A preload of 0.05 N is placed on the samples to remove kinking. Stress relaxation testing is performed whereby samples are stretched to 15% nominal strain in 2 seconds and then held at 15% nominal strain for 5 minutes while the change in reaction force is measured as a function of time. Constant strain-rate uniaxial tension tests are carried out on the samples at a strain-rate of 7.5% strain per minute until rupture or slippage is observed. This strain-rate is chosen in order to observe the long-term stiffness in the test samples, allowing for a comprehensive description of the tissue when used in conjunction with stress-relaxation data to describe the time-dependent behaviour.

Visco-hyperelastic material constitutive laws are fit to the experimental data. Specifically, a Yeoh hyperelastic model (Yeoh, 1993) is used to capture strain stiffening behaviour, where the strain energy density,  $W$  is given as:

$$W = \sum_{i=1}^3 C_{i0} (\bar{I}_1 - 3)^i + \sum_{i=1}^3 \frac{1}{D_i} (J - 1)^{2i} \quad (4-5)$$

The long-term parameters  $C_{i0}$  describe the non-linear shear stiffness, while the parameters  $D_i$  describe the material compressibility.  $\bar{I}_1$  is based on the isochoric first strain invariant and  $J$  is the volume Jacobian.

Fitted hyperelastic parameters are used in conjunction with a Prony series to describe the rate-dependant viscoelastic material behaviour; the shear relaxation modulus  $G_R(t)$  is given as

$$\frac{G_R(t)}{G_0} = 1 - \sum_{i=1}^n g_i (1 - e^{-\frac{t}{\tau_i}}) \quad (4-6)$$

where  $G_0$  is the instantaneous shear modulus,  $n$  is the number of the terms in the Prony series,  $\tau_i$  are the relaxation time constants for each term of the series, and the parameters  $g_i$  set the ratio of long-term to instantaneous shear modulus for each term. In the optimisation process the  $\tau_i$  and  $g_i$  parameters were incremented to optimise inverse finite element solution. The root mean square (RMS) error is calculated between the computational stress-strain results and the experimental stress-strain results. The RMS error is then normalised with respect to the maximum stress. In order to inspect if the solution is unique, multiple different starting parameter sets are chosen to test convergence on the same solution.

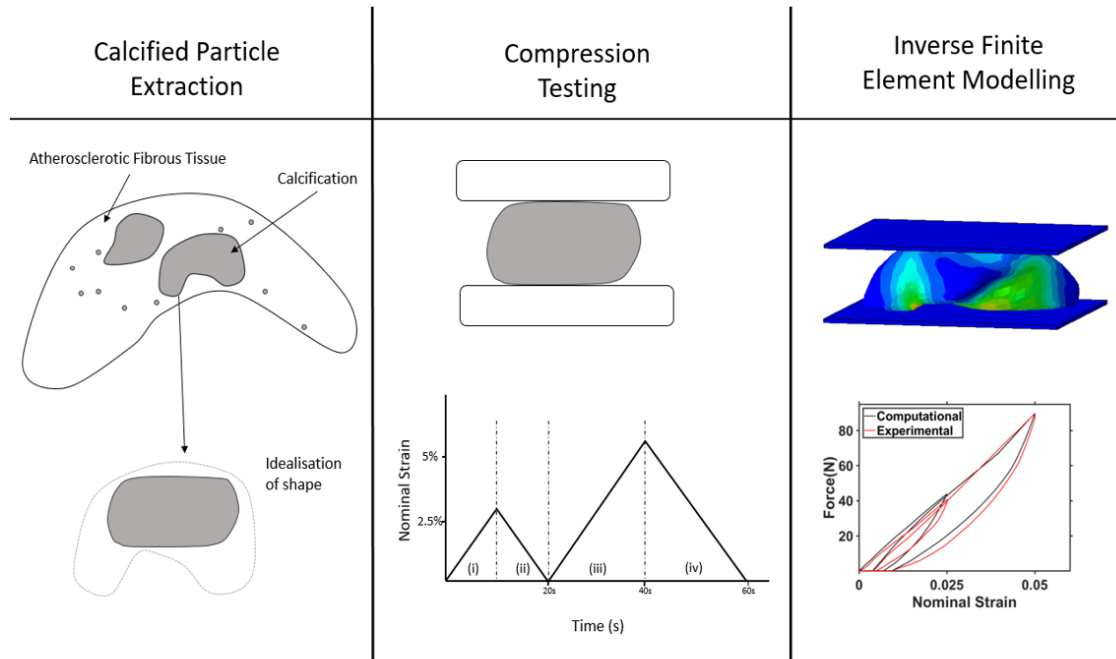


Figure 4.5. Schematic of the calcification testing: Calcified particles are extracted from the plaque and the sides are flattened using grit paper; the sample then undergoes unconfined compression, applied in steps, and finally, inverse finite element methods are used to characterise the mechanical behaviour of the tested isolated calcified particles.

#### 4.2.4 Isolated calcified particle compression testing and inverse finite element analysis

As illustrated in Figure 4.5, calcified particles ( $n=6$ ) are extracted from the atherosclerotic plaques and then polished to provide flat upper and lower surfaces for parallel plate compression testing. Samples are  $\mu$ CT scanned before testing to generate 3D finite element models for inverse finite element simulation of compression tests and material parameter calibration. The following loading protocols are applied: (i) loading to applied nominal axial strain of -2.5% nominal strain (negative sign indicates a compressive strain); (ii) unloading to a nominal strain of 0%; (iii) reloading to a nominal strain of -5%; (iv) unloading to a nominal strain of 0%. In all cases a strain-rate magnitude of 5% nominal strain per minute is applied. Inverse finite element simulations are carried out to determine the material behaviour of the individual isolated calcified particles. Loading

platens are modelled as rigid surfaces. Frictionless contact is assumed between the calcification and the loading platens. An iterative scheme is applied to identify the constitutive law and material parameters that accurately reproduce the experimentally measured force-deflection relationship for each calcified particle. The root mean square (RMS) error is calculated between the computational stress-strain results and the experimental stress-strain results. The RMS error is normalised with respect to the maximum force.

#### 4.2.5 Scanning electron microscopy

SEM imaging of both composite plaque samples and isolated calcified particles is performed. In order to gain insight into the internal structures, prior to imaging the composite plaque is ruptured through the application of uniaxial stretching, and then the fracture surface analysed. Similarly, fracture surfaces are created in isolated calcified particles through the application of parallel plate compression to the point of failure. Following the generation of fracture surfaces, samples are submerged in 2.5% glutaraldehyde for 2 hours at room temperature in order to fix the samples. They are then submerged in using 0.1 M PBS solution for 5 minutes then rinsed with more PBS solution. They are then dehydrated using increasing concentrations of ethanol (50%, 75% and 80%) for 5 minutes each at 4°C. Samples are then rinsed with 90% ethanol then 100% ethanol, twice each. They are then covered with hexamethyldisilazane (HMDS), and the solution allowed to evaporate off completely, thereby fully dehydrating the samples. Samples are then gold-plated to ensure a conductive surface for high-quality imaging capabilities.

## 4.3 Results

### 4.3.1 Micro computed tomography analysis

Data is shown for all identifiable particles in iliofemoral (n=7) and carotid (n=20) plaques; 1 femoral and 2 carotid plaques had compromised scans. The resolution of the  $\mu$ CT scans had a voxel size of 20  $\mu\text{m}$ , particles of volume less than  $0.0001 \text{ mm}^3$  could not be reliably identified or characterised. As shown in Figure 4.6(A), the total volume of individual excised iliofemoral plaques ( $2922 \pm 1733.3 \text{ mm}^3$ ) is significantly higher than that of carotid plaques ( $1601 \pm 738.1 \text{ mm}^3$ ). As shown in Figure 4.6(B), calcified particles make up  $7.6 \pm 9.4\%$  of the total volume of carotid plaques, compared to  $19.1 \pm 16.5\%$  of the total volume of iliofemoral plaques. However, Figure 4.6(C) shows the largest calcified particle in a plaque makes up  $53.7 \pm 18.5\%$  of the total calcification volume with  $88.4 \pm 11.6\%$  of the total calcification volume made up by the three largest calcifications. The probability distribution of calcified particle volume across all plaques is shown in Figure 4.6(D). Calcified particles smaller than  $0.25 \text{ mm}^3$  are significantly more numerous than larger particles. Sphericity of calcified particles (eqn. 4-3) is plotted as a function of particle size in Figure 4.6(E). Sphericity tends to increase as the volume of calcified particles decreases, i.e. smaller particles tend to be more spherical. As an example, for carotid plaques, calcified particles with a volume between  $0.025$  and  $0.05 \text{ mm}^3$  have a sphericity of  $0.768 \pm 0.09$ , whereas particles with a volume greater than  $10 \text{ mm}^3$  have a sphericity of  $0.339 \pm 0.082$ .

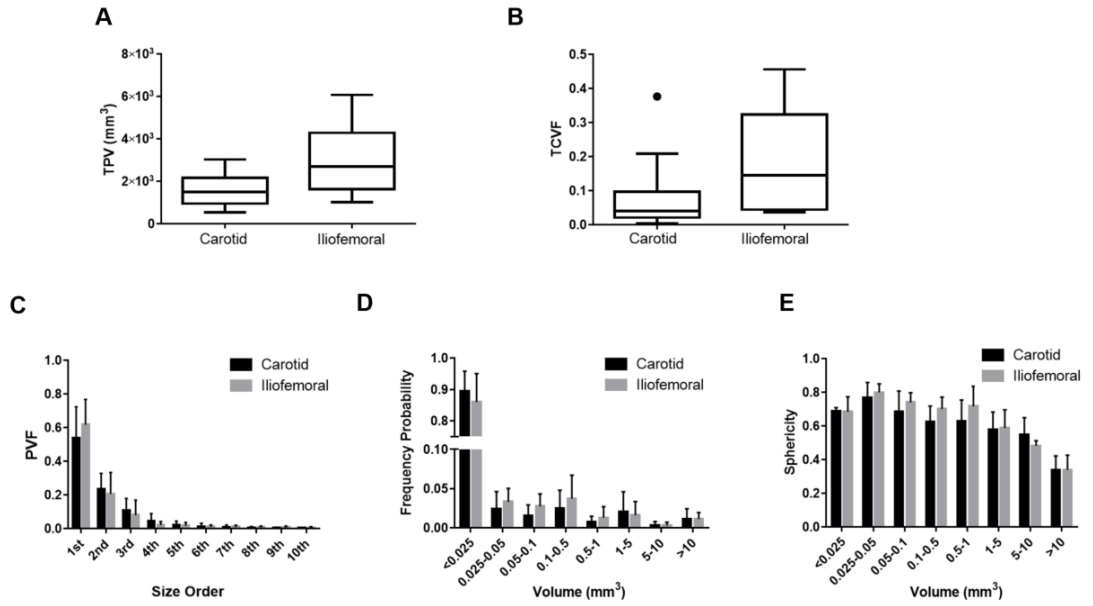


Figure 4.6. Tukey boxplots (A & B) are shown for the Total Plaque Volume (TPV) for both carotid (n=20) and iliofemoral samples (n=7) and Total Calcification Volume Percentage (TCVF, eqn. 4-1). Bar charts of mean and SD of: (C) Particle Volume Fraction (PVF, eqn. 4-2) of the 10 largest calcifications in each scanned plaque; (D) Frequency probability of calcifications of differing volumes; (E) Sphericity versus Volume of calcifications in excised plaque samples.

Table 4.1 Analysis of the orientation  $\theta$  of the largest six calcified particles in each plaque (N=23). Three categories of particle alignment are considered:  $0^\circ < \theta \leq 30^\circ$ ;  $30^\circ < \theta \leq 60^\circ$ ;  $60^\circ < \theta \leq 90^\circ$ . The number fraction (%) of largest particles (1<sup>st</sup>) across plaque samples (N=23) in each category is presented. Similar data is presented for the 2<sup>nd</sup>, 3<sup>rd</sup>, 4<sup>th</sup>, 5<sup>th</sup>, and 6<sup>th</sup> largest particles across all plaques.

Angle $\theta$ between centreline & calcification major axis	Calcified Particle Size Order					
	1st	2nd	3rd	4th	5th	6th
$0^\circ < \theta \leq 30^\circ$	47.8%	26.1%	43.5%	30.4%	8.7%	17.4%
$30^\circ < \theta \leq 60^\circ$	34.8%	39.1%	26.1%	34.8%	34.8%	56.5%
$60^\circ < \theta \leq 90^\circ$	17.4%	34.8%	30.4%	34.8%	56.5%	26.1%

As presented in Table 4.1, the largest calcifications in a plaque tend (47.8% of cases) to be aligned close to the longitudinal axis ( $0^\circ < \theta \leq 30^\circ$ ). In contrast, alignment close to the circumferential direction ( $60^\circ < \theta \leq 90^\circ$ ) is observed in only 17.4% of cases. With reducing size order of the particle, the tendency towards longitudinal alignment is reduced. In the case of the 6<sup>th</sup> Particle Size Order, only 17.4% of particles are observed to align between  $0^\circ < \theta \leq 30^\circ$ . Analysis of the  $\mu$ CT data reveals that eccentricity measures  $5.33 \pm 3.98$  across the plaques with intact plaque lumens (n=14).

#### 4.3.2 Fibrous uniaxial testing results

Results of mechanical tests performed on the isolated non-calcified fibrous samples are shown in Figure 4.7. The isolated non-calcified fibrous samples from both carotid and iliofemoral plaques exhibit significant stress relaxation (Figure 4.7(A)). The average



nominal stress reduced by approximately 38% in 5 minutes for carotid samples and by 50% for iliofemoral samples. This result demonstrates that the plaque fibrous matrix is viscoelastic. Uniaxial tensile testing of the isolated non-calcified fibrous samples demonstrates highly non-linear material behaviour (Figure 4.7(B,C)). A similar stiffness is observed for iliofemoral and carotid plaques for applied tensile strains up to 8%. However, at higher strains significantly higher strain stiffening is observed for carotid plaques. No significant difference ( $P>0.05$ ) is observed between the mechanical behaviour of circumferentially oriented samples and axially oriented samples in either carotid or iliofemoral plaques. Figure 4.7(C) demonstrates that iliofemoral plaques are statistically significantly stiffer than carotid plaques at higher strains.

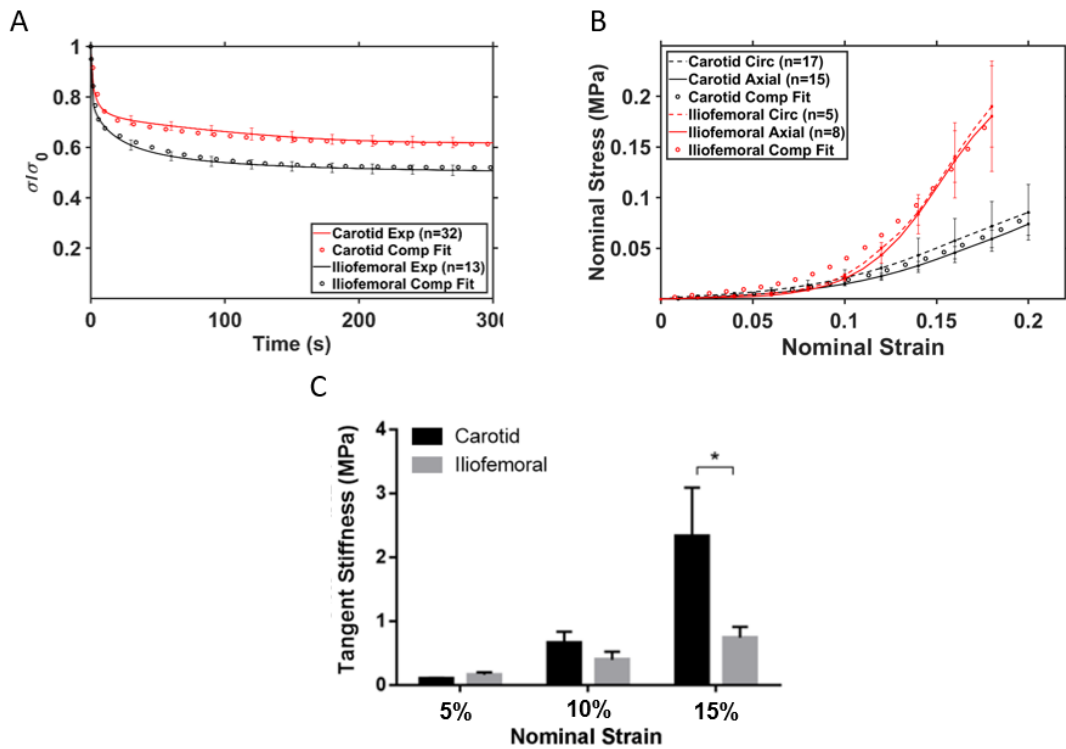


Figure 4.7. (A) Stress relaxation of isolated non-calcified carotid and iliofemoral fibrous plaque samples;  $\sigma_0$  is the maximum nominal stress following the initial loading to a strain of 15%. (B) Nominal stress-strain relationship for isolated non-calcified carotid and iliofemoral fibrous plaque samples in the circumferential and the axial directions. (C)

Mean tangent stiffnesses of the isolated non-calcified carotid and iliofemoral fibrous plaque samples at 5%, 10% and 15% nominal strains and one tail of the standard error of the mean (\* $p < 0.05$  using a one-way analysis of variance test).

Figure 4.7(A) and Figure 4.7(B) demonstrate that the hyper-viscoelastic material model described in Section 2.3 provides a reasonably accurate description of the stress-relaxation and uniaxial tensile test results for carotid (normalised RMS error: 0.012 (Figure 4.7(A)) & 0.123 (Figure 4.7(B))) and iliofemoral (normalised RMS error: 0.0117 (Figure 4.7(A)) & 0.056 (Figure 4.7(B))) plaque fibrous matrix samples. Best-fit material parameters are presented in Table 4.2.

Table 4.2. Fitted parameters for the stress-relaxation and uniaxial testing.

	$C_{10}$ (MPa)	$C_{20}$ (MPa)	$C_{30}$ (MPa)	D	$g_1$	$\tau_1$ (s)	$g_2$	$\tau_2$ (s)
Carotid	0.0091	0.374	4.608	12.802	0.298	4.51	0.116	87.06
Iliofemoral	0.0264	0.009	22.695	4.161	0.341	2.33	0.176	54.1

#### 4.3.3 Calcification compression testing and inverse finite element analysis

The measured dimensions of the tested calcified particles and the respective volume of their reconstructions are listed in Table 4.3. Figure 4.8 shows the strain distribution of the inverse finite element models of the isolated calcified particles that are created from  $\mu$ CT scans of the calcifications. Computed results demonstrate a highly heterogeneous distribution of strain due to the complex geometry of each isolated calcified particle. This highlights the necessity of inverse finite element analysis for the interpretation of experimentally measured forces and identification and calibration of material laws. Rupture data of tested fibrous homogeneous plaque is describe in Appendix 4B.

Table 4.3. Maximum height, width, thickness, and volume of the tested calcified particles measured from the reconstructed  $\mu$ CT imaging.

	Max Height (mm)	Max Width (mm)	Max Thickness (mm)	Volume (mm <sup>3</sup> )
I	2.32	4.09	3.25	26.5
II	2.86	4.22	4.82	55.3
III	2.50	5.99	4.45	48.8
IV	1.64	4.35	3.97	26.6
V	2.46	5.15	3.68	34
VI	2.87	5.15	3.29	26.8

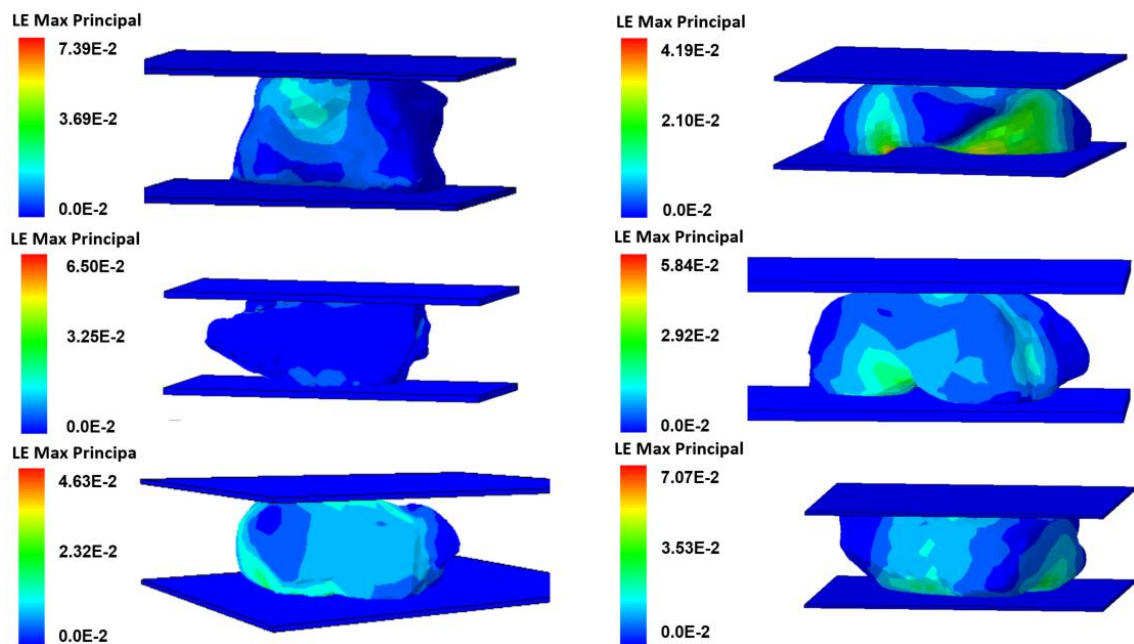


Figure 4.8. Contour plots highlighting maximum principal strain distribution whilst compressed at a nominal strain of 5% for the inverse finite element models of the 6 unconfined compression calcification samples.

The force-strain curves for the experimental testing of isolated calcified particles are shown in Figure 4.9. All samples exhibit large hysteresis between loading and unloading curves, both for initial compression to 2.5% and subsequent compression to 5% nominal

compressive strain, suggesting that the material is viscoelastic. Following the second unloading half-cycle, zero force is measured at approximately ~1% strain for all samples (i.e. the platen lost contact with the calcified particle at a strain of ~1%). However, all samples are observed to have recovered their initial undeformed height within 15 minutes of the completion of the test, again suggesting that the material behaviour is viscoelastic in nature, and further suggesting that significant damage or plasticity are not induced by the applied loading. Modelling the calcified particle as a viscoelastic material provides a reasonable prediction (NRMS Error <0.1) of the experimental behaviour, both for the initial loading cycle to 2.5% strain, and the subsequent loading cycle to 5% strain, as also shown in Figure 4.9.

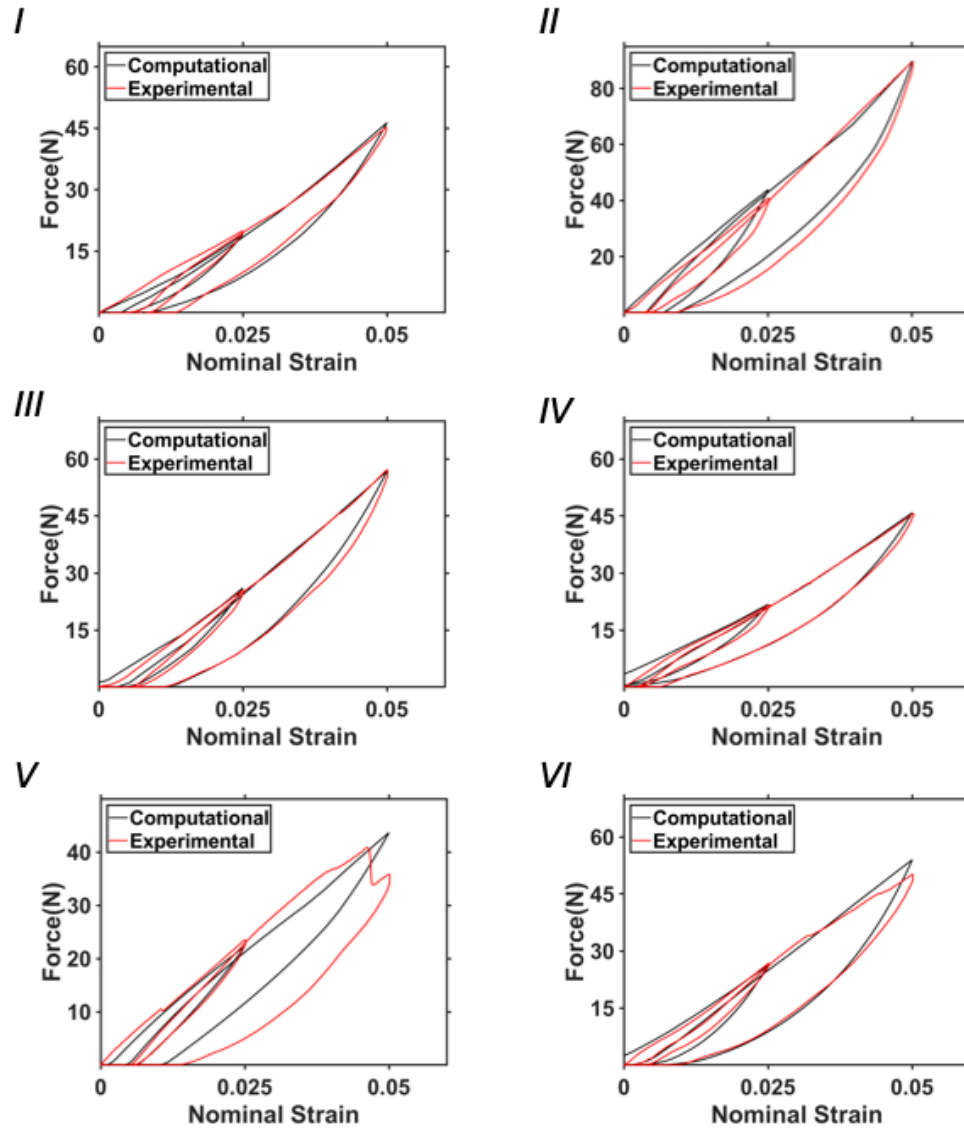


Figure 4.9. Force-displacement experimental curves and the computational fit for the ramp compression of isolated calcified particles.

The fitted parameters and normalised RMS of the inverse finite element simulations are listed in Table 4.4 for each of the isolated calcified particles. In all cases a neo-Hookean (Pence and Gou, 2015) hyperelastic model is applied and the effective Poisson's ratio is fixed at 0.4 based on the range of reported for Poisson's ratio of cortical bone which has been shown to vary between 0.15-0.45 (Wirtz *et al.*, 2000). In all cases a one-term Prony series provides a reasonable fit (NRMS Error < 0.1). The mean $\pm$ SD across all samples

are given as follows: instantaneous Young's modulus =  $424.4 \pm 163.3$  MPa, long-term Young's modulus =  $203.5 \pm 80.9$  MPa, and relaxation time =  $7.5 \pm 1.76$  s.

Table 4.4. Viscoelastic material parameters determined by inverse finite element analysis of compression experiments for each isolated calcified particle (I-VI). A one-term Prony series is found to provide a reasonable fit in all cases. Calibrated values for instantaneous Young's modulus  $E_0$ , long-term Young's modulus,  $E_\infty$ , relaxation time,  $\tau$ , and normalised RMS error for the fit are presented for each sample.

	$E_0$ (MPa)	$E_\infty$ (MPa)	$\tau$ (s)	Norm. RMS Error
I	574.9	287.5	7	0.0231
II	616	264.8	5	0.0296
III	365.9	164.6	10	0.0221
IV	366.8	183.4	7	0.0187
V	455.5	250.5	9	0.0998
VI	167.1	70.2	7	0.0314

#### 4.3.4 Scanning electron microscopy

SEM imaging of a ruptured composite carotid plaque sample is shown in Figure 4.10(A). A fracture surface is generated along the matrix-calcification interface. This fracture surface exhibits an irregular morphology with evidence of fibre pull-out from the calcification. In contrast, an intact non-ruptured surface exhibits regular patterns of aligned fibres. SEM imaging of fractured isolated carotid calcified particles are presented

in Figure 4.10(B-D). Significant fibre content is evident at the fracture surfaces, with fibrillation/fibre pull-out. This suggests that the presence of fibres is not limited to the surface of the calcified particle, but that fibres may be embedded throughout the particle.

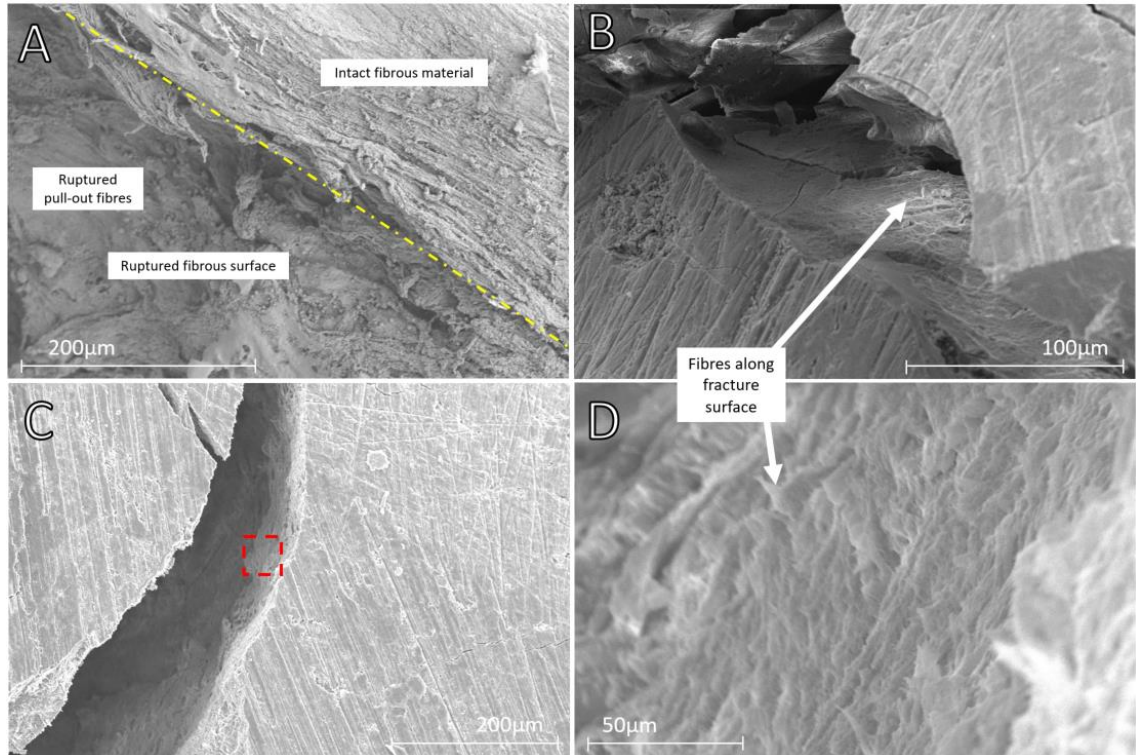


Figure 4.10. SEM images of samples showing various aspects of plaque constituent topology: (A) ruptured and intact surface of fibrous matrix; (B) Fracture surface of calcified particle showing fibres at surface; (C) Fracture surface in isolated calcified particle with the indicated area (D) demonstrating fibres at the fracture surface.

#### 4.4 Discussion

This study presents a novel morphological and mechanical characterization of the calcified particles in femoral and carotid atherosclerotic plaques.  $\mu$ CT scanning provides detailed characterization of the distribution in size and shape of calcified particles. Calcified particles contribute a significant proportion of the average plaque volume (7.6% carotid; 19.1% femoral), and on average over 50% of this volume ( $53.7 \pm 18.6\%$  carotid;  $61.7 \pm 15\%$  femoral) is accounted for by the largest individual particle found in the plaque.

Therefore, the morphological characterization suggests that calcified plaques should be modelled as composite materials with explicit representation of large calcifications. Based on this finding, mechanical testing of isolated calcified particles is performed, in addition to mechanical testing of isolated non-calcified fibrous matrix material. While both materials are found to exhibit viscoelastic behaviour, the stiffness of isolated calcified particles is found to be approximately two orders of magnitude higher than that of the isolated non-calcified fibrous matrix.

In addition to the key finding that the majority of the total volume of calcification in an atherosclerotic plaque is composed of the largest individual calcified particle, also observed is that larger calcified particles are less spherical (lower sphericity) than smaller calcified particles. Previous studies suggest that as calcifications grow they start to coalesce with other calcifications nearby (Abedin et al., 2004; Stary, 2002), developing a more irregular less spherical morphology. The observation of a high number of small calcified particles ( $<0.025 \text{ mm}^3$ ) is consistent with previous studies ((Kelly-Arnold et al., 2013; Maldonado et al., 2012; Rambhia et al., 2012; Vengrenyuk et al., 2012)). However, such small particles account for a very small proportion of the total calcification volume. The smallest particles ( $<0.025 \text{ mm}^3$ ) have lower sphericity than the next largest group due to the resolution of the scan resulting in a reduced number of faces composing the particles in the scan. The higher volume fraction of calcifications observed in iliofemoral plaques compared to carotid plaques is consistent with previous findings that Iliofemoral plaques express smaller quantities of osteoprotegerin, which inhibits the calcification of vascular smooth muscle cells (Heymann et al., 2012).

From the results of this study, the calcification stiffness is on average over 2 orders of magnitude higher than the isolated non-calcified fibrous tissue. This further demonstrates the importance of testing plaque constituents separately and modelling the plaques as



discrete constituents. The observed viscoelastic behaviour is possibly caused by fibre content that is present within calcifications as well as water content. The inverse finite element analysis provides a reasonable fit of the computational results to the experimental results. Therefore suggesting that the combination of a hyperelastic and a viscoelastic model is suitable for capturing the mechanical behaviour of calcifications. The stiffnesses outputted from the inverse finite element methods is within the lower range of calcification results reported in a previous nanoindentation study (Ebenstein et al., 2009). However these results differ from another previous nanoindentation study as the determined stiffnesses is 2 orders of magnitude less than the stiffnesses reported in Cahalane *et al.* (2018). This difference could potentially be explained by the length scales of the testing methods used. Nanoindentation is highly localised whereas the compression testing method used in this study will report a lower stress if there are small pores in the material. Physiological strain levels for atherosclerotic plaques have been observed to be between 0.15% - 0.63% strain (Gijssen et al., 2008). The strain range investigated mechanical testing well exceed the physiological levels. A limitation to the calcification testing is the lack of tensile data for material fitting due to the difficulties in testing particles small size and stiffness in tension. However the calcifications were modelled with a neo-Hookean material which at low strains has low asymmetry between the effective tension and compression moduli. The results from this study are of increased value for finite element applications as the present analysis is focused on a length scale similar to that of angioplasty and stenting procedures themselves. SEM analysis reveals collagen fibres embedded in the calcified particles. These collagen fibres may add to the toughness of the particles (compression of particles to 5% nominal strain did not cause fracture) and the presence of the fibres may account for the viscoelastic behaviour observed. Plaques are observed to have large eccentricity at the point of maximum stenosis this is concurrent that plaques generally form eccentrically (Steinman et al.,

2000). Eccentricity in stenoses complicate stress states in plaque as observed in previous computational studies (Gu et al., 2010; Iannaccone et al., 2014). This study presents the novel characterisation of the longitudinal orientations of calcifications in atherosclerotic plaques. This investigation has uncovered the largest calcifications in the plaques tend to be longitudinally aligned with the direction of the plaque centreline.

The viscoelastic behaviour observed in the current study exhibits a similar relaxation time to the results presented in Salunke *et al.* (2001). The long-term moduli observed in the present study are similar to those reported by Heiland *et al.* (2013). Such viscoelasticity behaviour indicates that lower stresses will be induced in plaques during angioplasty if low balloon/stent expansion rates are applied. The stiffness of non-calcified fibrous tissue reported in the current study exhibits strain stiffening. This observation has been noted in previous studies of composite plaques (Cunnane et al., 2016; Holzapfel et al., 2004; Maher et al., 2011, 2009; Salunke et al., 2001). The stiffnesses at lower strains uncovered in the current study are in agreement with the stiffnesses reported by a nano-indentation study by Ebenstein *et al.* (2009). However, nano-indentation experiments yield highly localised measurements at the surface of the plaque. Furthermore, Ebenstein *et al.* report a Young's modulus for the components of plaque, whereas the current study demonstrates that such materials are highly non-linear visco-hyperelastic. In the current study, isolated non-calcified fibrous tissue samples exhibit no statistically significant difference between axial and circumferential stiffnesses. Akyildiz *et al.* (2017) observed fibre directionality heterogeneously varied in all 3 directions (longitudinal, circumferential and radial) throughout analysed carotid plaques. Such heterogeneous multi-axial fibre orientations could result in effective isotropic behaviour in excised samples of fibrous tissue

In summary, the current study demonstrates that carotid and femoral plaques contain large calcified particles that are significantly stiffer than the surrounding fibrous tissue. This

suggests that finite element models of plaque should include site-specific fibrous material behaviour and explicit representations of calcified particles. The results of the current study provides key inputs for such models, leading to improved predictions of the stress state in atherosclerotic plaque during stenting and angioplasty procedures.

## 4.5 References

- Abedin, M., Tintut, Y., Demer, L.L., 2004. Vascular calcification: Mechanisms and clinical ramifications. *Arterioscler. Thromb. Vasc. Biol.* 24, 1161–1170. <https://doi.org/10.1161/01.ATV.0000133194.94939.42>
- Akyildiz, A.C., Strijkers, G.J., Baaijens, F.P.T., Chai, C.-K., Oomens, C.W.J., van der Lugt, A., Gijzen, F.J.H., 2017. 3D Fiber Orientation in Atherosclerotic Carotid Plaques. *J. Struct. Biol.* 200, 28–35. <https://doi.org/10.1016/j.jsb.2017.08.003>
- Barrett, H.E., Cunnane, E.M., Kavanagh, E.G., Walsh, M.T., 2016. On the effect of calcification volume and configuration on the mechanical behaviour of carotid plaque tissue. *J. Mech. Behav. Biomed. Mater.* 56, 45–56. <https://doi.org/10.1016/j.jmbbm.2015.11.001>
- Cahalane, R.M., Barrett, H.E., O'Brien, J.M., Kavanagh, E.G., Moloney, M.A., Walsh, M.T., 2018. Relating the mechanical properties of atherosclerotic calcification to radiographic density: A nanoindentation approach. *Acta Biomater.* 80, 228–236. <https://doi.org/10.1016/j.actbio.2018.09.010>
- Chang, C.K., Huded, C.P., Nolan, B.W., Powell, R.J., 2011. Prevalence and clinical significance of stent fracture and deformation following carotid artery stenting. *J. Vasc. Surg.* 54, 685–690. <https://doi.org/10.1016/j.jvs.2011.03.257>
- Conway, C., McGarry, J.P., Edelman, E.R., McHugh, P.E., 2017. Numerical Simulation of Stent Angioplasty with Predilatation: an Investigation into Lesion Constitutive Representation and Calcification Influence. *Ann. Biomed. Eng.* 45, 2244–2252. <https://doi.org/10.1007/s10439-017-1851-3.Numerical>
- Conway, C., McGarry, J.P., McHugh, P.E., 2014. Modelling of Atherosclerotic Plaque for use in a Computational Test-Bed for Stent Angioplasty. *Ann. Biomed. Eng.* 42, 2425–2439.
- Conway, C., Sharif, F., McGarry, J.P., McHugh, P.E., 2012. A Computational Test-Bed to Assess Coronary Stent Implantation Mechanics Using a Population-Specific Approach. *Cardiovasc. Eng. Technol.* 3, 374–387. <https://doi.org/10.1007/s13239-012-0104-8>
- Cunnane, E.M., Mulvihill, J.J.E., Barrett, H.E., Healy, D.A., Kavanagh, E.G., Walsh, S.R., Walsh, M.T., 2015. Mechanical, biological and structural characterization of human atherosclerotic femoral plaque tissue. *Acta Biomater.* 11, 295–303. <https://doi.org/10.1016/j.actbio.2014.09.024>
- Cunnane, E.M., Mulvihill, J.J.E., Barrett, H.E., Hennessy, M.M., Kavanagh, E.G., Walsh, M.T., 2016. Mechanical properties and composition of carotid and femoral atherosclerotic plaques: A comparative study. *J. Biomech.* 49, 3697–3704. <https://doi.org/10.1016/j.jbiomech.2016.09.036>
- Ebenstein, D.M., Coughlin, D., Chapman, J., Li, C., Pruitt, L.A., 2009. Nanomechanical properties of calcification, fibrous tissue, and hematoma from atherosclerotic plaques. *J. Biomed. Mater. Res. - Part A* 91, 1028–1037. <https://doi.org/10.1002/jbm.a.32321>

- Gijssen, F. J. H. et al. (2008) ‘Strain distribution over plaques in human coronary arteries relates to shear stress’, *American Journal of Physiology - Heart and Circulatory Physiology*, 295(4), pp. 1608–1614. doi: 10.1152/ajpheart.01081.2007.
- Gu, L., Zhao, S., Muttyam, A.K., Hammel, J.M., 2010. The Relation Between the Arterial Stress and Restenosis Rate After Coronary Stenting. *J. Med. Device*. 4, 031005. <https://doi.org/10.1115/1.4002238>
- Heiland, V.M., Forsell, C., Roy, J., Hedin, U., Gasser, T.C., 2013. Identification of carotid plaque tissue properties using an experimental-numerical approach. *J. Mech. Behav. Biomed. Mater.* 27, 226–238. <https://doi.org/10.1016/j.jmbbm.2013.05.001>
- Heymann, M.F., Herisson, F., Davaine, J.M., Charrier, C., Battaglia, S., Passuti, N., Lambert, G., Gouëffic, Y., Heymann, D., 2012. Role of the OPG/RANK/RANKL triad in calcifications of the atheromatous plaques: Comparison between carotid and femoral beds. *Cytokine* 58, 300–306. <https://doi.org/10.1016/j.cyto.2012.02.004>
- Holzappel, G.A., Sommer, G., Regitnig, P., 2004. Anisotropic Mechanical Properties of Tissue Components in Human Atherosclerotic Plaques. *J. Biomech. Eng.* 126, 657. <https://doi.org/10.1115/1.1800557>
- Hutcheson, J.D., Maldonado, N., Aikawa, E., 2014. Small entities with large impact. *Curr. Opin. Lipidol.* 25, 327–332. <https://doi.org/10.1097/mol.0000000000000105>
- Iannaccone, F., Debusschere, N., De Bock, S., De Beule, M., Van Loo, D., Vermassen, F., Segers, P., Verhegghe, B., 2014. The influence of vascular anatomy on carotid artery stenting: A parametric study for damage assessment. *J. Biomech.* 47, 890–898. <https://doi.org/10.1016/j.jbiomech.2014.01.008>
- Kelly-Arnold, A., Maldonado, N., Laudier, D., Aikawa, E., Cardoso, L., Weinbaum, S., 2013. Revised microcalcification hypothesis for fibrous cap rupture in human coronary arteries. *Proc. Natl. Acad. Sci.* 110, 10741–10746. <https://doi.org/10.1073/pnas.1308814110>
- Lawlor, M.G., O’Donnell, M.R., O’Connell, B.M., Walsh, M.T., 2011. Experimental determination of circumferential properties of fresh carotid artery plaques. *J. Biomech.* 44, 1709–1715. <https://doi.org/10.1016/j.jbiomech.2011.03.033>
- Li, F., McDermott, M., Li, D., Carroll, T., Hippe, D., Kramer, C., Fan, Z., Zhao, X., Hatsukami, T., Chu, B., Wang, J., Yuan, C., 2010. The association of lesion eccentricity with plaque morphology and components in the superficial femoral artery: A high-spatial-resolution, multi-contrast weighted CMR study. *J. Cardiovasc. Magn. Reson.* 12, 1–8. <https://doi.org/10.1186/1532-429X-12-37>
- Liu, B., Zhang, X., Wang, L., Hong, H., 2008. Fluidization of non-spherical particles: Sphericity, Zingg factor and other fluidization parameters. *Particuology* 6, 125–129. <https://doi.org/10.1016/j.cpart.2007.07.005>
- M Moerman, K., 2018. GIBBON: The Geometry and Image-Based Bioengineering add-On. *J. Open Source Softw.* 3, 506. <https://doi.org/10.21105/joss.00506>

- Maher, E., Creane, A., Sultan, S., Hynes, N., Lally, C., Kelly, D.J., 2011. Inelasticity of Human Carotid Atherosclerotic Plaque. *Ann. Biomed. Eng.* 39, 2445–2455. <https://doi.org/10.1007/s10439-011-0331-4>
- Maher, E., Creane, A., Sultan, S., Hynes, N., Lally, C., Kelly, D.J., 2009. Tensile and compressive properties of fresh human carotid atherosclerotic plaques. *J. Biomech.* 42, 2760–2767. <https://doi.org/10.1016/j.jbiomech.2009.07.032>
- Maldonado, N., Kelly-Arnold, A., Vengrenyuk, Y., Laudier, D., Fallon, J.T., Virmani, R., Cardoso, L., Weinbaum, S., 2012. A mechanistic analysis of the role of microcalcifications in atherosclerotic plaque stability: potential implications for plaque rupture. *Am. J. Physiol. Circ. Physiol.* 303, H619–H628. <https://doi.org/10.1152/ajpheart.00036.2012>
- Mulvihill, J.J., Cunnane, E.M., McHugh, S.M., Kavanagh, E.G., Walsh, S.R., Walsh, M.T., 2013. Mechanical, biological and structural characterization of in vitro ruptured human carotid plaque tissue. *Acta Biomater.* 9, 9027–9035. <https://doi.org/10.1016/j.actbio.2013.07.012>
- Pence, T.J., Gou, K., 2015. On compressible versions of the incompressible neo-Hookean material 20, 157–182. <https://doi.org/10.1177/1081286514544258>
- Rambhia, S.H., Liang, X., Xenos, M., Alemu, Y., Maldonado, N., Kelly, A., Chakraborti, S., Weinbaum, S., Cardoso, L., Einav, S., Bluestein, D., 2012. Microcalcifications increase coronary vulnerable plaque rupture potential: A patient-based micro-ct fluid-structure interaction study. *Ann. Biomed. Eng.* 40, 1443–1454. <https://doi.org/10.1007/s10439-012-0511-x>
- Salunke, N.V., Topoleski, L.D.T., Humphrey, J.D., Mergner, W.J., 2001. Compressive stress-relaxation of human atherosclerotic plaque. *J. Biomed. Mater. Res.* 55, 236–241. [https://doi.org/10.1002/1097-4636\(200105\)55:2<236::AID-JBM1010>3.0.CO;2-F](https://doi.org/10.1002/1097-4636(200105)55:2<236::AID-JBM1010>3.0.CO;2-F)
- Shaikh, S., Brittenden, J., Lahiri, R., Brown, P.A.J., Thies, F., Wilson, H.M., 2012. Macrophage subtypes in symptomatic carotid artery and femoral artery plaques. *Eur. J. Vasc. Endovasc. Surg.* 44, 491–497. <https://doi.org/10.1016/j.ejvs.2012.08.005>
- Stary, H.C., 2002. Natural history of calcium deposits in atherosclerosis progression and regression. *Z. Kardiol.* 89, S028–S035. <https://doi.org/10.1007/s003920070097>
- Steinman, D.A., Poepping, T.L., Tambasco, M., Rankin, R.N., Holdsworth, D.W., 2000. Flow patterns at the stenosed carotid bifurcation: Effect of concentric versus eccentric stenosis. *Ann. Biomed. Eng.* 28, 415–423. <https://doi.org/10.1114/1.279>
- Taniwaki, H., Shoji, T., Emoto, M., Kawagishi, T., Ishimura, E., Inaba, M., Okuno, Y., Nishizawa, Y., 2002. Femoral artery wall thickness and stiffness in evaluation of peripheral vascular disease in type 2 diabetes mellitus. *Atherosclerosis* 158, 207–214. [https://doi.org/10.1016/s0021-9150\(01\)00414-2](https://doi.org/10.1016/s0021-9150(01)00414-2)
- Teng, Z., Tang, D., Zheng, J., Woodard, P.K., Hoffman, A.H., 2009. An experimental study on the ultimate strength of the adventitia and media of human atherosclerotic carotid

arteries in circumferential and axial directions. *J. Biomech.* 42, 2535–2539.  
<https://doi.org/10.1016/j.jbiomech.2009.07.009>

Vengrenyuk, Y., Cardoso, L., Weinbaum, S., Laudier, D., Fallon, J.T., Maldonado, N., Virmani, R., Kelly-Arnold, A., 2012. A mechanistic analysis of the role of microcalcifications in atherosclerotic plaque stability: potential implications for plaque rupture. *Am. J. Physiol. Circ. Physiol.* 303, H619–H628.  
<https://doi.org/10.1152/ajpheart.00036.2012>

Walsh, M.T., Cunnane, E.M., Mulvihill, J.J., Akyildiz, A.C., Gijssen, F.J.H., Holzapfel, G.A., 2014. Uniaxial tensile testing approaches for characterisation of atherosclerotic plaques. *J. Biomech.* 47, 793–804. <https://doi.org/10.1016/j.jbiomech.2014.01.017>

Wirtz, D. C. et al. (2000) ‘Critical evaluation of known bone material properties to realize anisotropic FE-simulation of the proximal femur’, *Journal of Biomechanics*, 33(10), pp. 1325–1330. doi: 10.1016/S0021-9290(00)00069-5.

Yeoh, O. H., (1993) ‘Some forms of the strain energy function for rubber’, *Rubber Chemistry and technology*, 66(5), pp. 754-771

## Appendix 4A

Below is the MATLAB code measuring the geometric properties of plaque components.

```
clear; close all; clc;

%%
% Plot settings
markerSize=10;
figStruct.Color='k'; % Figure background color
figStruct.ColorDef='black'; % Setting colordefinitions to black
%%
% Path names
pathName='C:\Users\Brian\Documents\MATLAB\carotid_calc_stls/test';

%%
% Control parameters
headerLine='Id, Centroid_x, Centroid_y, Centroid_z, Area, Volume, Triangles, Nodes, ellipsoid radius X, ellipsoid radius Y, ellipsoid radius Z, ellipsoid angle X, ellipsoid angle Y, ellipsoid angle Z';
minVolume=1;
plotOn=1;

if plotOn==1
    [Fs, Vs, ~]=geoSphere(2,1);
end
%%
%

files = dir(fullfile(pathName, '*.stl'));
files={files(1:end).name};
files=sort(files(:));
numFiles=numel(files);

for fileID=1:1:numFiles

    % Get/set current file names
    fileNameNow=fullfile(pathName, files{fileID});
    [~, fileNameClean, ~]=fileparts(fileNameNow);
    saveName_CSV=fullfile(pathName, [fileNameClean, '.csv']);

    % Open file for writing and write header line
    fileOut = fopen(saveName_CSV, 'w'); % Open output file for writing
    fprintf(fileOut, '%s \n', headerLine); % Write header line

    % Import the STL file
    stlStruct=import_STL(fileNameNow);
    F_all=stlStruct.solidFaces{1};
    V_all=stlStruct.solidVertices{1};
    C_all=zeros(size(F_all,1),1);
```



```

[F_all,V_all]=mergeVertices(F_all,V_all); % Merge nodes since nodes are not recycled
in an STL
F_all_sort=sort(F_all,2);
logicValid= ~(F_all_sort(:,1)==F_all_sort(:,2) | F_all_sort(:,2)==F_all_sort(:,3) |
F_all_sort(:,3)==F_all_sort(:,1));
F_all=F_all(logicValid,:);
[F_all,V_all]=patchCleanUnused(F_all,V_all);

% Perform grouping of (nodes and) faces
[~,faceGroupLabel]=groupVertices(F_all,[],1); % Grouping to separate components
[faceGroupLabel_uni,ind1,ind2,groupSizes]=cunique(faceGroupLabel); % Get group
sizes
groupSizes=groupSizes(ind1); % Unique group size set
[groupSizes,indSort]=sort(groupSizes,'descend'); % Get sort order for groups
faceGroupLabel_uni=faceGroupLabel_uni(indSort); % Sort face group labelling
numGroups=numel(faceGroupLabel_uni); % Number of groups

% Visualize grouping
if plotOn==1
    hf=cFigure(figStruct); hold on;
    gpatch(F_all,V_all,faceGroupLabel,'none',0.7);
    colormap(gca,rand(numGroups,3));
    axisGeom; axis on;
    camlight headlight;
    lighting gouraud;
end
%
% Compute group features
groupCountValid=1;
for qGroup=1:1:numGroups

    % Get current face/vertex set
    F_group_now=F_all(faceGroupLabel==faceGroupLabel_uni(qGroup),:);
    V_group_now=V_all;
    [F_group_now,V_group_now]=patchCleanUnused(F_group_now,V_group_now);

    % Get volume
    volume_now=triSurfVolume(F_group_now,V_group_now);

    if volume_now>=minVolume
        % Fit an ellipsoid
        [M,ellipsStretchFit_now,R_fit,MU]=ellipsoidFit_centered(V_group_now); % Fit
ellipsoid to current group

        % Get euler angles from ellipsoid fit
        R_now=R_fit(1:3,1:3);
        [ellipsoidAngles_now]=DCM2euler(R_now);

        % Get centroid
        centroid_now=triSurfCentroid(F_group_now,V_group_now);
        area_now=sum(patch_area(F_group_now,V_group_now));

```

```
%Get number of vertices and faces
numFaces_now=size(F_group_now,1);
numVertices_now=size(V_group_now,1);

%Create current text line
tLine=[sprintf('%d, ',groupCountValid),...
       sprintf('%f, ',centroid_now),...
       sprintf('%f, ',area_now),...
       sprintf('%f, ',volume_now),...
       sprintf('%f, ',numFaces_now),...
       sprintf('%f, ',numVertices_now),...
       sprintf('%f, ',ellipsStretchFit_now),...
       sprintf('%f, ',ellipsoidAngles_now)];

fprintf(fileOut,'%s \n',tLine);
groupCountValid=groupCountValid+1;

if plotOn==1
   (gcf; figure(hf); disp("); % This line helps to avoid graphics bug on linux

    Ve=Vs.*ellipsStretchFit_now(ones(size(Vs,1),1),:); %Stretch
    Ve=(R_now*Ve)'; %Rotate
    Ve=Ve+centroid_now(ones(size(Vs,1),1),:); %Translate
    gpatch(Fs, Ve, 'kw', 'none', 0.5);
    plotV(centroid_now, 'k+', 'MarkerSize', markerSize);
    drawnow;
end
end
end

end

fclose(fileOut);
```

## Appendix 4B

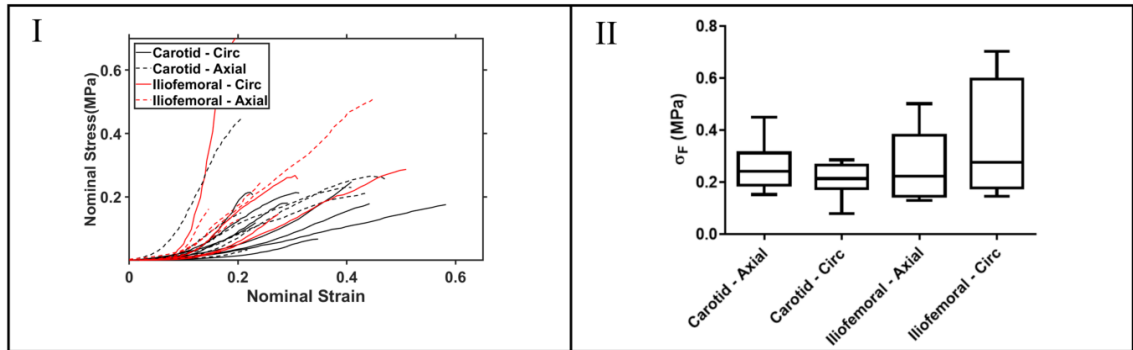


Figure A3: (I) Nominal stress-strain data for isolated non-calcified carotid and iliofemoral fibrous plaque samples in the circumferential and the axial directions tested to up to failure. (II) Tukey boxplots illustrating the nominal failure stress ( $\sigma_F$ ) of non-calcified carotid and iliofemoral fibrous plaque samples in the circumferential and the axial directions.

# 5 STENT AND BALLOON ANGIOPLASTY IN CALCIFIED ATHEROSCLEROTIC STENOSES

## 5.1 Introduction

In the US 1.8 million stents are implanted every year (iDataResearch, 2018) and it is estimated that around 10% of the world's population have peripheral arterial disease (Peach et al., 2012). The most common surgical treatments for atherosclerotic stenosis are endarterectomy, bypass, angioplasty, and stenting. Complications due to stenting can arise from the geometry of the stenosis and the increased plaque stiffness due to the formation of calcifications. An improved understanding of the effect of plaque constituents during stenting and balloon angioplasty can potentially guide the stratification of patients for differing treatment options.

Previous stenting computational studies have typically modelled calcified plaques as a homogenous material (A. Karimi et al., 2014; A. Karimi et al., 2014; Migliavacca et al., 2004; Pericevic et al., 2009). This homogeneous material is typically modelled as hyperelastic, with material properties typically being calibrated using mechanical test

data reported for whole excised plaques (Cunnane et al., 2015; Loree et al., 1994). This approach does not account for the composite nature of plaque and for the resultant stress concentrations due to stiffness mismatch of the plaque constituents. Discrete representations of plaque constituents in a finite element model could potentially provide improved predictions of the stress state in the plaque during angioplasty and stenting. Simulations reveal that the presence of calcifications reduces the lumen gain in stenosed arteries (Conway et al., 2014; García et al., 2012; Pericevic et al., 2009). Previous computational studies have investigated curvature (Conway et al., 2012), geometric properties of lipid pools (Cilla et al., 2012), stent oversizing (Gökgöl et al., 2017), and eccentricity (Wei et al., 2019) on the deformation of plaque during loading. There have been investigations detailing the analysis of the effect of lipid properties (Cilla et al., 2012; Conway et al., 2012; Wei et al., 2019).

Previous studies have investigated calcified inclusions in stenting in fibro-calcific plaques. García et al. (2012) investigated stenting in an idealised atherosclerotic artery with a single calcified particle, Morlacchi et al. (2014) also investigated stenting and stiffened the material behaviour of a localised collection of elements to represent a single calcification and (Conway et al., 2014, 2017a) implemented a similar method for single scattered elements to represent calcifications. These calcifications do not correlate with the calcification distribution observed in Chapter 4. Fan et al. (2016) modelled stenting in a patient specific geometry with fibrous material and calcifications, however they used the properties derived from calcified plaques (Loree et al., 1994) rather than discrete calcified particles, potentially underestimating the stiffness. Buffinton and Ebenstein (2014) pressurised an array of single 2D calcification geometries demonstrating the effects on interface stresses, however it does not evaluate the 3D stress states and effect of the inclusion of multiple stiff calcifications. The aim of this study is to investigate the effect of eccentricity, calcification volume and calcification orientation on balloon

angioplasty and the effect of stent strut thickness and calcification volume on stenting. This will provide insights into the efficacy of these treatments under differing atherosclerotic plaque constituent configurations and volumes.

In this study data generated from  $\mu$ CT to investigate the effect on calcification orientations and volume on stenting and balloon angioplasty are implemented in finite element models. Also, the effect of eccentricity and increased stent outward force is examined on calcified plaque mechanics. Section 5.2.1 details the creation of the atherosclerotic artery and calcifications models, section 5.2.2 and section 5.2.3 explores balloon angioplasty and stenting models respectively. Then section 5.3 details the results of the investigations and modelling, while section 5.4 discusses the results and its implications for plaque biomechanics.

## 5.2 Methodology

### 5.2.1 Atherosclerotic plaque geometry construction

As shown in Figure 5.2(A), an idealised femoral artery of length 50mm with a stenosed section of 20mm is created using finite element pre-processing software Abaqus CAE. An internal vessel diameter of 8mm is assumed (Irina et al., 2019), with a vessel wall thickness of 0.6 mm (van den Munckhof et al., 2012). Eccentric and concentric plaque configurations are created with equal internal/lumen diameters (representing a 60% area occlusion). The lumen is offset from the vessel centreline by 1mm in the case of eccentric model geometries based on the eccentricity models reported in Wei et al. (2019).

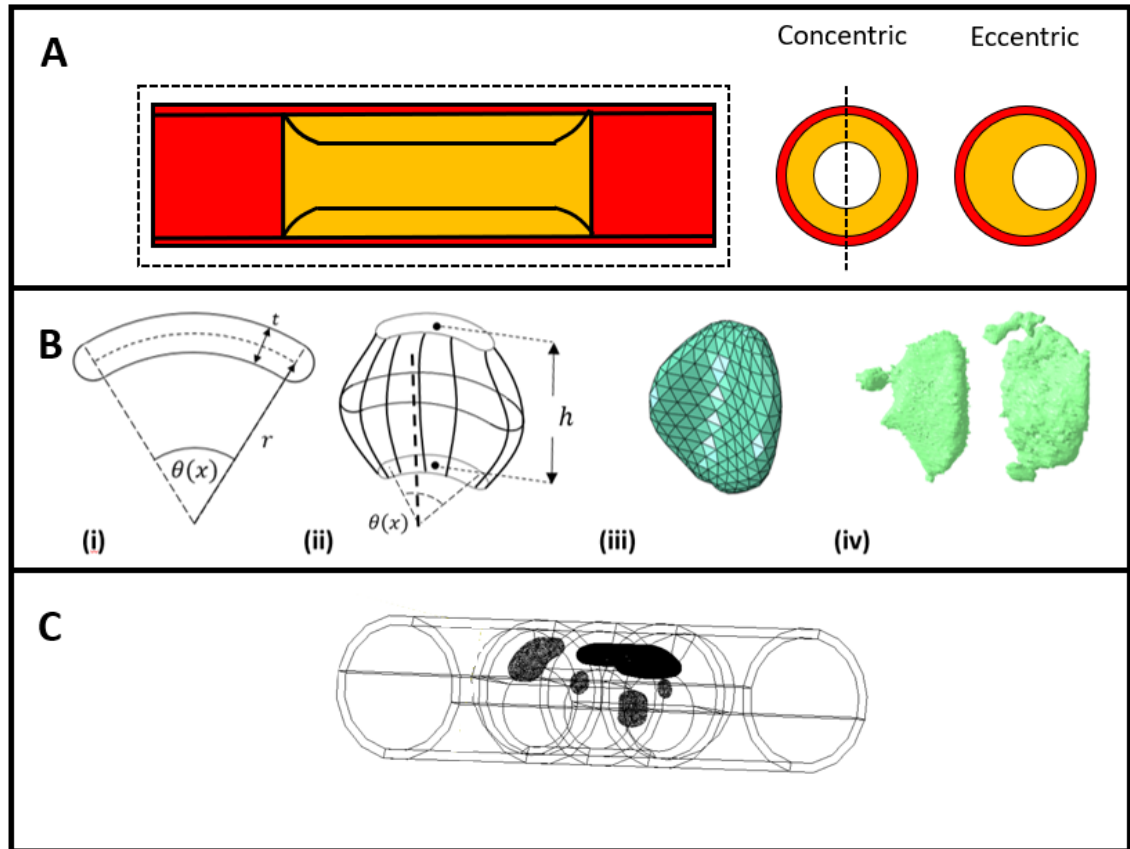


Figure 5.1. (A) Illustration of constructed geometry for eccentric and concentric fibrous occlusions (yellow) in an idealised cylindrical vessel (red). (B) Calcification mesh geometry is generated in MATLAB based on  $\mu$ CT reconstructions detailed in Chapter 4. They are constructed by multiple cross sections (i), stacked between two points of height  $h$  and then lofted between the exterior surfaces (ii) and then the mesh part is created (iii). (iv) The created mesh parts are representative of calcifications observed in  $\mu$ CT (iv). (C) Wireframe of an eccentric plaque model with calcified inclusions comprising 20% of the plaque volume.

A MATLAB script has been developed to create geometries of calcified inclusions as seen in Figure 5.1(B). Based on  $\mu$ CT scans presented in Chapter 4, calcifications are constructed so that they curve around the lumen of the plaque (in the circumferential direction). This enables for the inclusion of more realistic calcification particles in the curved plaque geometries. Geometric design parameters for each cross-section include

thickness ( $t$ ), midline radius ( $r$ ), height ( $h$ ), and angle width that varies on the position along the longitudinal axis ( $\theta(h)$ ). The sections are then lofted to create a surface and meshed. The resulting mesh part is representative of calcifications observed in  $\mu$ CT data. Figure 5.1(C) illustrates a wireframe example of a plaque model with 20% of the plaque volume comprised of calcifications.





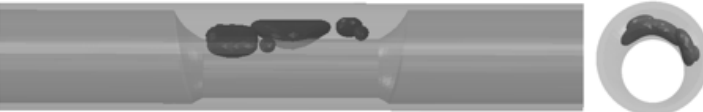


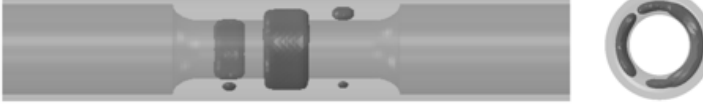
Eccentric Plaque	Concentric Plaque
0% Calcification Volume (E0)	0% Calcification Volume (C0)
<b>A</b> 	<b>B</b> 
10% Calcification Volume (E10)	20% Calcification – Longitudinal (C20L)
<b>C</b> 	<b>D</b> 
20% Calcification Volume (E20)	20% Calcification – Circumferential (C20C)
<b>E</b> 	<b>F</b> 

Figure 5.2. Model generation of atherosclerotic arteries with eccentric and concentric plaque geometries. Calcification volume is varied in eccentric plaque models and calcification orientation is varied in concentric plaque models.

As

shown

in

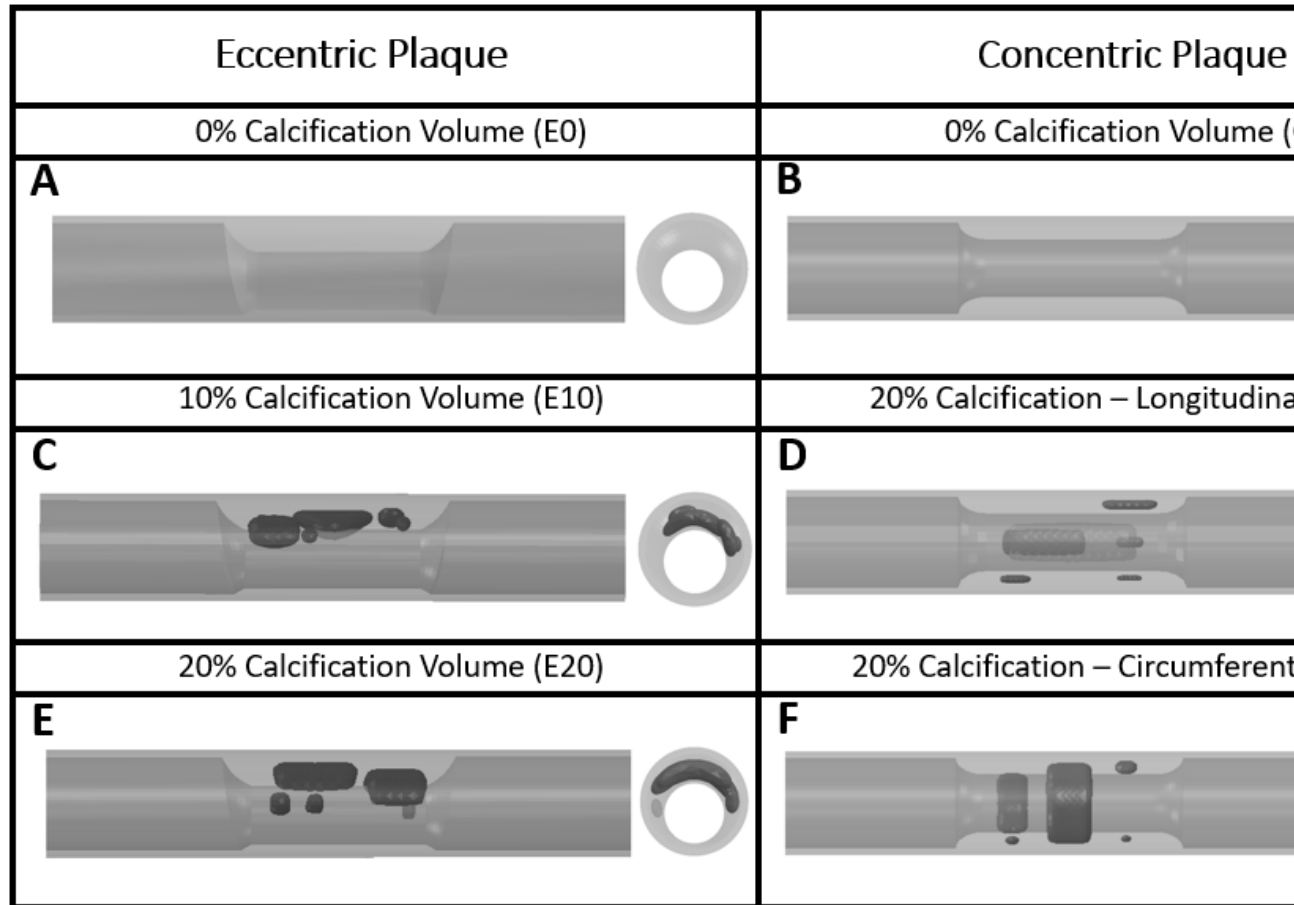


Figure 5.2, six plaque models are created: an eccentric plaque with no calcifications (E0, Figure 5.2A); a concentric plaque with no calcifications (C0, Figure 5.2B); an eccentric plaque with 10% of the plaque volume comprised of calcifications (E10, Figure 5.2C); a concentric plaque with 20% of the plaque volume comprised of longitudinally aligned calcifications (C20L, Figure 5.2D); an eccentric plaque with 20% of the plaque volume comprised of calcifications (E20, Figure 5.2E); and a concentric plaque with 20% of the plaque volume comprised of circumferentially aligned calcifications (C20C, Figure 5.2F). Six calcifications are generated for each of the calcified models, with the same volume distribution as observed from the femoral plaque results in the previous chapter. Calcifications in the eccentric models (E10 and E20) are mostly longitudinally aligned but have a maximum aspect ratio of 1.5:1 in the longitudinal direction. Each calcification in the models C20L and C20C had aspect ratios of 3:1 in the longitudinal direction and

the circumferential directions respectively. Each of the models are created using tetrahedral elements, the number of these elements in each model are; E0 – 98764; E10 – 26761; E20 – 88864; C0 – 98674; C20L – 32576; and C20C – 87513. The three main points of comparison for the array of models are:

- The influence of eccentric versus concentric on the fibrous models (E0 and C0).
- The influence of increasing calcification volume in the eccentric plaque models (E0, E10, and E20).
- The influence of calcification aspect ratio in the concentric models (C20L and C20C).

### 5.2.2 Balloon angioplasty finite element model construction

In each of the six models, balloon angioplasty is simulated by expanding a rigid cylindrical surface to the diameter of the healthy artery (8 mm) in the models shown in Figure 5.2 as per the suggested “*instructions-for-use (IFU) documents*” for commercially available angioplasty balloons (Merit; TERUMO, 2016) . The plaque and artery sections are meshed using C3D10 (second-order tetrahedral) elements. Calcifications are meshed using C3D4 (first-order tetrahedral) elements, and the balloon is meshed using SFM3D4R (quadrilateral surface element with reduced integration) elements. Based on material model calibration performed in Chapter 4, a Yeoh hyperelastic constitutive law with a two-term Prony viscoelastic component is used to model the plaque fibrous tissue. Calcifications are modelled using neo-Hookean hyperelasticity with one-term Prony

series viscoelasticity, again following from analyses performed in Chapter 4. The artery is modelled using an Ogden (n=2) hyperelastic material law with model parameter fitted to the experimental test data for femoral arterial tissue reported by Sokolis (2010). The plaque is assumed to be rigidly bonded to the internal wall of the vessel in all simulations. Contact conditions between the balloon and the plaque/vessel are defined using surface to surface contact implementing hard normal contact with a tangential penalty of 0.02. Lumen gain achieved in angioplasty models is calculated as;

$$Lumen\ Gain = \frac{\phi_i - \phi_o}{\phi_a - \phi_o} \quad (5-1)$$

where  $\phi_i$  is the deformed diameter during angioplasty,  $\phi_o$  is the initial stenosed diameter, and  $\phi_a$  is the diameter of a healthy unblocked vessel (i.e. the target lumen diameter following angioplasty). The radial force required to open the stenosis to the healthy lumen diameter is calculated as this can be related to the inflation pressure of the simulated angioplasty balloon.

Table 5.1. Material Parameters describing healthy arterial tissue using the Ogden (n=2) constitutive law. Properties based on the experimental testing of Sokolis (2010).

Parameter	$\alpha_1$	$\alpha_2$	$\mu_1$	$\mu_2$	$D_1$	$D_2$
	0.00618	0.00618	34.403	-34.403	37.763	37.763

### 5.2.3 Stent angioplasty simulations

A MATLAB script is used to generate two generic stent geometries, each of uncrimped length 32mm and internal uncrimped diameter of 9mm. The stents are generated from repeating sigmoidal curves as shown in Figure 5.3 (A). These diameter sizes are based on IFUs of commercially available endovascular stents (GORE, 2014), which state that a

stenosed artery of with healthy lumen diameter of 8mm should be treated with an oversized stent of diameter 9mm. Square cross-sections are assumed for the struts of both geometries. As shown in Figure 5(B), the only difference between the two stent model geometries is the choice of strut-thickness/width. One model consists of struts with cross-section  $150\mu\text{m} \times 150\mu\text{m}$ ; one model consists of thicker struts with cross-section  $220\mu\text{m} \times 220\mu\text{m}$ . These strut dimensions fall in the ranges of commercially available devices (Liang, 2016). The stent material (Nitinol) is modelled as a superelastic shape memory alloy (Abaqus Theory Manual, DS SIMULIA, USA). Material properties are presented in Table 5.1 (McGrath et al., 2016). Stent geometries are meshed using C3D8 (8-node linear brick) elements. Since most plaques observed clinically are eccentric (Steinman et al., 2000), only the eccentric models (E0, E10, and E20) are used for stenting simulations.

Table 5.2 Nitinol properties used in the Abaqus constitutive model.

Parameter	Value
Austenite elasticity (MPa)	53,001
Austenite Poisson's ratio	0.3
Martensite elasticity (MPa)	21,500
Martensite Poisson's ratio	0.3
Transformation strain	0.038
Start transformation loading (MPa)	434
End transformation loading (MPa)	500
Reference temperature (°C)	37
Start transformation unloading (MPa)	210.3
End transformation unloading (MPa)	138.7

Start transformation stress during loading in compression (MPa)	434
Volumetric transformation strain	0.038

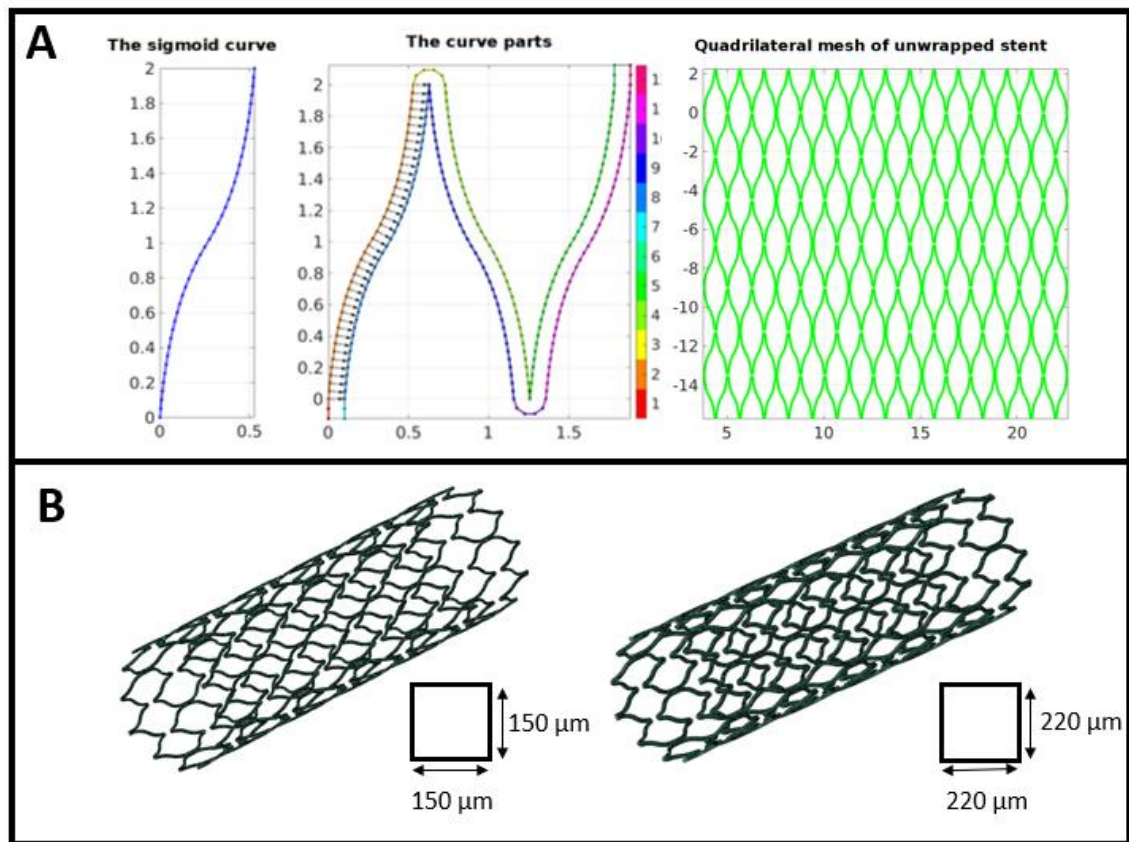


Figure 5.3. (A) MATLAB is used to generate stent geometries comprised of sigmoid curves and connecting struts. (B) Two stent geometries are created with inner diameters of 9mm, one with stent strut of thickness and width of 150  $\mu\text{m}$  and 220  $\mu\text{m}$ .

The radial force is measured by crimping the self-expanding stents using a rigid cylinder of surface elements around the stents reducing the outer diameter of the stent to 4.6mm. Following this, the cylinder is expanded to the maximum stent diameter.

The deployment of the stent in the occluded section of the vessel is simulated as follows. The stents are crimped as described previously and positioned in the vessel so that the centre point of the stent is aligned with the centre point of the occluded lumen. The crimper is then expanded with contact defined between the external surface of the stent and internal lumen surface. As the stent expands, contacting the plaque/vessel, it results in the computation of lumen gain.

All computational models and configurations in this study are computed using dynamic analysis in Abaqus/Explicit (V6.14) and the ratio of the kinetic energy to internal energy is below 5% during each of the simulations. Each of the models were calculated using a target time increment of 1E-6 seconds, which is sufficiently smaller than the minimum stable time increment to ensure accuracy.

## 5.3 Results

### 5.3.1 Balloon angioplasty simulations

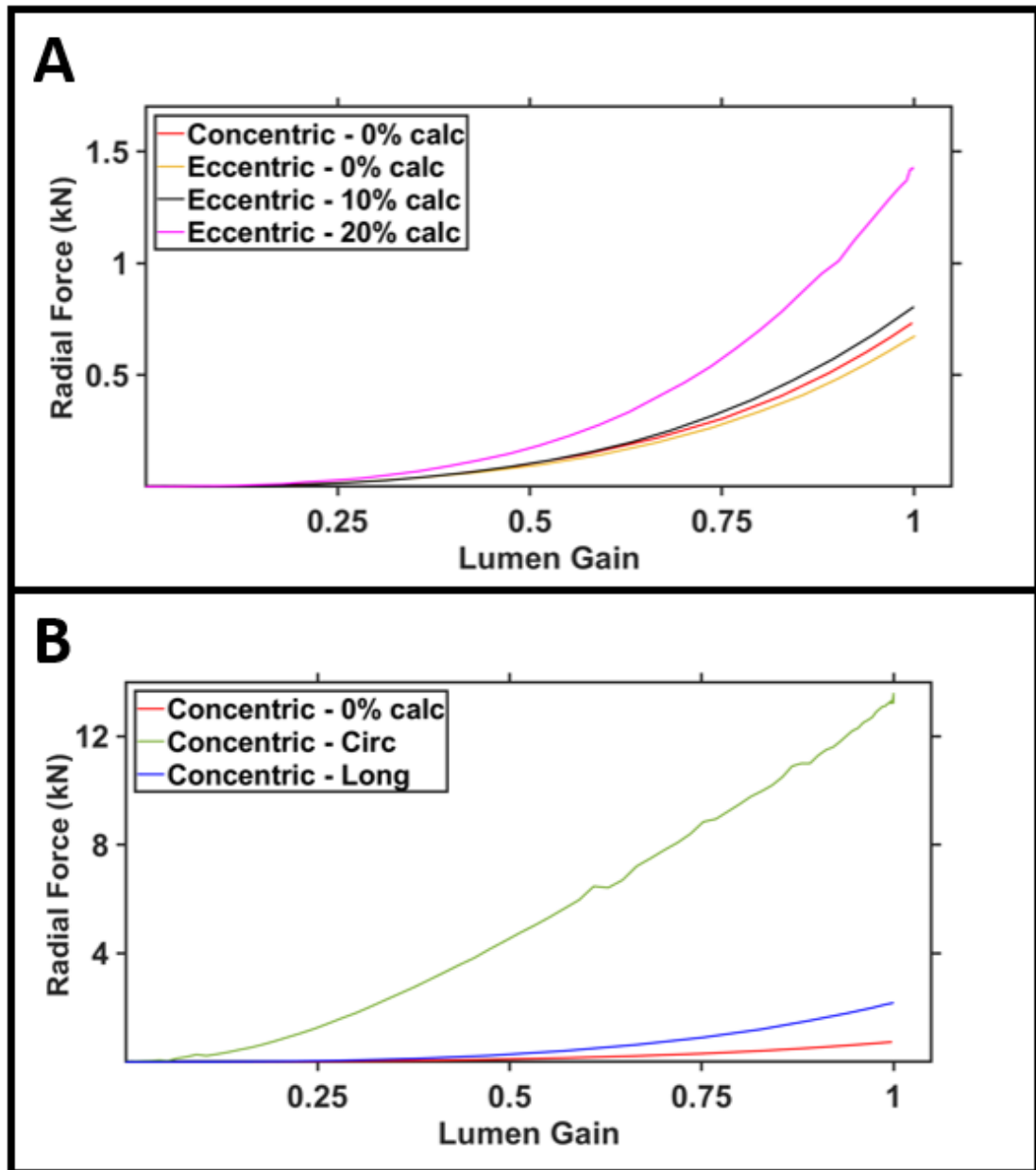


Figure 5.4. Radial force versus lumen gain for balloon angioplasty models comparing; (A) Concentric and eccentric models with no calcification (C0 and E0) and eccentric models with increasing calcification content (E0,E10, and E20) (B) Concentric plaques without calcification (C0) and two with differing calcification aspect ratios (C20L and C20C)



Table 5.3. Computed inflation pressure required to deform the plaque so that the original (unblocked) lumen area is restored.

Plaque Model		Inflation Pressure (MPa)
Eccentric	0% Calcification (E0)	0.90
	10% Calcification (E10)	1.10
	20% Calcification (E20)	1.90
Concentric	0% Calcification (C0)	0.97
	20% - Longitudinal (C20L)	2.92
	20% - Circumferential (C20C)	18.04

As shown in Figure 5.4(A), a lower radial force is required to fully restore the lumen area for an eccentric plaque containing 0% calcification (E0, max force=0.68 kN) compared to a concentric plaque containing 0% calcification (C0, max force=0.73 kN). A higher radial force is required to restore the lumen area in eccentric plaques with higher calcifications content (E0 max force=0.68 kN; E10, max force=0.80 kN; E20, max force=1.43 kN). Figure 5.4(B) shows the radial force required to achieve full lumen restoration is higher in a concentric plaque with circumferentially aligned calcifications (C20C, max force=13.5 kN) compared to a concentric plaque with longitudinally aligned calcifications (C20L, max force=2.2 kN).

Table 5.3 presents the pressure that must be applied by the balloon to the internal surface of the plaque/vessel in order to fully restore the lumen to the healthy unblocked area. A much higher pressure must be applied in the case of the C20C blockage than that computed for the other plaque configurations.

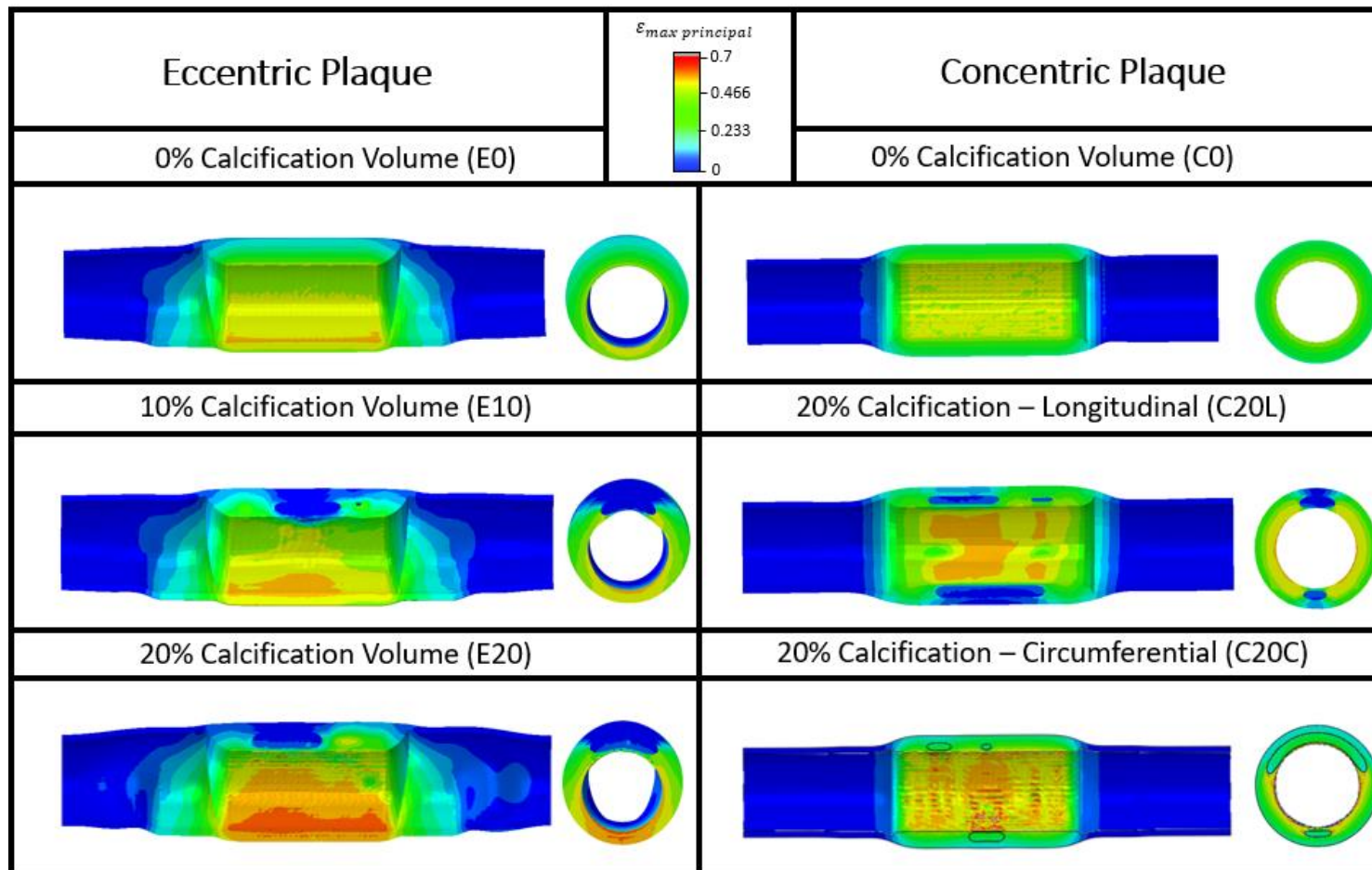


Figure 5.5. Maximum principal strain distribution during balloon angioplasty in concentric and eccentric plaque models with varying calcification of volumes and orientations

The finite element predictions of strain distribution in each of the balloon angioplasty simulations are shown in Figure 5.5. The maximum principal strain in the eccentric plaques (E0, E10, and E20) increases with increasing calcification volume. In all plaques that contain calcified particles (E10, E20, C20L, C20C) the maximum strain in the plaques is located in the fibrous tissue away from the calcifications, while low levels of strain occur in the region of the calcified particles. The high stiffness calcifications result in low levels of strain. Eccentric plaques (E0, E10, and E20) exhibit highest maximum strains at the thinnest part of the plaques during balloon angioplasty. The maximum strain in the fibrous tissue increases as the calcification content increases. Simulations also predict that circumferentially aligned calcifications (C20C) lead to a higher strain in the fibrous tissue than that computed for longitudinally aligned calcifications (C20L).

The primary effect of the balloon angioplasty is the circumferential strain on the plaque and artery at a given cross-section of a plaque. If a calcification occupies a large proportion of area in the cross-section, in order to achieve full lumen gain extremely high strains (greater than 0.8 strain) is required in the fibrous tissue. The stiff section of calcification will not strain thus requiring high strain in the fibrous tissue that is in series with the calcified particles. This is evident in the calcified models in Figure 5.5. In C20C the total angle ( $\theta$ ) of calcification in the cross-section is 2.48 radians and there is a maximum localised strain of 0.66. In C20L the total angle ( $\theta$ ) of calcification in the cross-section is 1.38 radians and there is a maximum localised strain of 0.55. With more calcifications in the circumferential direction the more force required to achieve lumen gain.

## 5.3.2 Stent radial force test

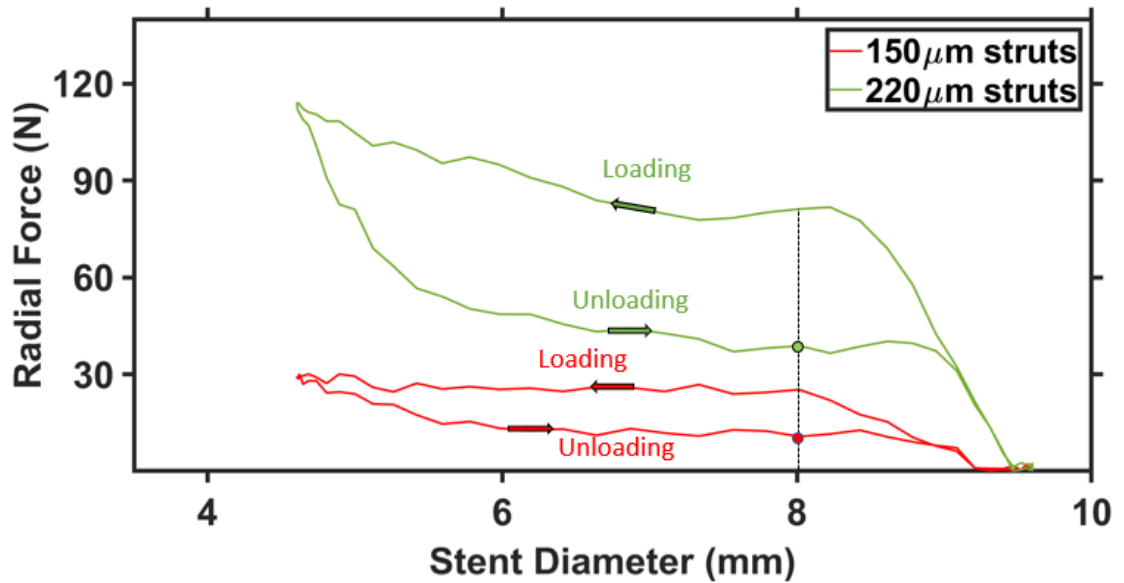


Figure 5.6. Computed relationship between radial force and stent diameter during crimping to a diameter of 4.6 mm from an undeformed diameter of inner diameters 9 mm (loading curve), followed by uncrimping (unloading curve). Results are shown for two stents designs: 150  $\mu\text{m}$  x 150  $\mu\text{m}$  square struts; 220  $\mu\text{m}$  x 220  $\mu\text{m}$  square struts. The target diameter is indicated by the dotted line and coloured dots denote the outward force at the target diameter.

Figure 5.6 shows the relationship between radial force and stent diameter during crimping to a diameter of 4.6 mm (loading), followed by uncrimping (unloading). Results are shown for two stents designs: 150  $\mu\text{m}$  x 150  $\mu\text{m}$  square struts; 220  $\mu\text{m}$  x 220  $\mu\text{m}$  square struts. In both cases the undeformed stent inner diameter is 9 mm. The computed radial force at full-crimp (diameter = 4.6 mm) for the stent with 220  $\mu\text{m}$  thick struts (113.6 N) is almost four times higher than for the stent with 150  $\mu\text{m}$  thick struts (29.3 N). When a stent is uncrimped to a target diameter of 8 mm the radial force for the stent with 220 mm thick struts is 38.8 N (on the unloading plateau), compared to 10.7N for the stent with 150  $\mu\text{m}$  thick struts. In the case of both stent designs, the radial force range along the uncrimping/unloading plateau is an order of magnitude lower than the computed radial

forces required achieve a full restoration of the lumen area for a stenotic vessel (Figure 5.4).

### 5.3.3 Stenting simulations

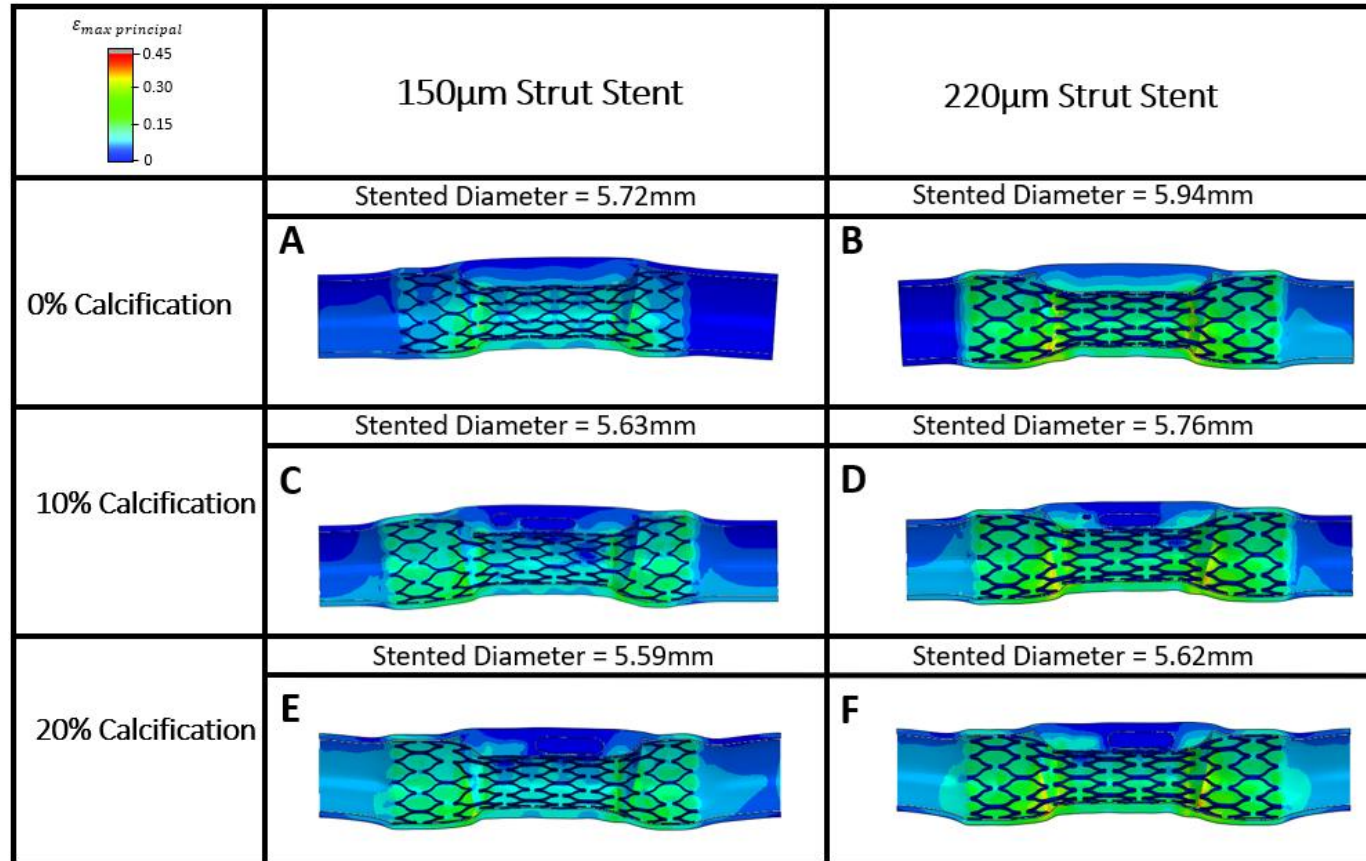


Figure 5.7. Maximum principal strain distribution during nitinol stenting in eccentric plaque models with varying calcification volume. The lumen again acquired in each of the stenting simulations are listed above the corresponding simulations.

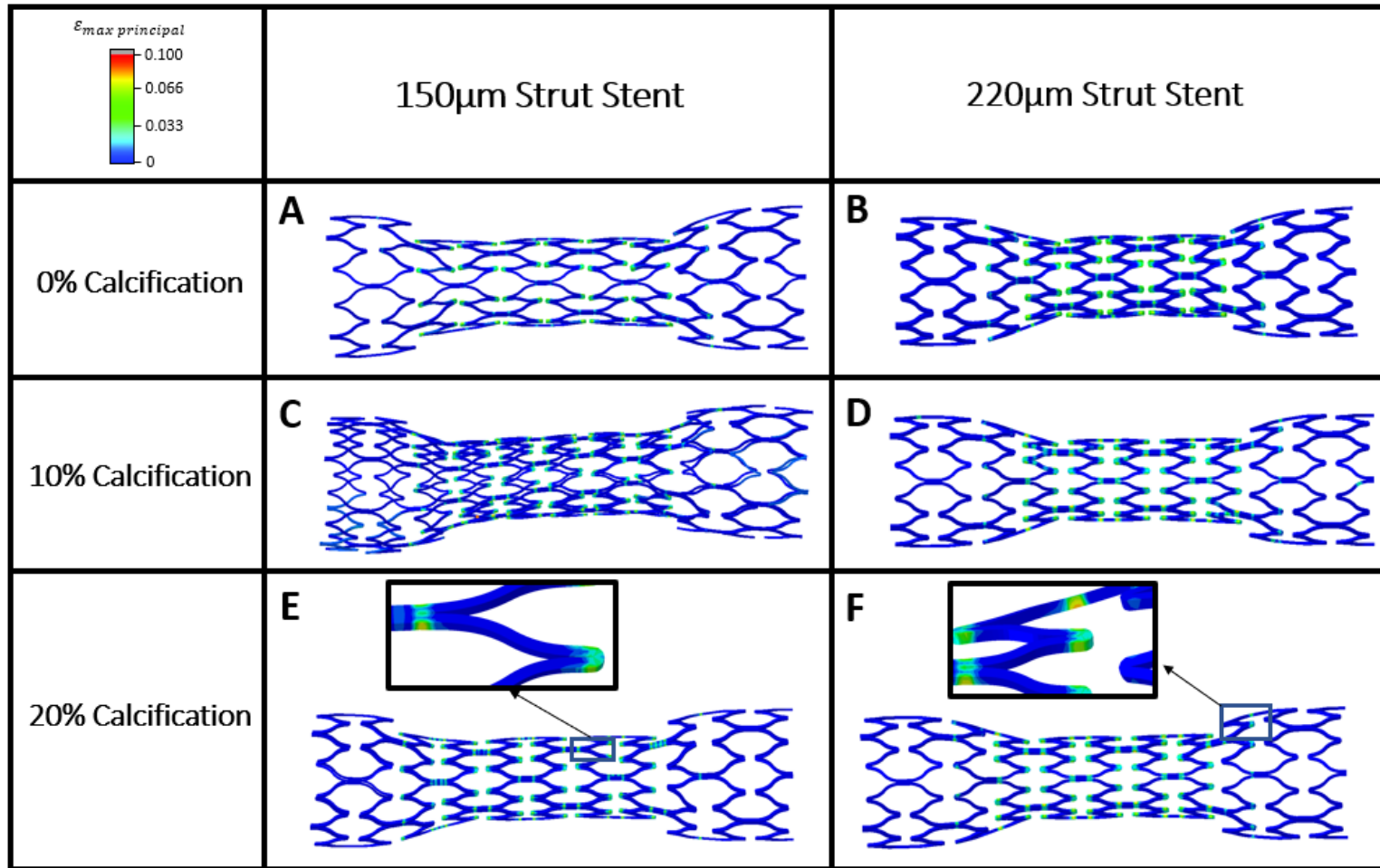


Figure 5.8. Maximum principal strain distribution during nitinol stenting in eccentric plaque models with varying calcification of volumes and orientations. Areas of highest strain on the stent are highlighted in E and F.

Figure 5.7 shows the deformed plaque/vessel following stent deployment for each plaque configuration and each stent design. The distribution of maximum principal stress in the plaque and vessel wall is also shown. The lumen diameter of an unblocked vessel is 8 mm. The stented lumen diameter is approximated by averaging two measurements of the diameter in the centre of the plaque. Figure 5.7(A) shows that the 150  $\mu\text{m}$  struts design achieves a stented lumen diameter of 5.72 mm. Figure 5.7(B) shows that the 220  $\mu\text{m}$  struts design achieves a stented lumen diameter of 5.94 mm. Figure 5.7(C) shows that the 150  $\mu\text{m}$  achieves a stented lumen diameter of 5.63 mm. Figure 5.7(D) shows that the 220  $\mu\text{m}$  achieves a stented lumen diameter of 5.76 mm. Figure 5.7(E) shows that the 150  $\mu\text{m}$  achieves a stented lumen diameter of 5.59 mm. Figure 5.7(F) shows that the 220  $\mu\text{m}$  achieves a stented lumen diameter of 5.62 mm. In all cases, full patency is not achieved. This demonstrates that the outward radial force generated by the stents during uncrimping is not sufficient to fully open any of the stenosed artery configurations shown in Figure 5.7. Consistent with the prediction that the 220 mm strut design provides a higher lumen gain than the 150 mm design, it also generates higher maximum principal strains in the plaque and vessel wall. The deployed stent takes up a dog-bone shape in the case of all plaque configurations considered in this study (Figure 5.8), with a higher equilibrium stent radius being predicted both distal and proximal to the plaque. Furthermore, the largest computed strains occur in the vessel wall distal and proximal to the plaque, in all cases. This is most pronounced for the 220  $\mu\text{m}$  strut design (Figure 5.7(B, D, and F)). The sections of artery that are directly contacted by the stents are opened beyond the unblocked diameter of 8 mm, with circumferential strains in the range from 10% to 15% for the 150  $\mu\text{m}$  strut design (Figure 5.7(A, C, and E)) and from 15% to 20% for the 220  $\mu\text{m}$  strut design (Figure 5.7(B, D, and F)). The highest strains in the stents listed in **Error!**



**Not a valid bookmark self-reference.** are observed in the connecting struts and peaks as shown in Figure 5.8 and highlighted in Figure 5.8(E and F). The maximum principal strains are largest along the plaque surface and are lower distal and proximal to the plaque since the stent has expanded more.

Table 5.4. Largest maximum principal strain in stents deployed in eccentric plaque models with varying calcification volume. The maximum principal strain located in the two distal crowns in the stent in each of the stenting simulations.

Stenting Simulation		Max Principal Strain (Entire Stent)	Max Principal Strain (Stent Ends)
150 $\mu$ m Stent Design	0% Calcification (A)	0.072	0.043
	10% Calcification (C)	0.082	0.017
	20% Calcification (E)	0.076	0.011
220 $\mu$ m Stent Design	0% Calcification (B)	0.072	0.008
	10% Calcification (D)	0.081	0.042
	20% Calcification (F)	0.082	0.007

## 5.4 Discussion

The effects of calcification on stenting and balloon angioplasty have been investigated. Balloon expansion into stenosed arteries with various calcification content and geometries and the resultant balloon lumen pressure is reported. Balloon pressure to achieve full patency higher with increasing calcification volume (E0 – 0.9 MPa, E10 – 1.1 MPa, E20 – 1.9 MPa). During angioplasty the inclusion of circumferentially

aligned calcifications results in a higher balloon pressure (18.04 MPa) in comparison to longitudinally aligned calcifications (2.92 MPa). High strains are observed in fibrous tissue in series with calcification in the circumferential direction and in the thinnest section of fibrous tissue. Eccentric plaque models with varying calcification content are stented using two stents of different strut thicknesses. Stenting resulted in insufficient lumen gain in all stenting simulations. The highest maximum principal strains (0.072 – 0.081) are presented at the connecting struts at the distal and proximal end of the stenosis.

During balloon angioplasty, or following stent deployment, higher strains in the fibrous tissue are computed for higher volume fractions of calcifications in the plaque. Higher strains are also computed in the fibrous tissue when calcifications are circumferentially orientated. The results of this study reveal that elevated localised strains are predicted in fibrous tissue that are in series with stiff calcified particles in the circumferential direction. Such elevated fibrous tissue strains may increase the risk of plaque rupture during stent/balloon angioplasty. The largest strain in eccentric plaques undergoing radial loading is present in the thinnest fibrous section, this has been previously reported in other computational studies (Gu et al., 2010; Iannaccone et al., 2014). As can be seen from the rupture data reported in Appendix 4B, the range of nominal rupture strains (0.14 - 0.57) is mostly less than the predicted strains in the angioplasty models. At lumen gain of 1 the range from strains computed were 0.55 – 0.66, suggesting a high risk of rupture at the thinnest section of the plaque during angioplasty.

The trends between finite models are in agreement with predictions that could be made using analytical pressure vessel theory. However standard thick-walled pressure theory uses the assumption that the materials are linear elastic in nature although as

shown in Chapter 4, plaque constituent materials are non-linear in behaviour and thus the finite element approach is more suitable as a predictive tool for the modelled scenarios.

Previous studies that have investigated various plaque component geometries have reported some macrocalcifications stabilising for the plaque during pressurisation (Buffinton and Ebenstein, 2014; Wong et al., 2012), also some clinical studies have suggested calcifications stabilise plaques (Kwee, 2010; Shaalan et al., 2004). Stability of plaques is not clearly defined in the literature and is generally assumed to be linked to the risk of rupture under loading. The result of this study demonstrated in all cases the presence of macrocalcifications increased rupture risk during angioplasty. As a balloon is inflated, the strains in the fibrous tissue will be greater in the more calcified plaques in comparison to plaques without calcification.

The radial force during uncrimping of the 220  $\mu\text{m}$  stent design is 3 – 4 fold higher than the 150  $\mu\text{m}$  stent design. The 220  $\mu\text{m}$  stent design simulations resulted in greater lumen gain than the 150  $\mu\text{m}$  stent design which aligns with the radial force results, suggesting for plaques with calcification content, a stent with a thicker stent strut may be required during stenting to achieve greater patency. Higher calcification volume requires higher radial force to achieve full restoration of the lumen area. Reduction in lumen gain with increasing calcification volume has been previously reported (Conway et al., 2014; García et al., 2012; Pericevic et al., 2009). In the cases presented in this study 220  $\mu\text{m}$  stent design appears to more favourable results as an increase ranging between 0.5% - 3.8% greater lumen gain the plaque models.

In this study, maximum principal strains of 7.2 – 8.2% are computed in stent struts after uncrimping of the stent into stenosed arteries. An experimental investigation of the fatigue behaviour of nitinol (Pelton et al. (2008)) reports that the maximum strain

amplitude permissible for an infinite fatigue life is dependent on the mean strain applied to the material during fatigue loading. Stenting models predict a mean strain in the stent following deployment between 7% and 8%, depending on the plaque configuration and stent strut thickness. This suggests that the maximum strain amplitudes should not be higher than  $\sim 0.4\%$  following deployment. An alteration of the stent design to achieve lower mean strains (higher deployed radius) would increase the fatigue factor of safety.

The computed pressure required (180.4 atm) to achieve full expansion of the E20C plaque configuration significantly higher than typical angioplasty balloons. Femoral angioplasty balloons has been cited to have rated burst pressures of  $17.7 \pm 4.1$  atm (Nakao et al., 2019). This suggests that angioplasty may not achieve sufficient lumen gain during stenting. However it is possible the implementation of damage may be required to more realistically simulate the stress-state during stent deployment. It has been shown in computational studies that the inclusion of plasticity leads to much more realistic representations of plaque deformation in stenting (Conway et al., 2017b, 2014). It is likely that plaque exhibits some damage or permanent deformation during angioplasty and stenting. Constitutive laws similar to the formulation proposed in Maher et al. (2012) may be required to calculate more physically representative damage in the tissue especially in cases of large stenosis ( $<80\%$ ) dilation.

The clinical implications of this study are the calcification volume and the orientation of the calcified particles are important factors in the success of balloon angioplasty and stenting. Previous studies have shown that calcification, distance to the lumen, lipid pool size, calcifications at shoulder of eccentric plaques all effect the rupture risk (Cardoso and Weinbaum, 2014; Pei et al., 2013; Wenk et al., 2010). The resolution of clinical computed tomography (CT) imaging is voxels  $0.4 \text{ mm}^3$  (Saremi and

Achenbach, 2015), high resolution magnetic resonance imaging (MRI) has pixel resolution of  $0.25 \text{ mm}^3$  (Van Wijk et al., 2015), and IVUS has resolution of  $0.1 - 0.2 \text{ mm}$  (Sharma et al., 2017). These resolutions are sufficient to identify these geometric structures in the stenosis/vessel prior to clinical intervention.

In summary, the current study demonstrates the effects of the calcification volume and geometry in stenting and balloon angioplasty. The results suggest that finite element models of plaque should include explicit representations of calcified particles. This study reinforces the importance of adapting treatment approaches and stent design based on variable plaque constituent geometries between patients.

## 5.5 References

- Cardoso, L., Weinbaum, S., 2014. Changing views of the biomechanics of vulnerable plaque rupture: A review. *Ann. Biomed. Eng.* 42, 415–431. <https://doi.org/10.1007/s10439-013-0855-x>
- Cilla, M., Peña, E., Martínez, M.A., 2012. 3D computational parametric analysis of eccentric atheroma plaque: Influence of axial and circumferential residual stresses. *Biomech. Model. Mechanobiol.* 11, 1001–1013. <https://doi.org/10.1007/s10237-011-0369-0>
- Conway, C., McGarry, J.P., Edelman, E.R., McHugh, P.E., 2017a. Numerical Simulation of Stent Angioplasty with Predilation: an Investigation into Lesion Constitutive Representation and Calcification Influence. *Ann. Biomed. Eng.* 45, 2244–2252. <https://doi.org/10.1007/s10439-017-1851-3>. Numerical
- Conway, C., McGarry, J.P., Edelman, E.R., McHugh, P.E., 2017b. Numerical Simulation of Stent Angioplasty with Predilation: An Investigation into Lesion Constitutive Representation and Calcification Influence. *Ann. Biomed. Eng.* 45, 2244–2252. <https://doi.org/10.1007/s10439-017-1851-3>
- Conway, C., McGarry, J.P., McHugh, P.E., 2014. Modelling of Atherosclerotic Plaque for Use in a Computational Test-Bed for Stent Angioplasty. *Ann. Biomed. Eng.* 42, 2425–2439. <https://doi.org/10.1007/s10439-014-1107-4>
- Conway, C., Sharif, F., McGarry, J.P., McHugh, P.E., 2012. A Computational Test-Bed to Assess Coronary Stent Implantation Mechanics Using a Population-Specific Approach. *Cardiovasc. Eng. Technol.* 3, 374–387. <https://doi.org/10.1007/s13239-012-0104-8>
- Cunnane, E.M., Mulvihill, J.J.E., Barrett, H.E., Healy, D.A., Kavanagh, E.G., Walsh, S.R., Walsh, M.T., 2015. Mechanical, biological and structural characterization of human atherosclerotic femoral plaque tissue. *Acta Biomater.* 11, 295–303. <https://doi.org/10.1016/j.actbio.2014.09.024>
- Fan, Z.M., Liu, X., Du, C.F., Sun, A.Q., Zhang, N., Fan, Z.M., Fan, Y.B., Deng, X.Y., 2016. Plaque components affect wall stress in stented human carotid artery: A numerical study. *Acta Mech. Sin. Xuebao* 32, 1149–1154. <https://doi.org/10.1007/s10409-016-0572-4>
- García, A., Peña, E., Martínez, M.A., 2012. Influence of geometrical parameters on radial force during self-expanding stent deployment. Application for a variable radial stiffness stent. *J. Mech. Behav. Biomed. Mater.* 10, 166–175. <https://doi.org/10.1016/j.jmbbm.2012.02.006>
- Gökgöl, C., Diehm, N., Büchler, P., 2017. Numerical Modeling of Nitinol Stent Oversizing in Arteries with Clinically Relevant Levels of Peripheral Arterial Disease: The Influence of Plaque Type on the Outcomes of Endovascular Therapy. *Ann. Biomed. Eng.* 45, 1420–1433. <https://doi.org/10.1007/s10439-017-1803-y>

GORE, 2014. Instructions for Use GORE VIABHAN. Read 1–86.

Gu, L., Zhao, S., Muttyam, A.K., Hammel, J.M., 2010. The Relation Between the Arterial Stress and Restenosis Rate After Coronary Stenting. *J. Med. Device.* 4, 031005. <https://doi.org/10.1115/1.4002238>

Iannaccone, F., Debusschere, N., De Bock, S., De Beule, M., Van Loo, D., Vermassen, F., Segers, P., Verheghe, B., 2014. The influence of vascular anatomy on carotid artery stenting: A parametric study for damage assessment. *J. Biomech.* 47, 890–898. <https://doi.org/10.1016/j.jbiomech.2014.01.008>

iDataResearch, 2018. Over 1.8 Million Stents Implanted per Year in the U.S. - iData Research [WWW Document]. URL <https://idataresearch.com/over-1-8-million-stents-implanted-per-year-in-the-u-s/> (accessed 10.20.19).

Irina, P.I., Carmen, C., Petru, B., 2019. Common Femoral Artery Diameters Determined by Doppler Ultrasonography. *ARS Medica Tomitana* 25, 1–5. <https://doi.org/10.2478/arism-2019-0001>

Karimi, A., Navidbakhsh, M., Faghihi, S., 2014. A comparative study on plaque vulnerability using constitutive equations. *Perfus. (United Kingdom)* 29, 178–183. <https://doi.org/10.1177/0267659113502835>

Karimi, A., Navidbakhsh, M., Yamada, H., Razaghi, R., 2014. A nonlinear finite element simulation of balloon expandable stent for assessment of plaque vulnerability inside a stenotic artery. *Med. Biol. Eng. Comput.* 52, 589–599. <https://doi.org/10.1007/s11517-014-1163-9>

Kelly-Arnold, A., Maldonado, N., Laudier, D., Aikawa, E., Cardoso, L., Weinbaum, S., 2013. Revised microcalcification hypothesis for fibrous cap rupture in human coronary arteries. *Proc. Natl. Acad. Sci.* 110, 10741–10746. <https://doi.org/10.1073/pnas.1308814110>

Kwee, R.M., 2010. Systematic review on the association between calcification in carotid plaques and clinical ischemic symptoms. *J. Vasc. Surg.* 51, 1015–1025. <https://doi.org/10.1016/j.jvs.2009.08.072>

Liang, W., 2016. Stent design: Factors influencing radial force and flexibility.

Loree, H.M., Grodzinsky, A.J., Park, S.Y., Gibson, L.J., Lee, R.T., 1994. Static circumferential tangential modulus of human atherosclerotic tissue. *J. Biomech.* 27, 195–204. [https://doi.org/10.1016/0021-9290\(94\)90209-7](https://doi.org/10.1016/0021-9290(94)90209-7)

Maher, E., Creane, A., Lally, C., Kelly, D.J., 2012. An anisotropic inelastic constitutive model to describe stress softening and permanent deformation in arterial tissue. *J. Mech. Behav. Biomed. Mater.* 12, 9–19. <https://doi.org/10.1016/j.jmbbm.2012.03.001>

McGrath, D.J., O'Brien, B., Bruzzi, M., Kelly, N., Clauser, J., Steinseifer, U., McHugh, P.E., 2016. Evaluation of cover effects on bare stent mechanical response.

- J. Mech. Behav. Biomed. Mater. 61, 567–580.  
<https://doi.org/10.1016/j.jmbbm.2016.04.023>
- Merit, n.d. DYNAMIS ΔV 0.035” PTA IFU.
- Migliavacca, F., Petrini, L., Massarotti, P., Schievano, S., Auricchio, F., Dubini, G., 2004. Stainless and shape memory alloy coronary stents: A computational study on the interaction with the vascular wall. *Biomech. Model. Mechanobiol.* 2, 205–217.  
<https://doi.org/10.1007/S10237-004-0039-6>
- Morlacchi, S., Pennati, G., Petrini, L., Dubini, G., Migliavacca, F., 2014. Influence of plaque calcifications on coronary stent fracture: A numerical fatigue life analysis including cardiac wall movement. *J. Biomech.* 47, 899–907.  
<https://doi.org/10.1016/j.jbiomech.2014.01.007>
- Nakao, M., Yamaguchi, J., Otsuki, H., Arashi, H., Hagiwara, N., 2019. Clinical outcomes of high-pressure balloon angioplasty for common femoral artery disease in contemporary practice. *Cardiovasc. Interv. Ther.* 34, 340–344.  
<https://doi.org/10.1007/s12928-018-0557-2>
- Peach, G., Griffin, M., Jones, K.G., Thompson, M.M., Hinchliffe, R.J., 2012. Diagnosis and management of peripheral arterial disease. *BMJ* 345.  
<https://doi.org/10.1136/bmj.e5208>
- Pei, X., Wu, B., Li, Z.-Y., 2013. Fatigue Crack Propagation Analysis of Plaque Rupture. *J. Biomech. Eng.* 135, 101003. <https://doi.org/10.1115/1.4025106>
- Pelton, A.R., Schroeder, V., Mitchell, M.R., Gong, X.Y., Barney, M., Robertson, S.W., 2008. Fatigue and durability of Nitinol stents. *J. Mech. Behav. Biomed. Mater.* 1, 153–164. <https://doi.org/10.1016/j.jmbbm.2007.08.001>
- Pericevic, I., Lally, C., Toner, D., Kelly, D.J., 2009. The influence of plaque composition on underlying arterial wall stress during stent expansion: The case for lesion-specific stents. *Med. Eng. Phys.* 31, 428–433.  
<https://doi.org/10.1016/j.medengphy.2008.11.005>
- Saremi, F., Achenbach, S., 2015. Coronary plaque characterization using CT. *Am. J. Roentgenol.* 204, W249–W260. <https://doi.org/10.2214/AJR.14.13760>
- Shalan, W.E., Cheng, H., Gewertz, B., McKinsey, J.F., Schwartz, L.B., Katz, D., Cao, D., Desai, T., Glagov, S., Bassiouny, H.S., 2004. Degree of carotid plaque calcification in relation to symptomatic outcome and plaque inflammation. *J. Vasc. Surg.* 40, 262–269. <https://doi.org/10.1016/j.jvs.2004.04.025>
- Sharma, S.K., Vengrenyuk, Y., Kini, A.S., 2017. IVUS, OCT, and Coronary Artery Calcification: Is There a Bone of Contention? *JACC Cardiovasc. Imaging* 10, 880–882. <https://doi.org/10.1016/j.jcmg.2017.06.008>
- Sokolis, D.P., 2010. A passive strain-energy function for elastic and muscular arteries: correlation of material parameters with histological data. *Med. Biol. Eng. Comput.* 48, 507–518. <https://doi.org/10.1007/s11517-010-0598-x>



Steinman, D.A., Poepping, T.L., Tambasco, M., Rankin, R.N., Holdsworth, D.W., 2000. Flow patterns at the stenosed carotid bifurcation: Effect of concentric versus eccentric stenosis. *Ann. Biomed. Eng.* 28, 415–423. <https://doi.org/10.1114/1.279>

TERUMO, 2016. PTA Balloon Dilatation Catheter [WWW Document]. CROSSTELLA-RX-IFU. URL <http://www.terumo.com/content/dam/terumopublic/products/CROSSTELLA/CROSSTELLA-RX-IFU.pdf>

van den Munckhof, I., Scholten, R., Cable, N.T., Hopman, M.T.E., Green, D.J., Thijssen, D.H.J., 2012. Impact of age and sex on carotid and peripheral arterial wall thickness in humans. *Acta Physiol.* 206, 220–228. <https://doi.org/10.1111/j.1748-1716.2012.02457.x>

Van Wijk, D.F., Strang, A.C., Duivenvoorden, R., Enklaar, D.J.F., Zwinderman, A.H., Van Der Geest, R.J., Kastelein, J.J.P., De Groot, E., Stroes, E.S.G., Nederveen, A.J., 2015. Increasing the spatial resolution of 3T carotid MRI has no beneficial effect for plaque component measurement reproducibility. *PLoS One* 10, 1–15. <https://doi.org/10.1371/journal.pone.0130878>

Wei, L., Chen, Q., Li, Z., 2019. Influences of plaque eccentricity and composition on the stent–plaque–artery interaction during stent implantation. *Biomech. Model. Mechanobiol.* 18, 45–56. <https://doi.org/10.1007/s10237-018-1066-z>

Wenk, J.F., Papadopoulos, P., Zohdi, T.I., 2010. Numerical Modeling of Stress in Stenotic Arteries With Microcalcifications: A Micromechanical Approximation. *J. Biomech. Eng.* 132, 091011. <https://doi.org/10.1115/1.4001351>

Wong, K.K.L., Thavornpattanapong, P., Cheung, S.C.P., Sun, Z., Tu, J., 2012. Effect of calcification on the mechanical stability of plaque based on a three-dimensional carotid bifurcation model. *{BMC} Cardiovasc. Disord.* 12. <https://doi.org/10.1186/1471-2261-12-7>

## Appendix 5A

Below is the ellipsoid creation MATLAB script.

```
clear; close all; close all;

w=0.9; % Thickness at centre
h=0.9; % Height
r1=3; % Inner radius
pointSpacing=0.1;
wrapAnglesDegrees=[15 16 18 16 15];
hLevels=[-h/2 -h/3 0 h/3 h/2];
numSteps=9;
numZSteps=5;

volumeFactor=8;
abaqusInpFileName=fullfile(fileparts(mfilename('fullpath')),'20pcaclf.inp');
%%
wrapAngles=(wrapAnglesDegrees/180)*pi;
zCoordinates=linspace(-h/2,h/2,numZSteps);

X=zeros(numZSteps,numSteps);
Y=zeros(numZSteps,numSteps);
Z=zeros(numZSteps,numSteps);
for q=1:numZSteps
    wrapAngleNow=interp1(hLevels,wrapAngles,zCoordinates(q),'pchip');
    V_now=createMoon(wrapAngleNow,r1,w,numSteps);
    X(q,:)=V_now(:,1)';
    Y(q,:)=V_now(:,2)';
    Z(q,:)=zCoordinates(q);
end

% Create quad patch data
c=(1:1:size(Z,1))';
C=c(:,ones(1,size(Z,2)));
[F,V,C]=surf2patch(X,Y,Z,C);

% Get start and end curves
indStart=1:numZSteps:size(V,1);
indEnd=numZSteps:numZSteps:size(V,1);

% Check if indices are consistent with edges
Eb=patchBoundary(F,V); % Patch edges
e=indStart(1:2);
logicFlip=~any((Eb(:,1)==e(1)) & (Eb(:,2)==e(2)));
if logicFlip
    indStart=flip(indStart);
end
e=indEnd(1:2);
```

```

logicFlip= ~any((Eb(:,1)==e(1)) & (Eb(:,2)==e(2)));
if logicFlip
    indEnd=flip(indEnd);
end

% Close patch if required
[F,V,C]=patchCylSurfClose(X,Y,Z,C);
C=round(C);

%%
% Convert to triangles
% F=[F(:,[1 2 3]); F(:,[3 4 1])];
% F=fliplr(F); % Invert face direction
Vc_end=V(indEnd,:);

logicSlashType= repmat(iseven(C),2,1);

Xi=X;
x=X(1,:);
dx=diff(x)/2;
dx(end+1)=(x(1)-x(end))/2;
for q=2:2:size(X,1)
    X(q,:)=X(q,.)+dx;
end

Yi=Y;
y=Y(1,:);
dy=diff(y)/2;
dy(end+1)=(y(1)-y(end))/2;
for q=2:2:size(Y,1)
    Y(q,:)=Y(q,.)+dy;
end

Zi=Z;
z=Z(1,:);
dz=diff(z)/2;
dz(end+1)=(z(1)-z(end))/2;
for q=2:2:size(Z,1)
    Z(q,:)=Z(q,.)+dz;
end

V=[X(:) Y(:) Z(:)];

% Ensure end curve is unaltered if numSteps is even
if iseven(numSteps)
    V(indEnd,:)=Vc_end;
end

F1=[F(:,1) F(:,3) F(:,2); F(:,1) F(:,4) F(:,3)];
F2=[F(:,1) F(:,4) F(:,2); F(:,2) F(:,4) F(:,3)];

```

```

F=fliplr([F1(~logicSlashType,:);F2(logicSlashType,:)]);

%% Close top and bottom
% Close top
% pointSpacingNow=mean(patchEdgeLengths(F,V));

pointSpacingNow=mean(diff(pathLength(V(indStart,[1 2]))));
[Ft,Vt]=regionTriMesh2D({ V(indStart,[1 2]) },pointSpacingNow,0,0);
Vt(:,3)=mean(V(indStart,3));
Ft=fliplr(Ft); % Invert face direction
% indBoundary=unique(patchBoundary(Ft,Vt));
% Vt_boundary=Vt(indBoundary,:);
Dt=minDist(Vt,V(indStart,:));
Dt=Dt./max(Dt(:));
Vt(:,3)=Vt(:,3)-(w/2).*sin(acos(1-Dt));
% Vt(indBoundary,:)=Vt_boundary;

% Close bottom
pointSpacingNow=mean(diff(pathLength(V(indEnd,[1 2]))));
[Fb,Vb]=regionTriMesh2D({ V(indEnd,[1 2]) },pointSpacingNow,0,0);
Vb(:,3)=mean(V(indEnd,3));
Db=minDist(Vb,V(indEnd,:));
Db=Db./max(Db(:));
Vb(:,3)=Vb(:,3)+(w/2).*sin(acos(1-Db));

%% Join and merge
[F,V,C]=joinElementSets({F,Ft,Fb},{ V,Vt,Vb }); % Append together
[F,V]=mergeVertices(F,V); % Merge shared nodes

%% Smoothen mesh
cPar.Method='HC';
cPar.n=150;
V=patchSmooth(F,V,[],cPar);

cFigure; hold on;
gpatch(F,V,'gw','k',1);
% patchNormPlot(F,V);

% gpatch(Ft,Vt,Dt);
% gpatch(Fb,Vb,'rw');

% patchNormPlot(Ft,Vt);
% patchNormPlot(Fb,Vb);
% plotV(V(indStart,:),'r-','LineWidth',5,'MarkerSize',35);

% plotV(V1,'r-','LineWidth',5,'MarkerSize',35);
% plotV(V2,'b-','LineWidth',5,'MarkerSize',35);
% plotV(Vt1,'g-','LineWidth',5,'MarkerSize',35);

```

```

% plotV(Vt2,'c.-','LineWidth',5,'MarkerSize',35);

% plotV(V,'k.-','LineWidth',5,'MarkerSize',50);
% plot3(X(:),Y(:),Z(:),'r.','LineWidth',5,'MarkerSize',50);
axisGeom;
camlight headlight;
drawnow;

%% Create a tetrahedral mesh

[V_regions]=getInnerPoint(F,V);

% Regional mesh volume parameter
inputStruct.stringOpt='-pq1.2AaY';
inputStruct.Faces=F;
inputStruct.Nodes=V;
inputStruct.holePoints=[];
inputStruct.faceBoundaryMarker=ones(size(F,1),1); %Face boundary markers
inputStruct.regionPoints=V_regions; %region points
inputStruct.regionA=volumeFactor.*tetVolMeanEst(F,V); %Volume for regular tets

% Mesh model using tetrahedral elements using tetGen
[meshOutput]=runTetGen(inputStruct); %Run tetGen

% Access model element and patch data
Fb=meshOutput.facesBoundary;
Cb=meshOutput.boundaryMarker;
V=meshOutput.nodes;
CE=meshOutput.elementMaterialID;
E=meshOutput.elements;

%% Visualizing mesh using |meshView|, see also |anim8|

% meshView(meshOutput);

%% Defining the abaqus input structure
% See also |abaqusStructTemplate| and |abaqusStruct2inp| and the abaqus user
% manual.

%%--> Heading
abaqus_spec.Heading.COMMENT{1}='Job name: ABAQUS inp file creation demo';
abaqus_spec.Heading.COMMENT{2}='Generated by: GIBBON';

%%--> Preprint
abaqus_spec.Preprint.ATTR.echo='NO';
abaqus_spec.Preprint.ATTR.model='NO';
abaqus_spec.Preprint.ATTR.history='NO';
abaqus_spec.Preprint.ATTR.contact='NO';

%%--> Part

```

```

% Node
nodeIds=(1:1:size(V,1));
abaqus_spec.Part.COMMENT='This section defines the part geometry in terms of
nodes and elements';
abaqus_spec.Part.ATTR.name='Calc';
abaqus_spec.Part.Node={nodeIds,V};

% Element
elementIds=(1:1:size(E,1));
abaqus_spec.Part.Element{1}.ATTR.type='C3D4';
abaqus_spec.Part.Element{1}.VAL={elementIds(:),E};

% Element sets
abaqus_spec.Part.Elset{1}.ATTR.elset='Set-1';
abaqus_spec.Part.Elset{1}.VAL=elementIds;

% Sections
abaqus_spec.Part.Solid_section.ATTR.elset='Set-1';
abaqus_spec.Part.Solid_section.ATTR.material='Elastic';

%%--> Assembly
abaqus_spec.Assembly.ATTR.name='Assembly-1';
abaqus_spec.Assembly.Instance.ATTR.name='Calc-assembly';
abaqus_spec.Assembly.Instance.ATTR.part='Calc';
volume=tetVol(E,V);
totalvolume=sum(volume)

abaqusStruct2inp(abaqus_spec,abaqusInpFileName);

function [V]=createMoon(wrapAngle,r1,w,numSteps)

r2=r1+w; % Outer radius

t_mid=linspace(-wrapAngle/2,wrapAngle/2,numSteps);
x1=r1.*cos(t_mid);
y1=r1.*sin(t_mid);
V1=[x1(:) y1(:) zeros(size(x1(:)))];

x2=r2.*cos(t_mid);
y2=r2.*sin(t_mid);
V2=[x2(:) y2(:) zeros(size(x2(:)))];

tt=linspace(0,pi,numSteps);
rt=w/2;
xt=rt.*cos(tt);
yt=rt.*sin(tt);
Vt=[xt(:) yt(:) zeros(size(xt(:)))];

R=euler2DCM([0 0 -wrapAngle/2]);

```

```

Vt1=Vt*R;
Vt1(:,1)=Vt1(:,1)-Vt1(1,1);
Vt1(:,2)=Vt1(:,2)-Vt1(1,2);
Vt1(:,1)=Vt1(:,1)+V2(end,1);
Vt1(:,2)=Vt1(:,2)+V2(end,2);

R=euler2DCM([0 0 pi+wrapAngle/2]);
Vt2=Vt*R;
Vt2(:,1)=Vt2(:,1)-Vt2(1,1);
Vt2(:,2)=Vt2(:,2)-Vt2(1,2);
Vt2(:,1)=Vt2(:,1)+V1(1,1);
Vt2(:,2)=Vt2(:,2)+V1(1,2);

V=[V1(1:end-1,:);flipud(Vt1);flipud(V2(1:end-1,:)); flipud(Vt2(2:end-1,:))];

V=evenlySampleCurve(V,numSteps,'pchip',1);

end

```

# 6 COHESIVE ZONE SIMULATION OF PLAQUE FAILURE DURING BALLOON ANGIOPLASTY

## 6.1 Introduction

Plaque rupture is major cause of myocardial infarction and stroke. Several studies focus on establishing rupture stresses for atherosclerotic plaque using mechanical testing of excised plaques (Cunnane et al., 2015; Lawlor et al., 2011; Mulvihill et al., 2013; Teng et al., 2009). These uniaxial testing studies have typically involved the monotonic stretching of heterogeneous plaque samples to failure and reporting a stress at failure. This approach does not establish the clear contribution of constituents to the rupture stress. This type of testing assesses the strength of the tissue in the circumferential and axial directions. However as seen in a clinical study, atherosclerotic plaques may delaminate from the artery leading to floating plaques (Liu et al., 2017). Also, it has been hypothesized the presence of micro-calcifications in the fibrous cap increase the risk of rupture. Computational studies of calcification



in the fibrous cap have shown stress increases in locations with both large calcifications (Bluestein et al., 2008; Wenk et al., 2010) and micro-calcifications (Bluestein et al., 2008; Hutcheson et al., 2014; Kelly-Arnold et al., 2013; Rambhia et al., 2012; Vengrenyuk et al., 2012). An interface strength for the calcification-fibrous interface has not been established.

The mechanisms of plaque rupture during angioplasty must be uncovered in order to reliably assess the performance and safety of angioplasty devices. Previous computational models have simulated crack growth using fracture modelling techniques similar to the extended finite element method (Ferrara and Pandolfi, 2008; Gasser and Holzapfel, 2007; Pei et al., 2013; Versluis et al., 2006). Additionally, some plaque rupture studies have applied cohesive based models at plaque constituent or layer interfaces in finite element simulations (Leng et al., 2016, 2015a, 2015b; Merei et al., 2017; Wang et al., 2014). None of these previous studies have investigated the effect of calcified particles on plaque rupture and fracture.

Cutting angioplasty balloons are designed to create a crack using mounted blades and induce tearing in difficult stenoses. Cutting balloons have been shown to induce less restenosis in comparison to traditional percutaneous transluminal angioplasty balloons (Kasirajan et al., 2004). The principal on which these devices work is that the cuts made in the wall of the plaque are controlled and will induce lower strains that will not damage the smooth muscle cells. With reduced damage to the smooth muscle cells, it is expected that restenosis rates will reduce. To the authors knowledge, cutting balloons have not been previously analysed using computational simulation.

Section 6.2.1 outlines uniaxial testing of a calcified fibrous atherosclerotic plaque sample to rupture in order to calibrate the cohesive strength of the calcification-fibrous

interface. Section 6.2.2 explores the effect of calcifications on rupture. Section 6.2.3 presents a computational analysis of plaque damage induced by cutting balloons.

## 6.2 Methodology

### 6.2.1 Rupture experiment and inverse finite element modelling

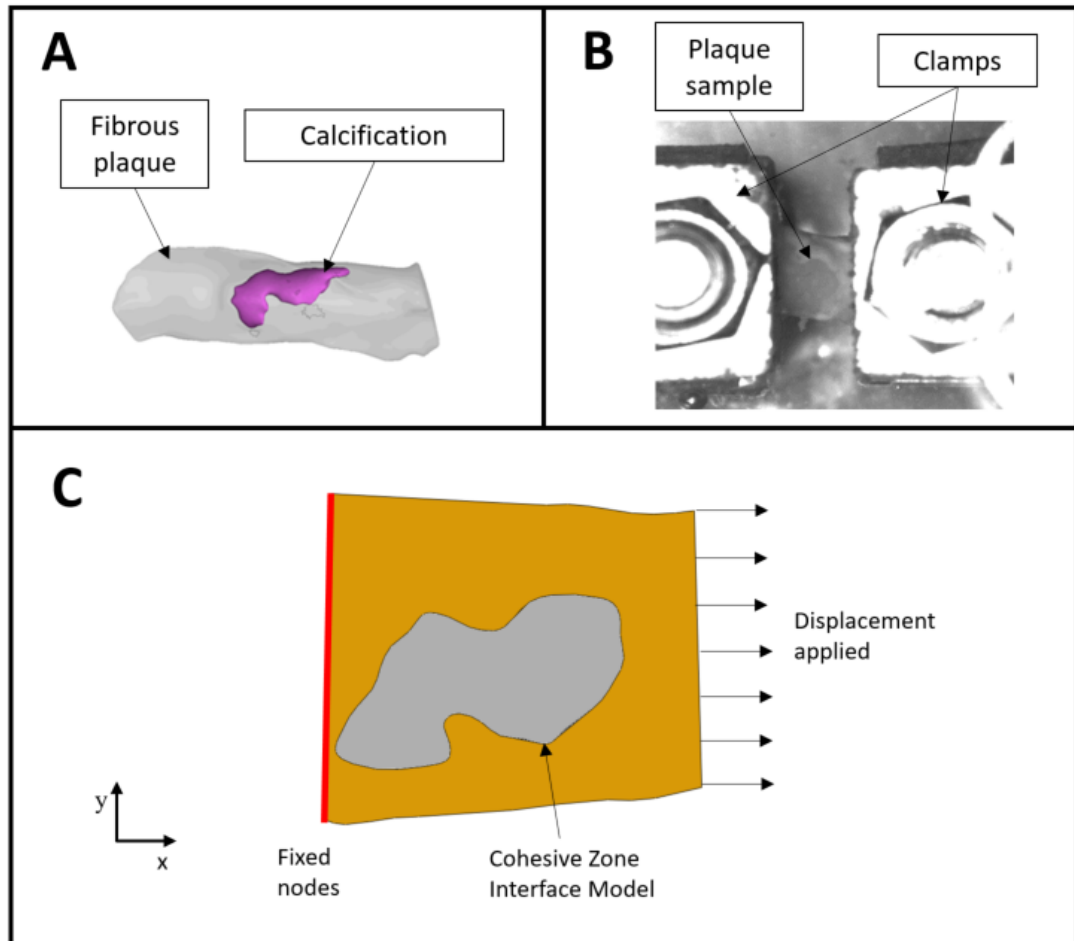


Figure 6.1. (A)  $\mu$ CT scanning of carotid plaque sample with embedded calcification in the matrix material. (B) Experimental testing the composite plaque sample to failure. (C) Model with cohesive zone model describing the plaque calcification-fibrous interface.

Heterogeneous samples are isolated using the same method to isolate homogeneous samples described in Chapter 4. Composite (containing calcifications and fibrous

tissue) atherosclerotic plaque samples were uniaxial stretched in a water bath at a strain rate of 7.5% strain per minute. From this testing 1 sample is observed to have ruptured along the plaque-calcification interface. This composite plaque sample is scanned and reconstructed (Figure 6.1(A)) using a  $\mu$ CT (micro-computed tomography) scanner with the same parameters outlined in Chapter 4. The sample is then uniaxially stretched until rupture (Figure 6.1(B)). A finite element simulation of the test is performed using a model consisting of 7247 generalized plane strain elements, as shown in Figure 6.1(C). The plaque and calcification material laws implemented are the calibrated hyperelastic properties for the constituents reported in Chapter 4. As shown in Figure 6.1(C), in order to simulate the experimental test, the left edge of the model is fixed in the x- and y-direction, while the right edge is fixed in the y-direction, with a displacement of 3 mm applied in the x-direction. A cohesive zone model (CZM) is implemented at the calcification-fibrous tissue interface. A bilinear uncoupled mixed-mode fracture criterion is implemented to describe the damage initiation (Abaqus Theory Manual, DS SIMULIA, USA). The traction stress vector  $\mathbf{t}$  is given by:

$$\mathbf{t} = \begin{Bmatrix} t_n \\ t_t \end{Bmatrix} = \begin{bmatrix} K_{nn} & 0 \\ 0 & K_{tt} \end{bmatrix} \begin{Bmatrix} \delta_n \\ \delta_t \end{Bmatrix} = K\delta \quad (6-1)$$

Where it consists of the traction in the normal and shear directions,  $t_n$  and  $t_t$  respectively. The corresponding separations are denoted by  $\delta_n$  and  $\delta_t$ .  $K_{nn}$  and  $K_{tt}$  describes the stiffness in the normal and shear directions. A maximum stress criterion is used for damage initiation and is represented by:

$$\max \left\{ \frac{\langle t_n \rangle}{T_n^o}, \frac{t_t}{T_t^o} \right\} = 1 \quad (6-2)$$

Where the  $T_n^o$  is the peak value for tensile contact stress (as denoted by the Macaulay brackets since compression cannot initiate delamination) and  $T_t^o$  is the peak shear contact stress. The effective separation is given by the expression:

$$\delta_m = \sqrt{\langle \delta_n \rangle^2 + \delta_s^2} \quad (6-3)$$

The effective separation at damage initiation  $\delta_m^f$  is defined as:

$$\delta_m^f = \frac{2G^C}{T_{eff}^o} \quad (6-4)$$

Where  $G^C$  is the critical failure energy and  $T_{eff}^o$  is the traction at damage initiation.

Damage parameter  $D$  for linear softening is described as:

$$D = \frac{\delta_m^f(\delta_m^{max} - \delta_m^o)}{\delta_m^{max}(\delta_m^f - \delta_m^o)} \quad (6-5)$$

Where  $\delta_m^{max}$  is the maximum value of the effective separation attained during the loading history and  $\delta_m^o$  is the effective separation at damage initiation. The damage evolution law is given as:

$$t_n = \begin{cases} (1-D)\bar{t}_n, & \bar{t}_n \geq 0 \\ \bar{t}_n, & otherwise \end{cases} \quad (6-6)$$

$$t_t = (1-D)\bar{t}_t$$

Where  $\bar{t}_n$  and  $\bar{t}_t$  are the contact stress components predicted by the elastic traction-separation behaviour for the current separation without damage. The relationship between normal and shear fracture energy are given as:

$$G^C = (G_t^C - G_n^C) \left\{ \frac{G_S}{G_T} \right\}^\eta + G_n^C \quad (6-7)$$

where  $G_S$  and  $G_T$  is the shear and total energy release rates respectively;  $G_n$  and  $G_t$  are the normal, first and second shear energy release rate;  $G_n^C$  and  $G_t^C$  normal and shear critical fracture energy (Benzeggagh and Kenane, 1996)

Based on the studies of Wang et al. (2011) and Leng et al. (2015b), the following model parameters are assumed:  $G_n = 0.019$  N/mm;  $G_t = 0.019$  N/mm;  $K = 10000$  MPa/mm; and  $\eta = 1.2$ . The parameters for  $T_n^0$  and  $T_s^0$  are calibrated so that the computed force at rupture is equal to the experimentally measured force at rupture. The assumption is made that the normal and shear peak tractions are equal ( $T_n^0 = T_t^0$ ).

### 6.2.2 2D angioplasty damage models

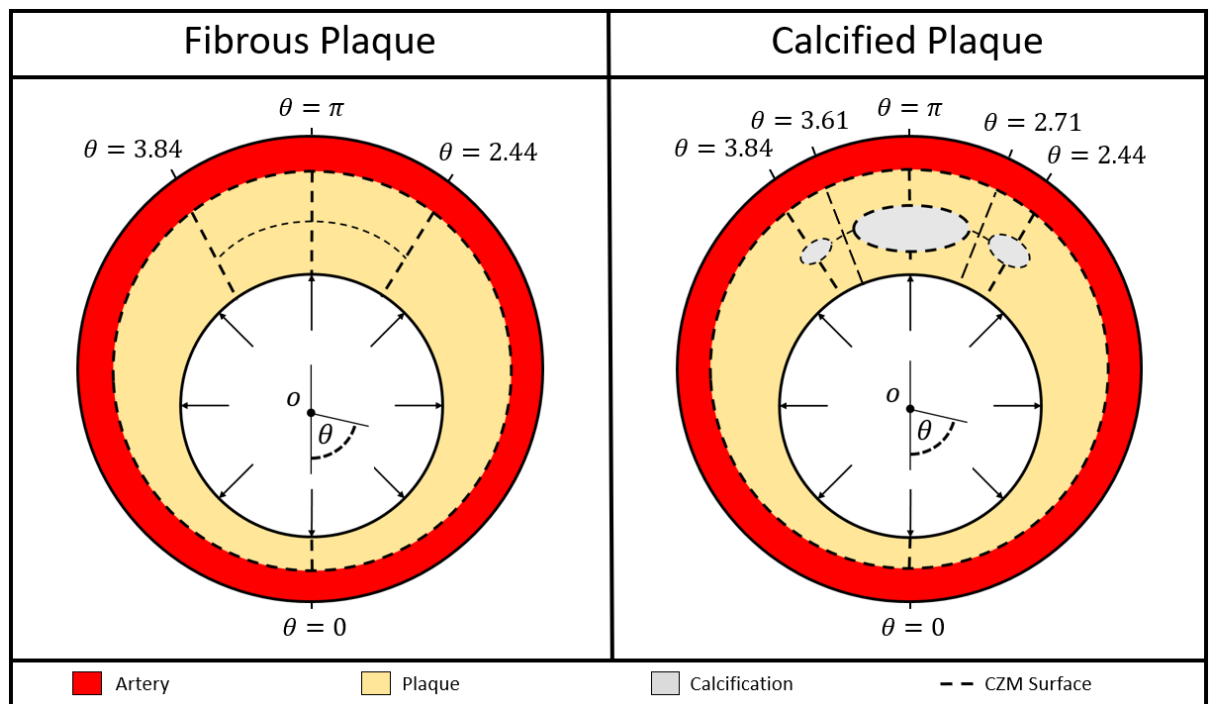


Figure 6.2. Schematic of 2D atherosclerotic plaque models: Left – (uncalcified) fibrous plaque; Right – calcified plaque. CZM surfaces at which the cohesive zone model is implemented as illustrated. The circumferential coordinate  $\theta$  (radians) is used to describe the location of CZM surfaces and calcifications. CZM surfaces within

the fibrous tissue are positioned at  $\theta = 0$ ,  $\theta = 2.44$ ,  $\theta = 2.71$ ,  $\theta = \pi$ ,  $\theta = 3.61$  and  $\theta = 3.84$ . Calcifications are positioned with centroids are  $\theta = 2.44$  and  $\theta = 3.84$ . A CZM surface is also positioned at the interface between the plaque and the vessel wall.

Two eccentric plaque configurations are constructed, as shown in Figure 6.2. Firstly, a fibrous plaque without any calcifications is modelled. The fibrous plaque model is created with the same diameters and eccentricity as the fibrous plaque models described previously in Chapter 5. Additionally, a composite plaque in which three elliptical calcified particles are embedded in the fibrous matrix is modelled. The total volume of the three calcified particles comprises of 20% of the total plaque volume. The ratio of the volume of the three particles (0.535:0.231:0.101) is based on the measured volume ratios of the 3 largest calcifications from the CT analysis presented in Chapter 4. The ratio of the major-axis to the minor-axis of the elliptical calcifications (1.65, 1.83, and 1.89 in order of size) is also based on analysis of the CT data presented in Chapter 4. Surfaces at which the cohesive zone model is implemented are illustrated. The circumferential coordinate  $\theta$  (radians) is used to describe the location of CZM surfaces and calcifications. CZM surfaces within the fibrous tissue are positioned at  $\theta = 0$ ,  $\theta = 2.44$ ,  $\theta = 2.71$ ,  $\theta = \pi$ ,  $\theta = 3.61$  and  $\theta = 3.84$ . Calcifications are positioned with centroids at  $\theta = 2.44$ ,  $\theta = \pi$  and  $\theta = 3.84$ , all on an arc of 3.4 mm from the centre point of the lumen. A CZM surface is also positioned at the interface between the plaque and the vessel wall. In the case of the calcified plaque, CZM surfaces are also positioned at the calcification-fibrous tissue interfaces.

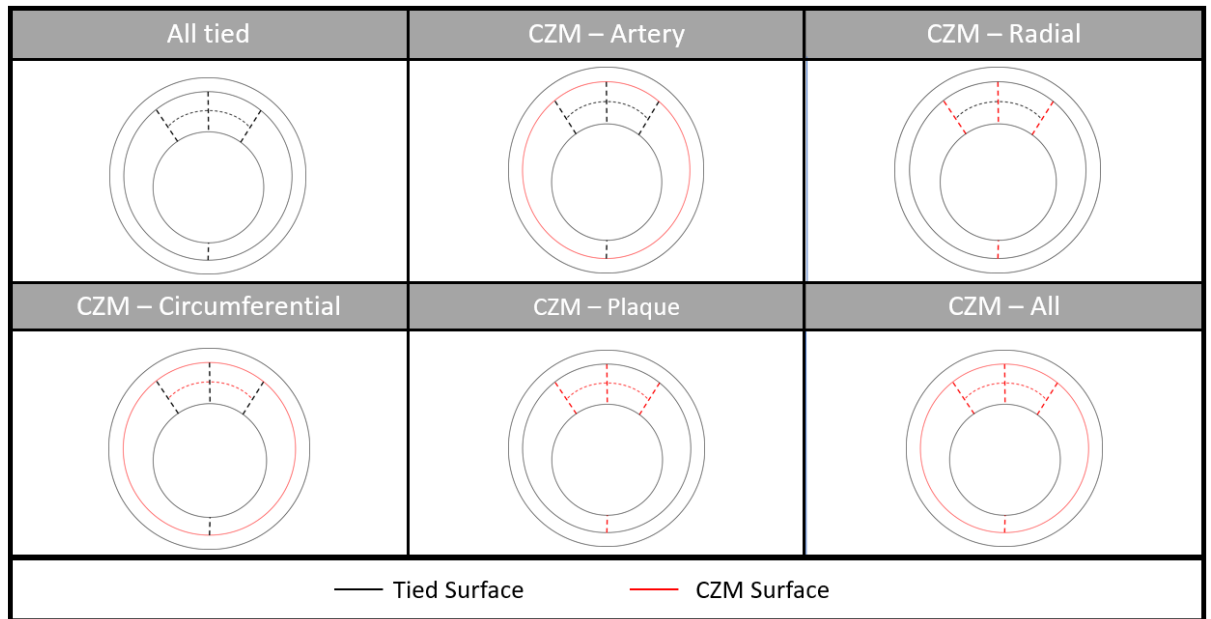


Figure 6.3. Schematic diagrams of simulated combinations of tied surfaces and CZM surfaces for non-calcified plaques.

Parametric analyses are performed in which different combinations of CZM surfaces are activated in order to assess the dominant modes of plaque failure during angioplasty, as shown in Figure 6.3 (fibrous plaque) and Figure 6.4 (calcified plaque). Such simulations range from “All tied” in which no CZM surfaces are activated and no plaque rupture is simulated, to “CZM-All” in which all cohesive zone CZM surfaces are activated and the relative risk of intra-fibrous tissue rupture, calcification-fibrous tissue interface fracture and artery-fibrous tissue fracture are assessed

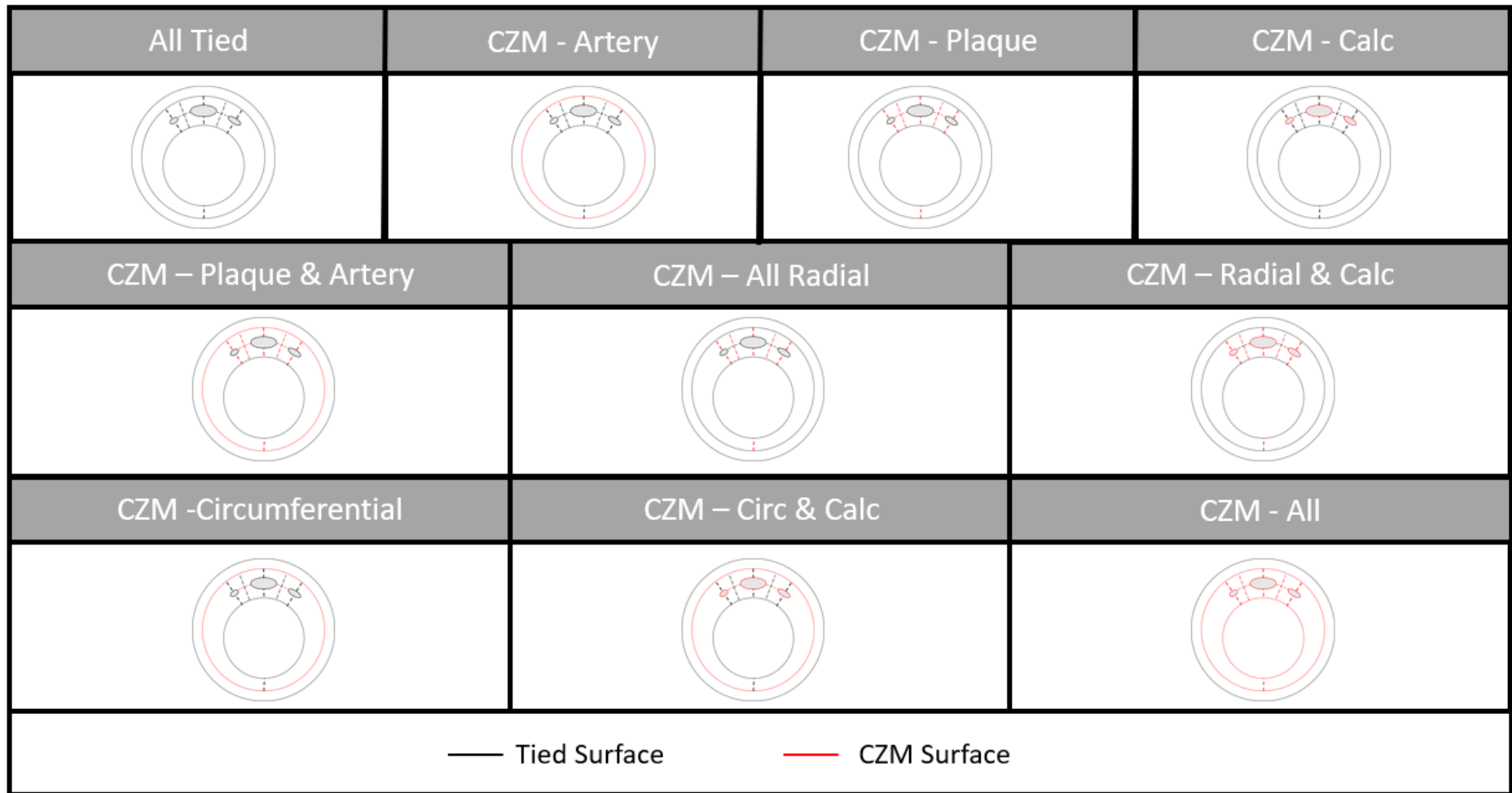


Figure 6.4. Schematic diagrams of simulated combinations of tied surfaces and CZM surfaces for calcified plaques.



All models are loaded by increasing the lumen pressure up to a maximum value of 1.5 MPa, or until extensive crack propagation is predicted. 1.5 MPa was chosen to investigate the loading conditions which would occur during balloon angioplasty. 4970 of CPE4R elements are used to mesh the plaque and vessel wall in the fibrous plaque models and 5716 of CPE4R elements are used to mesh the plaque, calcifications and vessel wall in the calcified plaque models. Again, hyper-viscoelastic material models developed and calibrated in Chapter 4 are used for the plaque fibrous tissue and calcified particles. Regarding the cohesive zone models, it is assumed that the normal and shear interface strengths are equal ( $T_n^0 = T_t^0$ ). Different values of interface strength are used at each CZM surface type. A plaque-artery interface strength of 0.14 MPa is assumed based on peel testing of murine atherosclerotic plaques by Leng et al. (2015b). The interface strength for intra-plaque fracture is assumed to be 0.3 MPa based on previously reported rupture stress of fibrous tissue (Cheng et al., 1993; Leng et al., 2016)). The calcification-fibrous tissue interface strength is calibrated using the simulations described in Section 6.2.1 above. Additionally, one model of the fibrous and calcified geometries with all CZM boundaries active were prescribed the calibrated calcification-fibrous strength.

## 6.2.3 Cutting balloon simulations

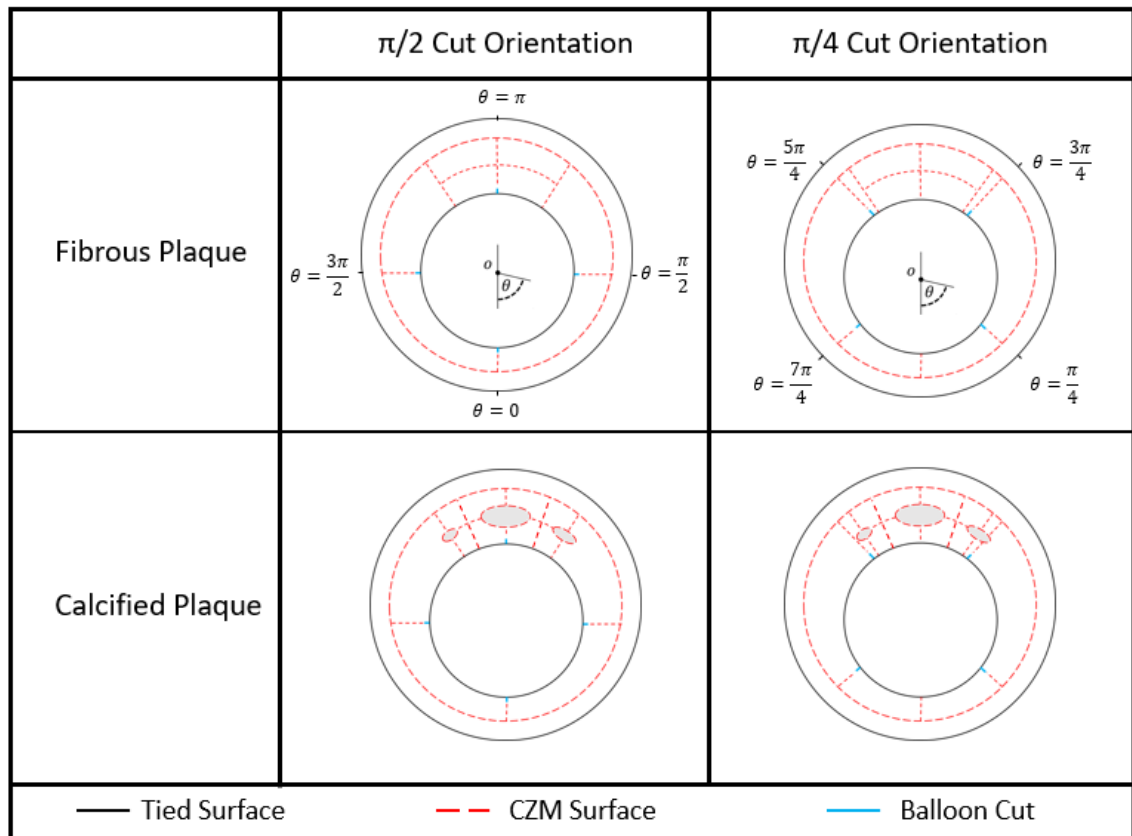


Figure 6.5. Schematic diagrams of various tied and cohesive surfaces combinations in fibrous and calcified plaque models. Four cuts were placed in intervals of  $\pi/2$  radians clockwise starting at  $\pi/2$  radians (left) and  $\pi/4$  radians (right) to the  $\theta = 0$ .

Cutting balloons are a type of angioplasty device designed to open difficult stenosis by introducing cuts in the lumen wall. The intended function to control the plaque rupture and reduce the pressure to inflate the plaque by purposefully cutting the plaque during expansion. Cutting balloon angioplasty is simulated by inserting four small equal-spaced “cuts” of depth of 0.127 mm. This “cut” depth is based on the blade dimensions for commercially available cutting-balloons (Bergersen et al., 2011). CZM surfaces continue from the cuts to the plaque-artery boundary. As illustrated in Figure 6.5, both calcified and uncalcified plaques are simulated, and cutting balloons oriented at both  $\pi/2$  radians and  $\pi/4$  radians are considered.

## 6.3 Results

### 6.3.1 Rupture experiments and inverse finite element modelling

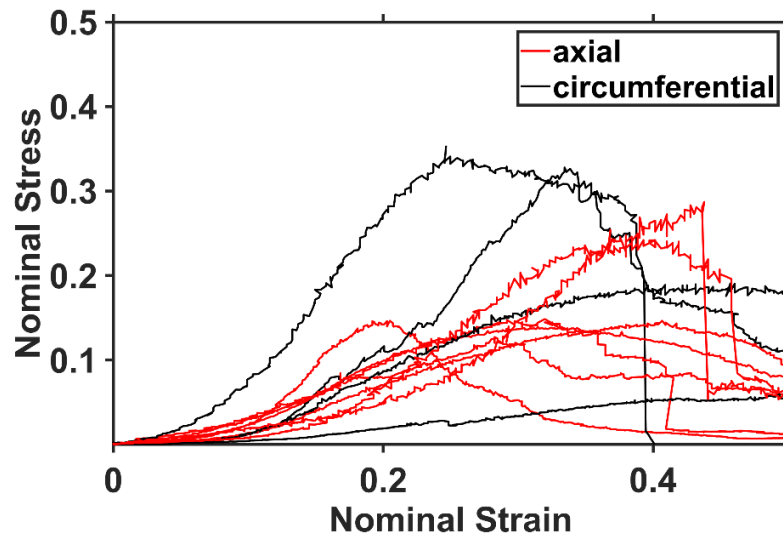


Figure 6.6. Nominal stress-strain results of uniaxial testing of composite plaque samples tested in the axial and circumferential directions (n=11).

Figure 6.6 shows the nominal stress-strain results from testing of 11 composite plaque samples. In 10 out of the 11 samples tested slipped or ruptured at the clamps during stretching. The sample that delaminated along the plaque-calcification interface is shown in Figure 6.7 (left).

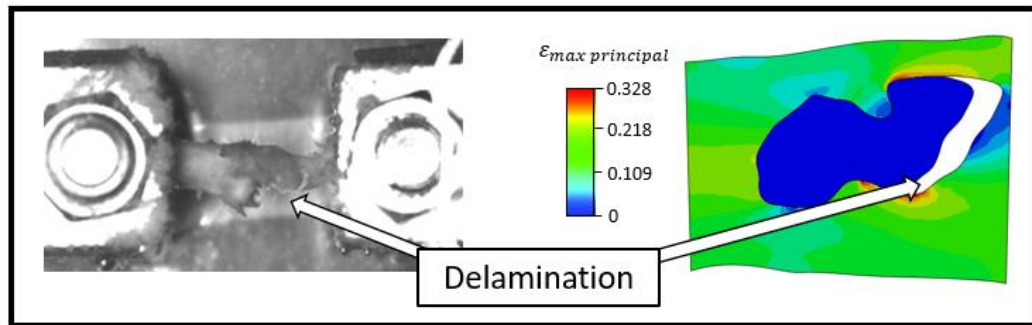


Figure 6.7. Experiment (left) showing delamination of the fibrous tissue away from the surface of the calcification and the computational model (right) simulating the experimental test using a cohesive surface at the calcification-fibrous interface.

The experimental test and computational simulation of a composite plaque rupture is shown in Figure 6.7. Extensive delamination along the calcification-fibrous interface was observed during experimental testing (Figure 6.7, left). A rupture force of 2.56 N was measured. The computational model (Figure 6.7, right) correctly predicts extensive delamination between the calcified particle and the fibrous tissue. A cohesive strength of 4 MPa is computed at the calcification-fibrous interface, resulting in a predicted rupture force of 2.54 N. This demonstrates a strong agreement between experimental and computational results.

6.3.2 2D angioplasty damage models

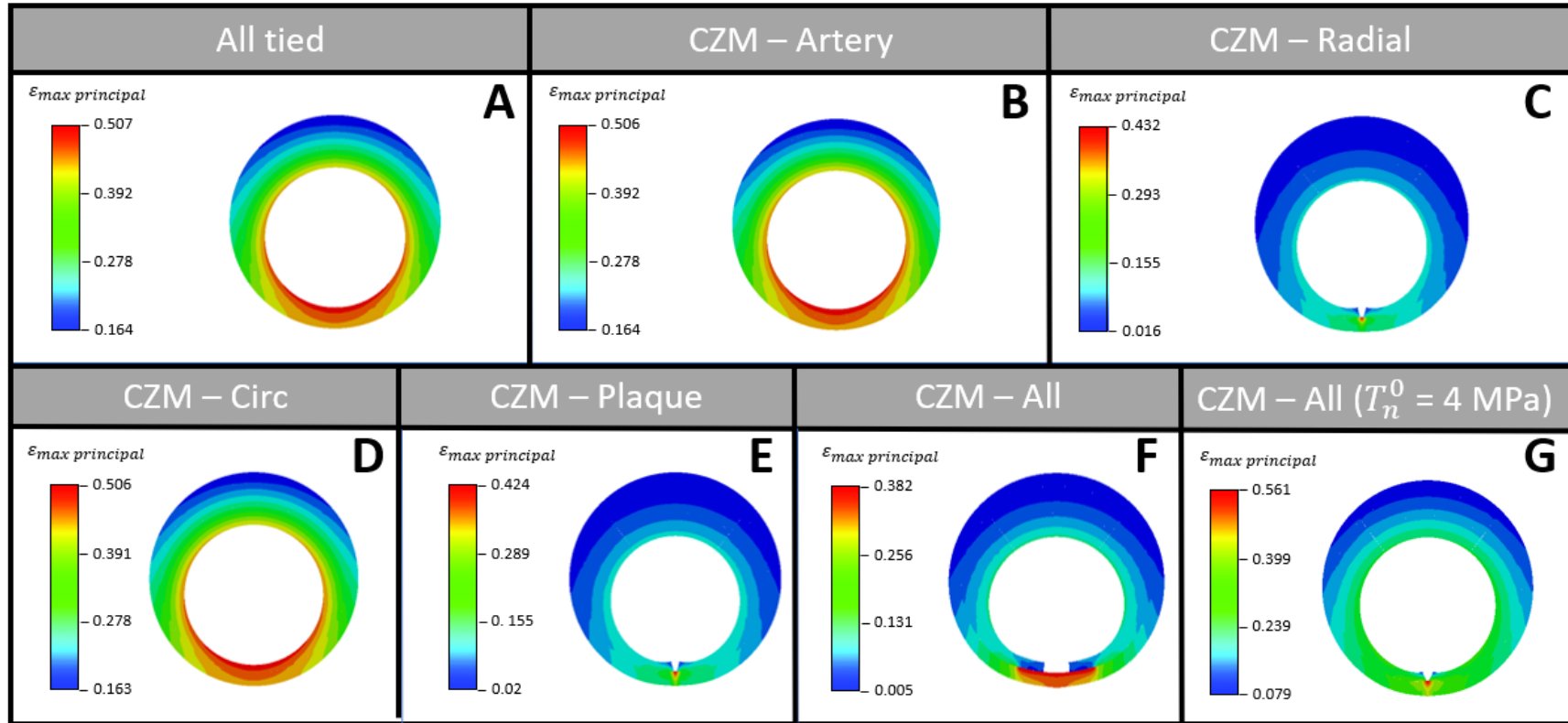


Figure 6.8. Maximum principal strain distribution during angioplasty in fibrous plaque models with cohesive boundaries in varying combinations and one additional model with all boundaries prescribed an interface strength of 4 MPa.

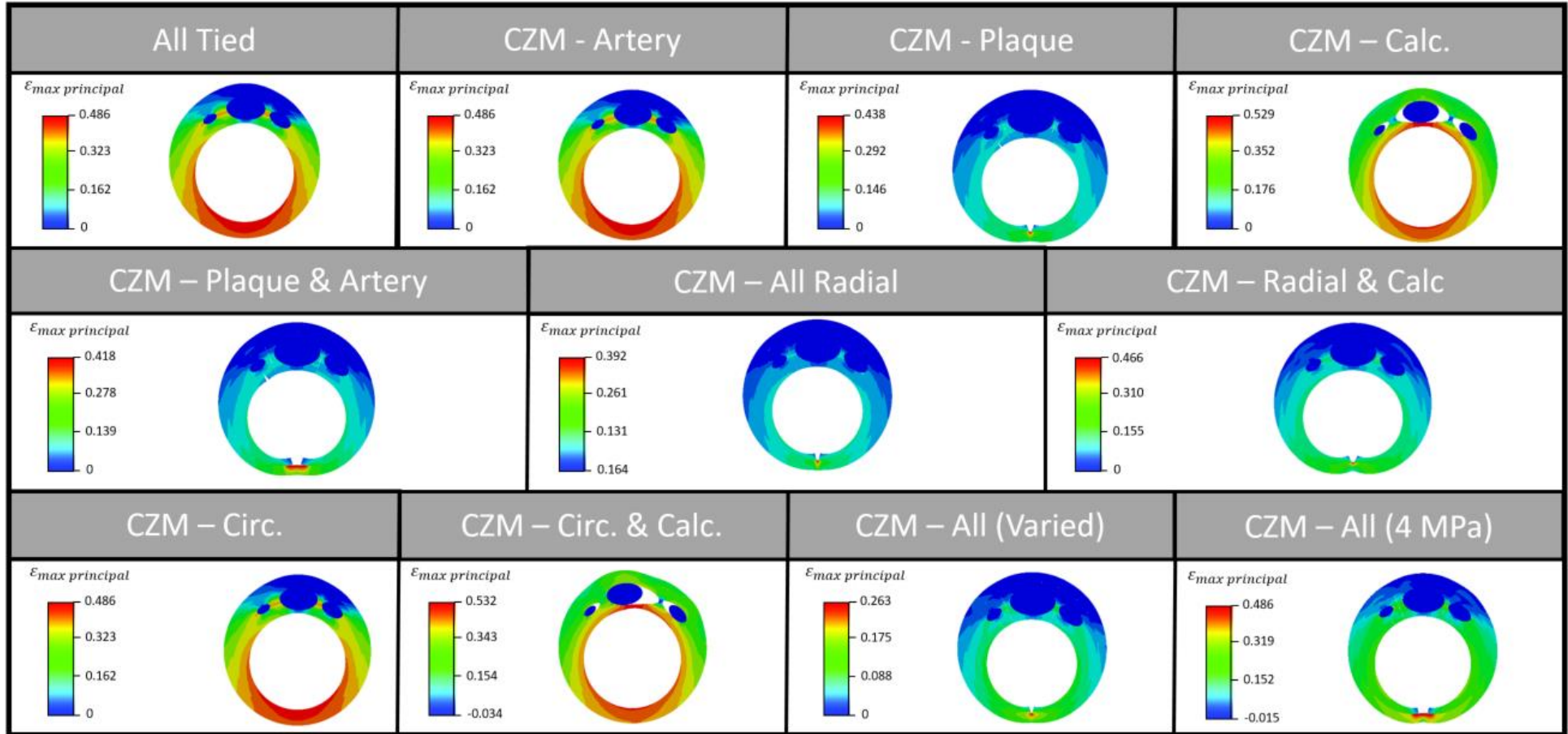


Figure 6.9. Maximum principal strain distribution during angioplasty in calcified plaque models with cohesive boundaries in varying combinations and one additional model with all boundaries prescribed an interface strength of 4 MPa.

Table 6.1. Rupture pressure of the varying cohesive boundaries in balloon angioplasty in fibrous and calcified plaques

CZM:	Rupture Pressure (MPa)	
	Fibrous	Calcified
All tied	Did not rupture	Did not rupture
Artery	Did not rupture	Did not rupture
Plaque	0.04115	0.0404
Calc	N/A	Did not rupture at lumen
Plaque & Artery	Same as All (varied)	0.0405
All Radial	0.04125	0.0404
Radial & Calc	N/A	0.0412
All Circ	Did not rupture	Did not rupture
Circ. & Calc.	N/A	Did not rupture at lumen
All	0.0413	0.0408
All ( $T_n^0 = 4$ MPa)	0.43695	0.3945

The strain distributions in the artery and plaque for the *All-tied* configurations (Figure 6.8(A) and Figure 6.9(A)) are similar to those in the *CZM-artery* (Figure 6.8(B) and Figure 6.9(B)) and *CZM-Circ* configurations (Figure 6.8(D) and Figure 6.9(H)). In cases where intra-fibrous tissue fracture is simulated (as shown in Figure 6.8(C, E, F and G) and Figure 6.9(C, E, F, G, J and K)), fracture is predicted to occur at  $\theta = 0$  at the thinnest section of the plaque. As shown in Table 6.1 fibrous models with radial boundary conditions fracture at approximately 0.0412 MPa and calcified models with radial boundary conditions fracture at approximately a pressure of 0.0407 MPa, excluding the  $T_n^0 = 4$  MPa models. All CZM-circumferential simulations (Figure 6.8 (B and D) and Figure 6.9((B, D, H and I)), in which radial crack propagation is not permitted, predict that the maximum lumen pressure is reached without any computed fracture at the fibrous-artery or intra-fibrous interfaces, with high strain values being computed in the

fibrous tissue in the thinnest region of the plaque ( $\theta=0$  radians). All CZM-circumferential configurations in the fibrous model Figure 6.8(B and D) are observed to have identical strain distribution and both achieve a lumen diameter of 8.04 mm at 1.5 MPa. All CZM-circumferential configurations without calcification-fibrous CZM surfaces in the calcified model, Figure 6.8(B and H) are observed to have identical strain distribution and both achieve a lumen diameter of 7.98 mm at 1.5 MPa. When the CZM model at the calcification-fibrous tissue interface is included but all other modes of fracture are prevented (CZM-calcification, Figure 6.9(D & I)) extensive delamination of the fibrous tissue from the stiff calcifications is predicted with an achieved lumen diameter of 8.08mm at 1.5 MPa Pressure. Addition of circumferentially oriented CZM surfaces does not significantly alter this failure mode, as shown in Figure 6.9(I). However, the introduction of radially oriented intra-fibrous tissue CZM surfaces significantly alters the failure mode, as shown in Figure 6.9(G). Intra-fibrous tissue fracture is predicted to occur in the radial direction at  $\theta=0, 2.44, 3.61$  and  $3.84$  radians, and the consequent reduction in strain energy in the fibrous tissue in the region of the calcifications eliminates delamination at the calcification-fibrous tissue interfaces. It is perhaps expected that radial intra-fibrous tissue fracture is predicted to occur instead of calcification-fibrous tissue delamination, given that the interface strengths of these failure modes differ by an order of magnitude (0.3MPa and 4MPa, respectively). However, even if the interface strength of the intra-fibrous tissue radial CZM surfaces is increased from 0.3 MPa to 4 MPa, as shown in Figure 6.9(K), fracture in the fibrous tissue is still predicted to occur at  $\theta =0$  radians, again with the consequent reduction in strain energy eliminating calcification-fibrous tissue delamination.

In summary, intra-fibrous tissue crack propagation in the radial direction is predicted to be the primary mode of failure of a plaque. The consequent reduction in strain energy in the fibrous tissue eliminates the prediction of delamination at the interface between the



fibrous tissue and calcified particles. Additionally, simulations reveal that delamination between the plaque and the vessel wall does not alter the strain state in the plaque.

### 6.3.3 Cutting Balloons

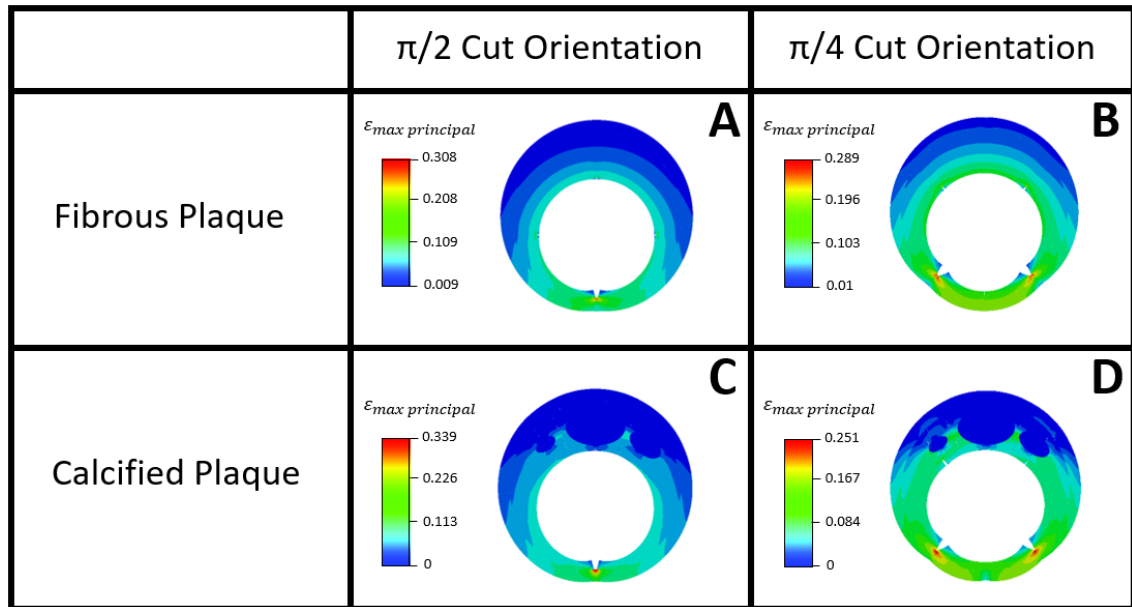


Figure 6.10. Maximum principal strain distribution during cutting balloon angioplasty (at both  $\pi/2$  and  $\pi/4$  cut orientations) in fibrous and calcified plaque models with cohesive interface strengths that vary by boundary and homogeneous interface strengths of 4 MPa each.

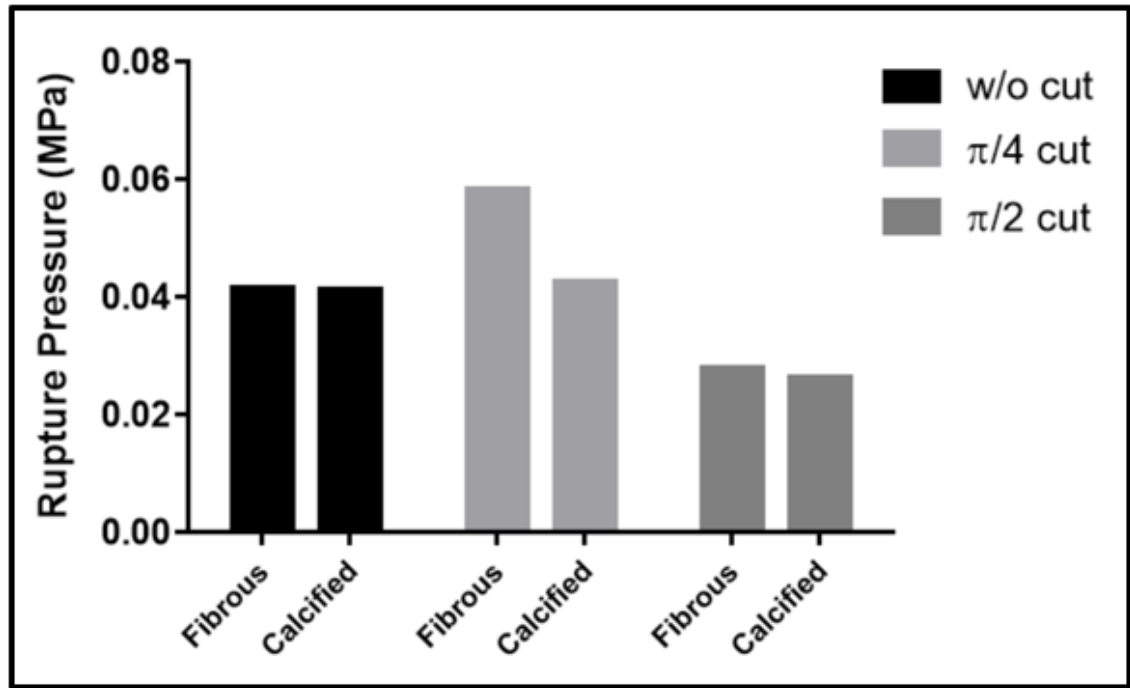


Figure 6.11. Comparison of the simulated rupture pressure for fibrous and calcified plaques with a balloon without a cut and balloons with cuts at  $\pi/2$  and  $\pi/4$  cut orientations.

Computed strain distributions and crack propagations induced by cutting-balloon angioplasty are shown in Figure 6.10. Corresponding computed balloon/lumen pressures for plaque rupture are shown in Figure 6.11. As shown in Figure 6.10(A), when a cutting balloon blade is positioned at  $\theta=0$  radians (the thinnest section of the vessel), a crack is predicted to propagate in the radial direction from the lumen to the vessel wall. It should be noted that significant crack propagation is not predicted at the location of the other three “cuts”. The early initiation of fracture at  $\theta=0$  radians reduces the strain energy in the fibrous tissue and prevents crack propagation at the other “cut” locations. As shown in Figure 6.11, for the  $\pi/2$  balloon configuration, positioning of a cutting blade at  $\theta=0$  radians, results in a reduction of the pressure required for rupture (32.4% reduction for a fibrous plaque and 36.3% reduction for a calcified plaque) in comparison to corresponding simulations without balloon “cuts”. This is due to the fact that rupture

initiates at  $\theta=0$  in the absence of “cuts”, and the introduction a “cut” at this location simply leads to accelerated crack propagation through the fibrous tissue.

As shown in Figure 6.10(B), if cutting balloon blades are not placed at the thinnest section of the plaque the predicted trend of rupture is altered. Crack propagation no longer occurs at  $\theta=0$  radians, but instead occur at the location of the balloon “cuts” at  $\theta = \pm\pi/4$  radians. If the “cut” is not positioned at the location where rupture would otherwise occur (i.e. at  $\theta=0$ ) the pressure required for rupture may in fact be increased, as shown in Figure 6.10. For example, the introduction of cuts at  $\theta = \pm\pi/4$  radians reduces the strain energy at  $\theta=0$ , and, in the case of a calcified plaque, a pressure of 0.0581 MPa is required to cause rupture at the “cut” locations. In comparison a pressure of only 0.0413 MPa is required in the absence of balloon “cuts”. The balloon/lumen pressure at rupture is predicted to be higher than that for the “ $\pi/2$ ” balloon configuration and without the “cuts”, 40.7% increase in the fibrous model and a 3.9% increase in the calcified model in comparison to without the inclusion of “cuts”. Overall, these simulations suggest that cutting balloons will result in fibrous tissue fracture in one or two locations in the thinner section of the plaque. Fracture is not predicted to occur at balloon “cuts” located in thicker section of the plaque, or in the calcified regions. Additionally, the introduction of balloon “cuts” is not predicted to dramatically reduce the balloon/lumen pressure at rupture.

## 6.4 Discussion

Balloon angioplasty is used as a method to increase patency in atherosclerotic plaques. Balloon deployment results in large stretching of the plaque and vessel in the circumferential direction. In the current study a cohesive zone formulation is used to simulate fracture of the fibrous tissue and delamination at the fibrous tissue-calcification interface and at the fibrous tissue-artery interface. These simulations reveal that the likely mechanism of rupture is intra-fibrous tissue crack propagation in the radial direction

located at the thinnest section plaque. The consequent release of strain energy from the plaque following such rupture eliminates the occurrence of delamination of calcified particles from the fibrous tissue or delamination of the plaque from the artery wall. Simulations also reveal that cutting balloon angioplasty reduces the pressure required for rupture one if the blades is positioned at the thinnest section of the plaque. Otherwise, it is predicted that the possible the introduction of cuts into the fibrous tissues can increase the pressure required to cause rupture.

This study presents experimental testing of a heterogeneous atherosclerotic plaque sample and the calibration of the cohesive strength for the calcification-fibrous interface. As shown from the results, implementation of a cohesive-based damage model can predict the force response observed experimentally. The calibrated strength of the calcification-fibrous interface is higher than previously reported failure stresses from literature (Cheng et al., 1993; Cunnane et al., 2016; Lendon et al., 1991; Leng et al., 2015b; Teng et al., 2009). Only 1 sample was observed to fracture at this interface, the other samples did not rupture at the calcification surface, instead rupturing at the grips or slipping. This alone suggests the interface strength is very high in comparison to the strength of the fibrous tissue. Difficulty to achieve such a fracture would explain why it has not been previously reported. Only reporting 1 sample to approximate the calcification-fibrous interface strength is a limitation of this study. With more samples that could be tested at this interface it could lead to a more accurate representation the value of the mean interface strength of this interface. The preliminary high strength calibrated in this study is hypothesized to be resultant from fibres in the fibrous tissue interlocking with the calcifications at the interface as previously seen in the scanning electron microscopy results reported in Chapter 4. A future study may be required to use histology on a large number of samples investigate the prevalence of interlocking fibres with the calcifications in composite plaque samples.

In summary, intra-fibrous tissue crack propagation in the radial direction is predicted to be the primary mode of failure of a plaque. The consequent reduction in strain energy in the fibrous tissue eliminates the risk of delamination at the interface between the fibrous tissue and calcified particles. Additionally, simulations reveal that delamination between the plaque and the vessel wall does not alter the strain state in the plaque. All plaque model configurations that are investigated in this study with only circumferential CZM surfaces have the same strain distribution in comparison to the tied configurations. In models without radial cohesive surfaces, there is no fracture occurring to release strain energy. The highest strain in the fully tied models is located at the thinnest section of the plaque material section, as observed in Chapter 5. This serves as an explanation as to why models with radial cohesive interfaces fracture at the  $\theta = 0$  radian interface in all models with a CZM surface at this location. In rupture simulations by Pei et al. (2013), it was found that when a stiff inclusion was introduced a crack would grow in the thinnest portion of the plaque away from the stiff inclusion. Fibrous and calcified plaque models had very little difference in the pressure required to initiate delamination. The strain concentrations caused by the presence of calcifications at the thinnest part of the plaque that were computed in Chapter 5, contribute very little to a difference in the pressure to cause delamination. This is likely due to how low interface strength is at the radial boundary is at the thinnest part of the plaque in comparison to the corresponding stress increase.

Simulations reveal that cutting balloon angioplasty reduces the pressure required for rupture one of the blades is positioned at the thinnest section of the plaque. On the other hand, if a blade is not positioned at the thinnest section of the fibrous tissues the pressure required to cause rupture is predicted to increase. A clinical study by Tang et al. (2014) does not find a statistically significant reduction in the dilatation pressure for cutting

balloon angioplasty in comparison to standard balloon angioplasty. A clinical study by Byrne et al (2017) also fails to establish the superiority of cutting balloons compared to standard angioplasty balloons. The cutting balloon computational models presented show that the effectiveness of cutting balloon angioplasty is highly sensitive to the precise positioning of a cutting blade at the thinnest section of the plaque providing insight into the results of these clinical studies.

The cohesive models in this study fracture at low pressures in comparison to the clinically used high pressure balloons. This suggests the cohesive properties are lower than physiological strengths. The intra-fibrous rupture strength of 300 kPa chosen in this study is based on conservative estimates made in previous literature for plaque rupture strength originating from Lendon et al. (1991). Many other studies have used this as a benchmark (Ferrara and Pandolfi, 2008; Maldonado et al., 2012; Vengrenyuk et al., 2012) which originates from Cheng et al., (1993). However, this study generated this value from analysis of heterogeneous plaques rather than homogeneous fibrous material. This would likely contribute to an underestimate of the rupture strength of the fibrous material as calcified particles would increase local stress states in the material. Additionally, this study implements a fibrous plaque-artery interface strength 0.14 MPa based on murine experimental data due to a lack of human data. In clinical cases, floating plaques can occur due to fibrous tissue-artery interface delamination. The measurement of the strength of this interface in diseased arteries could potentially lead to the prediction of similar types of plaque delamination using this modelling framework.

In order to predict failure in more complex plaque geometries it may be necessary to introduce a framework to predict kinking of crack paths. An extended finite element method (XFEM), similar to that implemented by Gasser and Holzapfel, (2007) and Versluis et al. (2006), offers such capability. However, XFEM simulations are computationally demanding and are highly mesh sensitive. Additional damage laws may

be required to representatively model plaque in high strain situations such as angioplasty. An example of this is permanent deformation in plaque tissue has been observed in a previous study by Maher et al. (2011).

In summary, preliminary simulations reveal that mechanism of rupture is intra-fibrous tissue crack propagation in the radial direction through the thinnest section of the plaque. The consequent release of strain energy from the plaque following such rupture eliminates the occurrence of delamination of calcified particles from the fibrous tissue or delamination of the plaque from the artery wall. Furthermore, the ability of cutting balloons to reduce the pressure at rupture is highly dependent on the precise positioning of a cutting blade at the thinnest section of the plaque..

## 6.5 References

- Akkus, N.I., Budeepalli, J., Cilingiroglu, M., 2013. Immediate stent recoil in an anastomotic vein graft lesion treated by cutting balloon angioplasty. *Rev. Port. Cardiol.* 32, 935–939. <https://doi.org/10.1016/j.repc.2013.04.013>
- Benzeggagh, M.L., Kenane, M., 1996. MEASUREMENT OF MIXED-MODE DELAMINATION FRACTURE TOUGHNESS OF UNIDIRECTIONAL GLASS/EPOXY COMPOSITES WITH MIXED-MODE BENDING APPARATUS. *Compos. Sci. Technol.* 56, 439–449.
- Bergersen, L., Gauvreau, K., Justino, H., Nugent, A., Rome, J., Kreutzer, J., Rhodes, J., Nykanen, D., Zahn, E., Latson, L., Moore, P., Lock, J., Jenkins, K., 2011. Randomized trial of cutting balloon compared with high-pressure angioplasty for the treatment of resistant pulmonary artery stenosis. *Circulation* 124, 2388–2396. <https://doi.org/10.1161/CIRCULATIONAHA.111.018200>
- Bluestein, D., Alemu, Y., Avrahami, I., Gharib, M., Dumont, K., Ricotta, J.J., Einav, S., 2008. Influence of microcalcifications on vulnerable plaque mechanics using FSI modeling. *J. Biomech.* 41, 1111–1118. <https://doi.org/10.1016/j.jbiomech.2007.11.029>
- Byrne, R.A., Stone, G.W., Ormiston, J., Kastrati, A., 2017. Coronary balloon angioplasty, stents, and scaffolds. *Lancet* 390, 781–792. [https://doi.org/10.1016/S0140-6736\(17\)31927-X](https://doi.org/10.1016/S0140-6736(17)31927-X)
- Cheng, G.G., Loree, H.M., Kamm, R.D., Fishbein, M.C., Lee, R.T., 1993. Distribution of Circumferential Stress in Ruptured and Stable Atherosclerotic Lesions. *Circulation* 87, 1179–1187.
- Cunnane, E.M., Barrett, H.E., Kavanagh, E.G., Mongrain, R., Walsh, M.T., 2016. The influence of composition and location on the toughness of human atherosclerotic femoral plaque tissue. *Acta Biomater.* 31, 264–275. <https://doi.org/10.1016/j.actbio.2015.11.056>
- Cunnane, E.M., Mulvihill, J.J.E., Barrett, H.E., Healy, D.A., Kavanagh, E.G., Walsh, S.R., Walsh, M.T., 2015. Mechanical, biological and structural characterization of human atherosclerotic femoral plaque tissue. *Acta Biomater.* 11, 295–303. <https://doi.org/10.1016/j.actbio.2014.09.024>
- Ferrara, A., Pandolfi, A., 2008. Numerical modelling of fracture in human arteries. *Comput. Methods Biomech. Biomed. Engin.* 11, 553–567. <https://doi.org/10.1080/10255840701771743>
- Gasser, T.C., Holzapfel, G.A., 2007. Modeling plaque fissuring and dissection during balloon angioplasty intervention. *Ann. Biomed. Eng.* 35, 711–23. <https://doi.org/10.1007/s10439-007-9258-1>
- Hutcheson, J.D., Maldonado, N., Aikawa, E., 2014. Small entities with large impact. *Curr. Opin. Lipidol.* 25, 327–332. <https://doi.org/10.1097/mol.0000000000000105>
- Kasirajan, K., Schneider, P.A., Hood, D., Dalman, R., Coogan, S., Andros, G., Ahn, S., 2004. Early outcome of “cutting” balloon angioplasty for infrainguinal vein graft stenosis. *J. Vasc. Surg.* 39, 702–708. <https://doi.org/10.1016/j.jvs.2003.10.046>



- Kelly-Arnold, A., Maldonado, N., Laudier, D., Aikawa, E., Cardoso, L., Weinbaum, S., 2013. Revised microcalcification hypothesis for fibrous cap rupture in human coronary arteries. *Proc. Natl. Acad. Sci.* 110, 10741–10746. <https://doi.org/10.1073/pnas.1308814110>
- Lawlor, M.G., O'Donnell, M.R., O'Connell, B.M., Walsh, M.T., 2011. Experimental determination of circumferential properties of fresh carotid artery plaques. *J. Biomech.* 44, 1709–1715. <https://doi.org/10.1016/j.jbiomech.2011.03.033>
- Lendon, C.L., Davies, M.J., Born, G.V.R., Richardson, P.D., 1991. Atherosclerotic plaque caps are locally weakened when macrophages density is increased. *Atherosclerosis* 87, 87–90. [https://doi.org/10.1016/0021-9150\(91\)90235-U](https://doi.org/10.1016/0021-9150(91)90235-U)
- Leng, X., Chen, X., Deng, X., Sutton, M.A., Lessner, S.M., 2015a. Simulation of Atherosclerotic Plaque Delamination Using the Cohesive Zone Model. *Conf. Proc. Soc. Exp. Mech. Ser.* 63, 81–88. [https://doi.org/10.1007/978-3-319-06974-6\\_12](https://doi.org/10.1007/978-3-319-06974-6_12)
- Leng, X., Chen, X., Deng, X., Sutton, M.A., Lessner, S.M., 2015b. Modeling of Experimental Atherosclerotic Plaque Delamination. *Ann. Biomed. Eng.* 43, 2838–2851. <https://doi.org/10.1007/s10439-015-1357-9>
- Leng, X., Davis, L.A., Deng, X., Sutton, M.A., Lessner, S.M., 2016. Numerical modeling of experimental human fibrous cap delamination. *J. Mech. Behav. Biomed. Mater.* 59, 322–336. <https://doi.org/10.1016/j.jmbbm.2016.02.011>
- Liu, W., Lu, S., Feng, Y., Zhang, Z., Liu, P., Liu, Z., 2017. Truth of floating carotid plaques. *Front. Neurol.* 8, 8–11. <https://doi.org/10.3389/fneur.2017.00673>
- Maher, E., Creane, A., Sultan, S., Hynes, N., Lally, C., Kelly, D.J., 2011. Inelasticity of Human Carotid Atherosclerotic Plaque. *Ann. Biomed. Eng.* 39, 2445–2455. <https://doi.org/10.1007/s10439-011-0331-4>
- Maldonado, N., Kelly-Arnold, A., Vengrenyuk, Y., Laudier, D., Fallon, J.T., Virmani, R., Cardoso, L., Weinbaum, S., 2012. A mechanistic analysis of the role of microcalcifications in atherosclerotic plaque stability: potential implications for plaque rupture. *Am. J. Physiol. Circ. Physiol.* 303, H619–H628. <https://doi.org/10.1152/ajpheart.00036.2012>
- Merei, B., Badel, P., Davis, L., Sutton, M.A., Avril, S., Lessner, S.M., 2017. Atherosclerotic plaque delamination: Experiments and 2D finite element model to simulate plaque peeling in two strains of transgenic mice. *J. Mech. Behav. Biomed. Mater.* 67, 19–30. <https://doi.org/10.1016/j.jmbbm.2016.12.001>
- Mulvihill, J.J., Cunnane, E.M., McHugh, S.M., Kavanagh, E.G., Walsh, S.R., Walsh, M.T., 2013. Mechanical, biological and structural characterization of in vitro ruptured human carotid plaque tissue. *Acta Biomater.* 9, 9027–9035. <https://doi.org/10.1016/j.actbio.2013.07.012>
- Pei, X., Wu, B., Li, Z.-Y., 2013. Fatigue Crack Propagation Analysis of Plaque Rupture. *J. Biomech. Eng.* 135, 101003. <https://doi.org/10.1115/1.4025106>

- Rambhia, S.H., Liang, X., Xenos, M., Alemu, Y., Maldonado, N., Kelly, A., Chakraborti, S., Weinbaum, S., Cardoso, L., Einav, S., Bluestein, D., 2012. Microcalcifications increase coronary vulnerable plaque rupture potential: A patient-based micro-ct fluid-structure interaction study. *Ann. Biomed. Eng.* 40, 1443–1454. <https://doi.org/10.1007/s10439-012-0511-x>
- Tang, Z., Bai, J., Su, S.P., Wang, Y., Liu, M.H., Bai, Q.C., Tian, J.W., Xue, Q., Gao, L., An, C.X., Liu, X.J., 2014. Cutting-balloon angioplasty before drug-eluting stent implantation for the treatment of severely calcified coronary lesions. *J. Geriatr. Cardiol.* 11, 44–49. <https://doi.org/10.3969/j.issn.1671-5411.2014.01.012>
- Teng, Z., Tang, D., Zheng, J., Woodard, P.K., Hoffman, A.H., 2009. An experimental study on the ultimate strength of the adventitia and media of human atherosclerotic carotid arteries in circumferential and axial directions. *J. Biomech.* 42, 2535–2539. <https://doi.org/10.1016/j.jbiomech.2009.07.009>
- Vengrenyuk, Y., Cardoso, L., Weinbaum, S., Laudier, D., Fallon, J.T., Maldonado, N., Virmani, R., Kelly-Arnold, A., 2012. A mechanistic analysis of the role of microcalcifications in atherosclerotic plaque stability: potential implications for plaque rupture. *Am. J. Physiol. Circ. Physiol.* 303, H619–H628. <https://doi.org/10.1152/ajpheart.00036.2012>
- Versluis, A., Bank, A.J., Douglas, W.H., 2006. Fatigue and plaque rupture in myocardial infarction. *J. Biomech.* 39, 339–347. <https://doi.org/10.1016/j.jbiomech.2004.10.041>
- Wang, R., Raykin, J., Li, H., Gleason, R.L., Luke, J., 2014. Differential mechanical response and microstructural organization between non-human primate femoral and carotid arteries 1041–1051. <https://doi.org/10.1007/s10237-014-0553-0>
- Wang, Y., Ning, J., Johnson, J.A., Sutton, M.A., Lessner, S.M., 2011. Development of a quantitative mechanical test of atherosclerotic plaque stability. *J. Biomech.* 44, 2439–2445. <https://doi.org/10.1016/j.jbiomech.2011.06.026>
- Wenk, J.F., Papadopoulos, P., Zohdi, T.I., 2010. Numerical Modeling of Stress in Stenotic Arteries With Microcalcifications: A Micromechanical Approximation. *J. Biomech. Eng.* 132, 091011. <https://doi.org/10.1115/1.4001351>

# 7 CONCLUDING REMARKS AND FUTURE RECOMMENDATIONS

## 7.1 Summary of Key Findings

The experimental and computational investigations of atherosclerotic plaque outlined in this thesis provide new insights into the mechanical behaviour of plaque and medical device deployment in stenosed arteries. This section outlines the key contributions of this research.

### 7.1.1 Chapter 4

- $\mu$ CT scanning of plaques provides new detail on the morphology and distribution of calcifications. Iliofemoral samples are found to have a higher calcified volume than carotid samples. In all cases the largest calcified particle is found to comprise of over 50% the total calcified volume.  $\mu$ CT scans also reveal that large calcified particles frequently exhibit longitudinal alignment to the centreline of the lumen.
- Hyperelastic and viscoelastic material behaviour in both iliofemoral and carotid fibrous material is characterised from mechanical testing of isolated fibrous tissue. Testing also uncovers that iliofemoral samples are significantly stiffer than carotid samples.
- The first macro-scale investigation of calcification material behaviour is performed through unconfined compression testing of isolated calcifications in conjunction with inverse finite element analysis. This investigation reveals that calcified particles exhibit hyper-viscoelastic material behaviour.

### 7.1.2 Chapter 5

- Higher volumes of calcifications result in higher radial balloon forces to restore full lumen patency during angioplasty.
- Plaques containing circumferentially aligned calcifications require higher balloon pressure than plaques with longitudinally aligned calcifications.
- High strains are predicted in the region of fibrous tissue that is in series (in the circumferential direction) with calcifications, with peak strains being computed in the thinnest section of eccentric plaques.

### 7.1.3 Chapter 6

- A preliminary value for the strength of the calcification-matrix interface is determined using inverse finite element modelling of experimental rupture testing of composite calcified excised plaque samples.
- Finite element modelling of balloon angioplasty predicts that the mechanism of rupture in intra-fibrous tissue is crack propagation in the radial direction through the thinnest section of the plaque.
- The ability of a cutting balloon to reduce the pressure required for plaque rupture is highly dependent on the precise positioning of cutting blades in relation to the thinnest section of the plaque.

## 7.2 Future Recommendations

- As discussed in Chapter 4, in order to accurately model atherosclerotic plaques, full characterisation of each of the plaque components is required. Future experimental studies should independently characterise plaque constituents using a similar methodology to that of Chapter 4.
- The results reported in this thesis suggest site specificity in the fibrous material behaviour of plaques. The majority of plaque testing reported in the literature has

been carried out on plaque originating from iliac, femoral and carotids, primarily due to ease of acquisition. However, testing of coronary samples is distinctly lacking, even though the most common target vessels in stenting are the coronary arteries.

- As observed in literature and as per the results presented in Chapter 4, there is significant variability in mechanical behaviour of plaque samples. It is recommended that larger scale studies, with a standardised testing protocol, are performed in order to achieve sufficient statistical power.
- In order to improve understanding of plaque damage and rupture more experimental testing of human samples is required, building on the work by Maher et al. (2011), in terms of permanent deformation and softening, and Leng et al. (2015), in terms of the artery-plaque interface in murine models. This would provide a significant improvement for the understanding of plaque material behaviour under large deformation.
- As described in Chapter 6 there is currently no established rupture stress for homogeneous plaque fibrous tissue. This is also the case for calcifications, where the yield stress and ultimate tensile strength is essential to the computational modelling of scoring balloon deployment in calcified plaques.
- Large variation in the stress states and lumen gain have been observed in plaques with varying constituent geometries. Computational modelling of balloon angioplasty and stent deployment in atherosclerotic arteries is not currently required for regulatory approval. Similar to the computational test-bed suggested by Conway et al. (2012), the author expands this suggestion to include a standardised “testing gauntlet” to assess stent performance, potentially containing semi-idealised plaques varying in calcification content, lipid content, stenosis

size, eccentricity, calcification geometry and lipid geometry. “Worst-case” plaque compositions could also be included as a device testing standard.

- Finite element is used a predictive tool in this thesis, but models should be experimentally validated where possible to determine accuracy. Model validation was considered for the simulations presented in Chapters 5 and 6, however due to a lack of plaque and calcification analogues available and a scarcity of human plaque samples, experimental validation was determined to be unfeasible. If possible, future work should be undertaken to validate the models presented in this thesis.
- The creation of an open source anonymised repository of MRI or CT scans of atherosclerotic plaques would allow for the creation of patient specific finite element models, leading to more accurate modelling of stress states during vascular medical device deployment. A large collection of 3D imaging data would provide additional statistical metrics on the variation in plaque composition and geometrical properties. This would benefit both academia and the medical device industry by enabling physically representative computational models.
- Similar to the work presented by García et al. (2012) and Kioussis et al. (2007), stent designs should be computationally evaluated in varying plaque compositions and geometries. This data could be used to inform clinicians and device designers about the best computationally performing stents for a given plaque configuration.
- Fluid structure interaction modelling should be implemented in stenting models to determine wall shear stress, that has been shown to influence restenosis (Boland, Grogan and McHugh, 2019).
- Finally, new techniques are emerging for solving complex computational problems, such as machine learning, which could be implemented in medical device design. For example, a repository of site specific plaque geometries may

be utilised for optimised and automated stent design, potentially improving device performance and clinical outcomes.

### 7.3 References

- Boland, E. L., Grogan, J. A. and McHugh, P. E. (2019) ‘Computational modelling of magnesium stent mechanical performance in a remodelling artery: Effects of multiple remodelling stimuli’, *International Journal for Numerical Methods in Biomedical Engineering*, 35(10), pp. 1–25. doi: 10.1002/cnm.3247.
- Conway, C. et al. (2012) ‘A Computational Test-Bed to Assess Coronary Stent Implantation Mechanics Using a Population-Specific Approach’, *Cardiovascular Engineering and Technology*, 3(4), pp. 374–387. doi: 10.1007/s13239-012-0104-8.
- García, A., Peña, E. and Martínez, M. A. (2012) ‘Influence of geometrical parameters on radial force during self-expanding stent deployment. Application for a variable radial stiffness stent’, *Journal of the Mechanical Behavior of Biomedical Materials*. Elsevier Ltd, 10, pp. 166–175. doi: 10.1016/j.jmbbm.2012.02.006.
- Kiousis, D. E., Gasser, T. C. and Holzapfel, G. A. (2007) ‘A Numerical Model to Study the Interaction of Vascular Stents with Human Atherosclerotic Lesions’, *Annals of Biomedical Engineering*. Springer Science and Business Media {LLC}, 35(11), pp. 1857–1869. doi: 10.1007/s10439-007-9357-z.
- Leng, X. et al. (2015) ‘Simulation of Atherosclerotic Plaque Delamination Using the Cohesive Zone Model’, *Conference Proceedings of the Society for Experimental Mechanics Series*, 63(VOLUME 2), pp. 81–88. doi: 10.1007/978-3-319-06974-6\_12.
- Maher, E. et al. (2011) ‘Inelasticity of Human Carotid Atherosclerotic Plaque’, *Annals of Biomedical Engineering*, 39(9), pp. 2445–2455. doi: 10.1007/s10439-011-0331-4.



